



## Experimental and numerical investigations of plasma turbulence

Forskningscenter Risø, Roskilde

*Publication date:*  
1990

*Document Version*  
Publisher's PDF, also known as Version of record

[Link back to DTU Orbit](#)

*Citation (APA):*  
Huld, T. (1990). Experimental and numerical investigations of plasma turbulence. (Risø-M; No. 2858).

## DTU Library

Technical Information Center of Denmark

---

### General rights

Copyright and moral rights for the publications made accessible in the public portal are retained by the authors and/or other copyright owners and it is a condition of accessing publications that users recognise and abide by the legal requirements associated with these rights.

- Users may download and print one copy of any publication from the public portal for the purpose of private study or research.
- You may not further distribute the material or use it for any profit-making activity or commercial gain
- You may freely distribute the URL identifying the publication in the public portal

If you believe that this document breaches copyright please contact us providing details, and we will remove access to the work immediately and investigate your claim.

**DT 9000116**

**RISØ**

**Risø-M-2858**

**Experimental and Numerical  
Investigations of  
Plasma Turbulence**

**Thomas Huld**

**Risø National Laboratory, DK-4000 Roskilde, Denmark  
July 1990**

# **Experimental and Numerical Investigations of Plasma Turbulence**

**Risø-M-2858**

**Thomas Huld**

*Risø National Laboratory, DK-4000 Roskilde, Denmark  
July 1990*

**Abstract** Turbulence in plasmas has been investigated experimentally and numerically. The work described here is divided into four parts:

- Experiments on edge turbulence in a single-ended Q-machine. Convective cells are investigated in detail together with the anomalous transport caused by them.
- Numerical simulation of the edge turbulence in the Q-machine. This simulation uses spectral methods to solve Euler's equation in a cylindrical geometry.
- Measurements on wave propagation and the ion beam instability in an unmagnetized plasma with an ion beam with a finite diameter.
- Development of software for the automated acquisition of data. This program can control an experiment as well as make measurements. It also includes a graphics part.

This report is practically identical to the thesis submitted to the Technical University of Denmark for obtaining the Ph.D. degree. This was submitted on 1 October 1989 and the lecture held on 1 March 1990.

ISBN 87-550-1624-3

ISSN 0418-6435

Grafisk Service Rissø 1990

**For Geske**

# Contents

<b>Acknowledgements</b>	v
<b>Summary</b>	vi
<b>Dansk resumé—Abstract in Danish</b>	viii
<b>1 Introduction</b>	1
<b>2 Experiments on edge turbulence in a Q-machine</b>	3
2.1 Introduction . . . . .	3
2.2 Experimental set-up . . . . .	3
2.3 Measurements of turbulence in the plasma edge. . . . .	4
2.4 Interaction between the turbulence and an injected convective cell	13
2.5 Anomalous plasma transport . . . . .	18
2.6 Conditional statistical analysis of the turbulence . . . . .	26
2.7 Plans for the near future . . . . .	30
<b>3 Numerical simulation of Q-machine edge plasma</b>	32
3.1 Formulation of the problem . . . . .	32
3.2 The Numerical Methods . . . . .	33
3.3 Numerical results. . . . .	45
3.4 Attempts at removing the ringing . . . . .	52
3.5 Future developments . . . . .	54
<b>4 Experiments on wave propagation and instability in a plasma with an ion beam</b>	55
4.1 Introduction . . . . .	55
4.2 Analysis of the plasma response to a dilute beam of fast ions. . . . .	55
4.3 Briefly on the ion beam instability. . . . .	64
4.4 Experiments on the DP-machine . . . . .	65
<b>5 The AIDA data acquisition and display system.</b>	78
5.1 Introduction . . . . .	78
5.2 General structure of AIDA . . . . .	78
5.3 Measurement Types . . . . .	79
5.4 The data acquisition subprograms . . . . .	80
5.5 The graphics subprograms . . . . .	83
5.6 Making and updating Measurement Types . . . . .	87
5.7 Present and future developments . . . . .	88
<b>A Some useful relations between Chebyshev series</b>	90
<b>B Consistency of the discrete Fourier expansion</b>	91
<b>C Nyquist analysis for the plasma dispersion function</b>	92
<b>D Briefly on the Cubic Spline Interpolation</b>	94
<b>References</b>	95

## **Acknowledgements**

**This report describes the work in which I have participated during the last two and a half years in the Group for Fundamental Plasma Physics. None of this would have been possible without the members of this group, indeed it is mainly their work I am describing here. They are on the experimental work: H. L. Pécsei, J. Juul Rasmussen and, on the Q-machine experiment, S. Iizuka of the Yokohama National University. On the numerical simulation work it is: F. R. Hansen, J-P. Lynov and E. A. Coustans, the latter from University of New Mexico. I would like to thank them all for the privilege (for such it is) of working in the group. I would also like to thank B. Reher, M. Nielsen, J. Thorsen and K-V. Weisberg for their technical assistance in the experimental work. Finally, I would like to thank our head of section, Dr. V. O. Jensen for his continuous help and encouragement.**

## Summary

Various aspects of plasma turbulence have been investigated experimentally and numerically. In magnetized plasmas the emphasis has been on the study of *flute-type* or *convective cell* fluctuations in the edge of a Q-machine plasma, caused by the Kelvin-Helmholtz instability. This has been studied extensively. The studies fall into four main groups:

1. General studies of the turbulence using correlation measurements. These have uncovered the spectra of the fluctuations under various conditions and the phase relations between the potential and density fluctuations both in the main plasma and in the edge region.
2. Investigations of the interaction between the turbulent (spontaneous) fluctuations and an externally injected convective cell. It is found that the turbulence interacts nonlinearly with the cell and that the cell essentially absorbs the energy of the turbulence. The result is a cascade of energy from high mode numbers to lower ones.
3. Measurements of the cross-field plasma transport associated with the turbulence have been performed. Here it is found that the turbulent transport is orders of magnitude larger than that of classical diffusion. In other words, this type of turbulence may be a major source of plasma loss in some types of magnetic confinement experiments. The results may be applicable even if the driving mechanism is different.
4. Conditional statistical measurements of the turbulence have been made using a digital oscilloscope to acquire real-time traces of the fluctuating quantities. These make it possible to get a picture of the state of the plasma during large fluctuations in the density or electrical field and to measure the anomalous flux associated with such large fluctuations.

A simulation of the Kelvin-Helmholtz instability in the edge of the Q-machine has been initiated. In this simulation the guiding center equations (the fluid continuity equation, the  $\mathbf{E} \times \mathbf{B}$  velocity equation, and Poisson's equation) are solved in two dimensions in cylindrical geometry (the direction along the magnetic field is ignored). A spectral method is employed. In the radial direction the expansion is made with Chebyshev polynomials, while in the azimuthal direction a Fourier expansion is employed as the boundary conditions are periodical. A very efficient solver has been developed for Poisson's equation in this geometry which yields a very accurate solution with only  $O(1)$  calculations per grid point. Initial results are in qualitative agreement with experiment though problems remain. An extension to include viscous effects is being developed at the time of writing (autumn 1989).

In an unmagnetized plasma investigations of the ion beam instability have been performed. The emphasis has been on the study of the plasma response to a weak beam of fast (supersonic) ions moving through the plasma. Experiments in a Double-Plasma device have been performed and are compared to theoretical calculations. Good agreement has been obtained. In addition, initial experiments have been made on the ion beam instability with a finite-diameter ion beam.

Finally, a versatile program for data acquisition and display is presented. This program, called AIDA, has originally been developed for the experiments of the Plasma Physics Section. However, it is adaptable for many types of experiment. It can be used both for automatic data acquisition and also to some extent to



control the experiment. The emphasis has been on ease of use, and menus are used extensively. Most of the data presented in this thesis have been acquired using this program which runs on a standard PC.

## Dansk resumé

Forskellige aspekter af turbulens i plasmæer er blevet udforsket, både eksperimentelt og ved numeriske simulationer. I magnetiserede plasmæer har hovedvægten været lagt på studiet af fluktuationer af *flute*-typen, også kaldet *konvektive celler* i kanten af et plasma i en Q-maskine. Disse fluktuationer bliver drevet af Kelvin-Helmholts instabiliteten. Undersøgelserne kan inddrages i fire hovedgrupper:

1. Generelle studier af turbulensen ved hjælp af korrelationsmålinger. På denne måde er fluktuationernes spektrum blevet målt sammen med faserelationerne mellem fluktuationerne i potentialet og plasmætætheden, både i midten af plasmæet og i kanten, hvor turbulensen er mest udtalt.
2. Undersøgelser af vekselvirkningen mellem de (spontane) turbulente fluktuationer og en konvektiv celle påtvunget plasmæet. Det ses her, at turbulensen vekselvirker på en ikke-lineær måde med cellen, og at cellen opsuger energi fra turbulensen. Følgen er, at energien strømmer fra høje bølgelængder til lave bølgelængder.
3. Målinger af den plasmætransport på tværs af magnetfeltet, som turbulensen forårsager. Her finder man, at den turbulente transport er flere størrelsesordener større end den, der skyldes klassisk diffusion. Med andre ord: turbulensen kan være hovedkilden til tab af plasma i visse typer af eksperimenter med magnetisk indeslutning af plasmæet. Disse resultater kan være af betydning for andre eksperimenter, også selv om mekanismen, der forårsager turbulensen er en anden.
4. Målinger af turbulensen med betinget statistiske metoder er blevet udført v. hj. a. et digitaloscilloskop, der kan opsamle tidsrækker af de fluktuerende størrelser i sand tid. Dette muliggør en undersøgelse af plasmæets tilstand, når fluktuationerne i tætheden eller  $E$ -feltet er store, og at måle den dertil hørende radiære flux.

Et projekt til simulering af Kelvin-Helmholts instabiliteten i kanten af Q-maskinen er blevet indledt. I denne simulation findes en løsning til Guiding-center ligningerne (kontinuitetsligningen,  $E \times B$ -hastighedsligningen og Poissons ligning) i polære koordinater. Kun bevægelse på tværs af magnetfeltet bliver betragtet her. Løsningen findes ved brug af spektrale metoder. I den radiære retning udvikles i Chebyshevpolynomier mens en Fourierudvikling bruges i den azimuthale retning, eftersom randbetingelserne her er periodiske. En særdeles effektiv løsningsmetode til Poissons ligning er blevet udviklet. Løsningen kan her findes med  $O(1)$  beregninger pr. gitterpunkt. De første resultater viser en kvalitativ overensstemmelse med eksperimenterne. Der er dog stadig visse problemer. Disse søges løst ved at medtage viskositet i ligningerne. Dette er ved at blive udviklet i skrivende stund (efterår 1989).

I et umagnetiseret plasma er der blevet udført undersøgelser af ion-beam instabiliteten. Her er vægten blevet lagt på studiet af forstyrrelsen af plasmæet som følge af indskydning af en svag stråle af hurtige (supersoniske) ioner. Der er blevet udført eksperimenter i Dobbelt-plasma maskine 1, og disse er blevet sammenholdt med teoretiske beregninger. Der ses at være god overensstemmelse. Derudover er der blevet foretaget indledende eksperimenter over ion-beam instabiliteten med en ionstråle med endelig diameter.

I forbindelse med eksperimenterne er der blevet udviklet et alsidigt computerprogram til opsamling og grafisk udskrivning af måledata. Programmet, AIDA, er

oprindeligt blevet udviklet til eksperimenterne i Plasmafysiksektionen, men kan anvendes i mange typer af eksperimenter. Det kan bruges både til automatisk opsamling af data og til at styre eksperimentet. Der er blevet lagt stor vægt på at gøre det brugervenligt ved udstrakt brug af menuer. Størstedelen af de måledata, der præsenteres i denne rapport er opsamlet med AIDA, der kører på en standard PC.

# 1 Introduction

The study of turbulence in plasmas has received much interest in recent years. This is especially true for magnetic fusion energy research. The objective of magnetic fusion research is to confine a hot plasma in a magnetic field sufficiently well to allow fusion processes to occur. By now, many of the large-scale instabilities which impaired the performance of early experiments have been brought under control. However, the plasma confinement is still not nearly as good as would be expected from an analysis of classical diffusion. The reason for this is thought to lie mainly with what has been termed *microinstabilities* [1, ch. 11]. These appear where free energy is available, e.g. where the gradients in density, magnetic or electrical field or temperature are large, or where there are inhomogeneities in the velocity distribution. Instabilities in these regions may cause turbulence with scale sizes that are small compared to that of the experiment<sup>1</sup>. While these turbulent fluctuations do not completely disrupt the plasma discharge they are nonetheless thought to contribute strongly to the anomalous transport of plasma across the magnetic field. An understanding of this would be most desirable since it may point to remedies or to specific conditions which enhance the anomalous transport and should therefore be avoided.

Since there are many different mechanisms which may drive instabilities, different theoretical methods are used in the investigations of these instabilities. Some can be adequately described by the two-fluid equations or even by MHD theory. These are in many ways similar to the macroinstabilities in their origin. However, they are normally confined to special regions of the plasma, especially in the plasma edge where the gradients are largest and there is (in fusion experiments) a strong influx of impurities from the wall of the vacuum chamber. Examples of these gradient-driven instabilities are the drift instability caused by density gradients and the Kelvin-Helmholtz instability which is driven by velocity shears where the electrical field has large gradients.

Other instabilities are due to non-Maxwellian distribution functions and must be treated by the Vlasov equation. A prime example of this is the two-stream or beam instability where charged particles are moving through a plasma with a speed comparable to the speed of sound in the plasma. Another is the "loss-cone" instability found in mirror machines where particles in a certain velocity range are lost at the ends of the machine. This distorts the velocity distribution and leads to instability.

One thing common to all studies of plasma turbulence is their nonlinear character. While the stability criteria for the various instabilities and their associated initial growth rates can normally be calculated by a linear analysis, the evolution of the instability leading to turbulent behaviour can only be described using the full nonlinear equations. This of course leads to almost insurmountable difficulties in doing precise analytical calculations. Therefore the theoretical study of turbulence in plasmas is often performed by numerical calculations. Here too, though, difficulties caused by the nonlinear character of the problems often manifest themselves.

On the experimental side the problems of doing accurate measurements of turbulence are seen immediately from the nonrepetitive character of turbulent fluctuations. Ideally, one would take a large number of "snapshots" in rapid succession of the relevant plasma parameters, such as the density and local potential in order

<sup>1</sup>In [1] the term *microinstability* is used only for instabilities caused by non-Maxwellian velocity distributions. Here, however, I have used it mainly to describe local instabilities compared with global instabilities which completely disrupt the plasma.

to follow coherent structures in the turbulence. However, such a measurement is not feasible. For one thing it would require the storing of an enormous amount of data. Furthermore, diagnostics such as probes which are the only ones to measure potentials accurately disturb the plasma and must be kept as small and few as possible. For these reasons measurements of plasma turbulence are of a statistical nature. Many measurements are made in a few points to obtain an averaged picture of the plasma turbulence.

The contents of this work are organised as follows: Chapter 2 describes experiments on plasma edge turbulence in the Risø Q-machine. These are caused by the Kelvin-Helmholtz instability. Statistical measurements are performed using Langmuir probes to reveal coherent structures in the turbulence. In chapter 3 is described an attempt at simulating the phenomena investigated experimentally in chapter 2. Spectral methods are used on a one-fluid equation. Problems with the numerical methods have not yet been completely solved but already results bear clear resemblance to experiments.

In chapter 4 is related the first experiments on the Risø DP-machine. This contains an unmagnetised plasma into which an ion beam can be injected. Measurements of the plasma response to perturbations of the beam reveals Čerenkov-like radiation patterns. Also, the beam instability is investigated in some detail.

Finally, chapter 5 contains a description of a large data-acquisition program developed by me and used for many of the experiments in this work. This is admittedly not what one would usually understand by plasma physics research. However, data acquisition using computers have by now become an integral part of experimental physics. Therefore I have thought is worthwhile to describe these efforts as they have been a necessary prerequisite for this work.

## 2 Experiments on edge turbulence in a Q-machine

### 2.1 Introduction

Studies of turbulence in magnetized plasmas have been performed in many different experimental machines with widely varying geometries (see for instance [2, 3]). These have most often been multipole devices or tokamaks. These experiments are hampered by the complexity of their geometries which makes it difficult to generalize from measurements in a few points, by the often short duration of the plasma and for tokamaks also the high temperatures of the plasma which make probe measurements impossible except in the scrape-off layer. In contrast to this the Q-machine features a simple geometry with a cold steady-state plasma in which measurements can be made anywhere. Of course it is by no means certain that the results obtained in a Q-machine will have any relevance to large toroidal devices. Still, there are indications that the phenomena observed in the Risø Q-machine and reported here are similar in structure and sometimes in physical origin to those observed in other machines.

Due to the physical nature of the plasma in the Q-machine (see next section) the emphasis here is on turbulence in the plane perpendicular to the magnetic field and the corresponding enhanced particle transport across field lines. This is of course also the topic of greatest interest for fusion-related work.

The work related in this chapter in reality consists of two distinct experiments, described in two papers[4, 5]. However, since there is some overlap between the two experiments, especially as the experimental set-ups were almost identical I will here treat them together and make no distinctions between the two. In addition some new results are presented here which have not yet been published.

### 2.2 Experimental set-up

#### Basic machine set-up and diagnostics

The experimental set-up consists of the Risø Q-machine which is outlined in Fig. 1. (In the following a basic knowledge of Q-machines is assumed.) It is a fairly standard Q-machine[6] operated in single-ended mode. The hot plate is made from tantalum and is heated by electron bombardment from behind (energy 1.5–2keV) to a temperature of up to app. 2200°C. In the other end of the plasma column the plasma is terminated by a cold metal plate. This can be biased relative to the vacuum chamber. Close to the end plate a small (8mm diameter) metal disc has been placed. This too can be biased independently.

Diagnostics in this machine consists of Langmuir probes[6, ch. 3]. These are spherical platinum probes of diameter 1mm. Only the tip is exposed to the plasma. The probe shaft is covered with two concentric glass tubes for electrical insulation. Between the glass tubes is a grounded metal tube. Depending on the experiment up to four probes are used at one time. Some are fixed in one or a few positions while others can be moved freely across the plasma column.

#### Basic plasma characteristics

In this machine a cesium plasma is used. The magnetic field strength can be varied in the region 0.1–0.6T. Depending on the cesium oven temperature and the hot plate temperature the plasma density is  $n = 10^{15} - 10^{16} \text{m}^{-3}$ , measured by ion saturation current to a probe. The plasma temperature is essentially determined

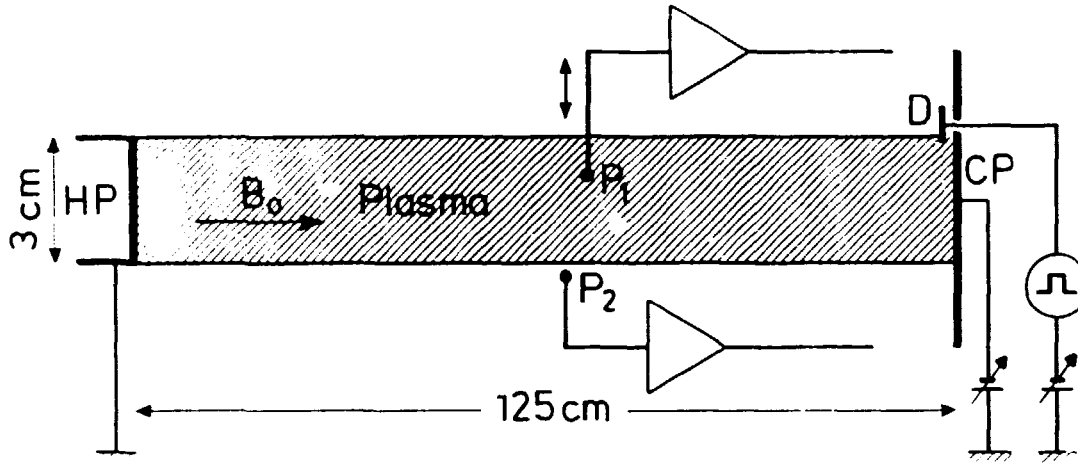


Figure 1. Schematic drawing of the Risø Q-machine. HP is the hot tantalum plate. CP is the cold end-plate which can be biased independently. D is the exciter disc and P1 & P2 are Langmuir probes.

by the hot plate temperature and so is  $T_e \approx T_i \approx 0.2\text{eV}$  where  $T_{i,e}$  is the ion and electron temperature, respectively. The temperature has been measured over the entire plasma column. It was found that there is no appreciable temperature variation across the plasma column. This is what one would expect since the plasma is not in contact with the walls and the mean free path for charge exchange is much greater than the diameter of the plasma column. There is thus no mechanism which preferably cools one part of the plasma. At the plasma parameters used here the plasma is electron rich and therefore the plasma potential is negative. The plasma potential is measured by the floating potential,  $V_f$  of a Langmuir probe. As the electron temperature is constant the plasma potential  $V_p$  is given by  $V_p \approx V_f - 4T_e = V_f - 0.8\text{V}$ . The plasma potential varies with the density and hot plate temperature but is generally  $\sim -3\text{V}$ .

In Fig. 2 is shown the density and floating potential of the probe in a cross-section of the plasma column. It is seen that the plasma potential is very nearly constant across the column and rises outside the main plasma. (The "main" plasma is here taken to be the part of the plasma where the magnetic flux tubes intersect the hot plate.) The constancy of the plasma potential inside the main plasma is caused by "hot-plate damping". Where the flux tubes impinge on the hot plate excess charge is "shortened out" as the hot plate is electrically conducting. (The argument is actually a little more involved because of the plasma sheath at the hot plate.)

The density profile is somewhat similar to the potential profile but more peaked. This is thought to be due to the fact that the temperature of the hot plate varies slightly across the plate and is highest in the middle. Variations in work function across the plate also influence the plasma density.

## 2.3 Measurements of turbulence in the plasma edge.

### Basic characteristics of the turbulent fluctuations

The original intent with the Q-machine concept was to produce a plasma free from large-scale instabilities and therefore free from noise (except thermal noise, of

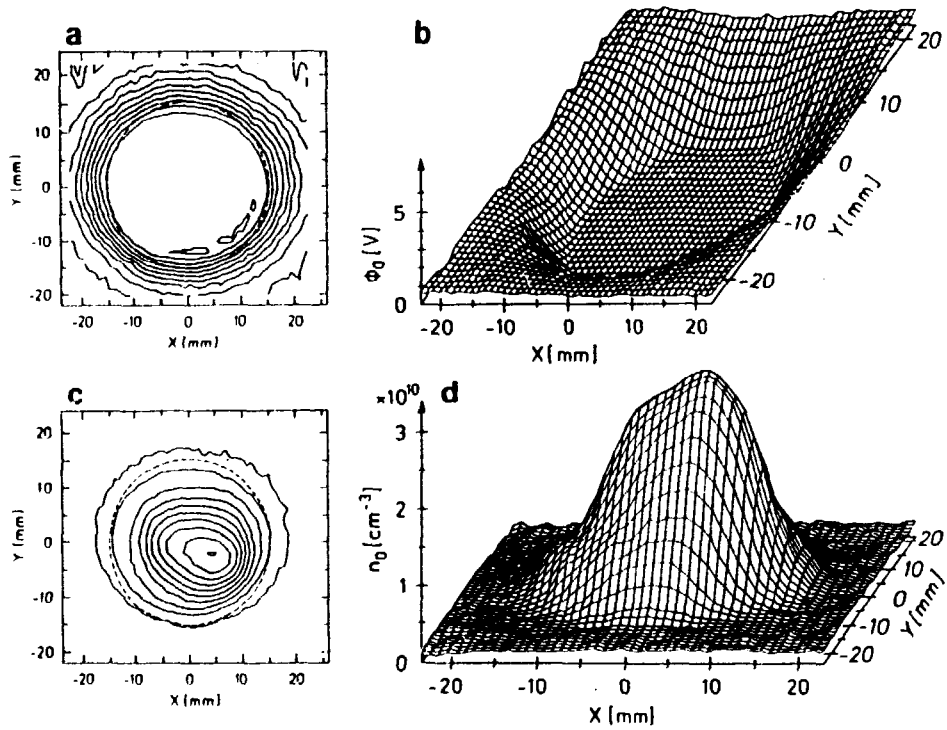


**Figure 2. a) & b) Probe floating potential  $V_f(\mathbf{r})$  across the plasma column. c) & d) Density variation  $n_0(\mathbf{r})$  over the column. The dashed circle shows the edge of the hot plate.**



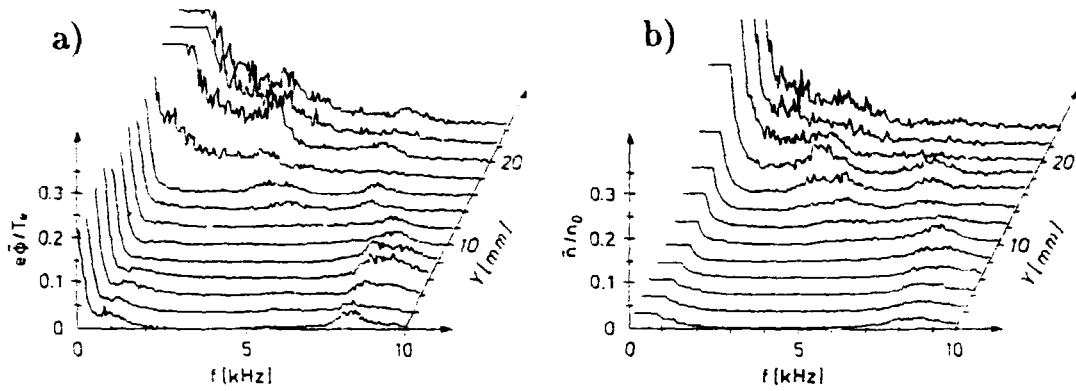


Figure 3. a) Spectra of the fluctuations in the plasma potential normalised by  $T_e/e$  for different radial positions  $Y$ . b) Similarly for the density fluctuations normalised by the local background density. The edge of the plasma is at  $Y = 15\text{mm}$ .

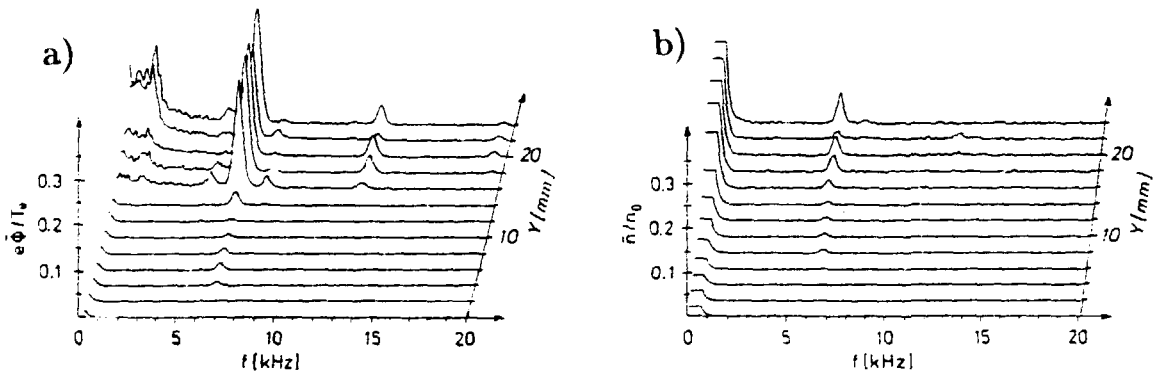


Figure 4. As previous figure, but this time for oscillations with a narrow frequency band. a) Potential fluctuations, b) density fluctuations.

course). In the main plasma column this has largely been achieved. However, in the edge of the plasma there are spontaneous low-frequency ( $\lesssim 20\text{kHz}$ ) fluctuations. That this should be so is not surprising. In the edge there are large density and potential gradients. Thus there is free energy which may drive an instability.

The spectrum of the fluctuations has been measured with a standard spectrum analyser. Density fluctuations were measured by the AC-signal to a Langmuir probe at ion saturation current, the potential fluctuations by the AC-signal to a floating probe. In Fig. 3 is shown for one set of plasma parameters the spectra of the fluctuations  $\bar{n}$  normalised by  $n_0(r)$  and  $\bar{\phi}$  normalised by  $T_e/e$  for various radial positions.

It is immediately seen that in the main plasma there is only a very weak signal at  $\sim 8\text{kHz}$ . However, in the plasma edge there are strong fluctuations with a broad low-frequency (up to  $5\text{kHz}$ ) spectrum. The very low frequency fluctuations found in the main plasma are thought to be noise due to outside sources.

The spectra in Fig. 3 were obtained at a specific set of plasma parameters.

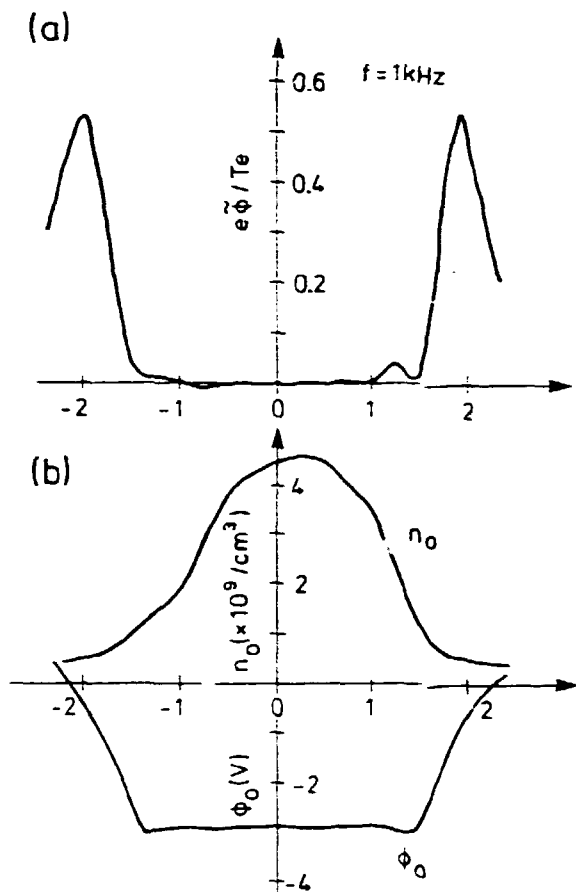


Figure 5. a) Fluctuation amplitude at 1kHz as a function of radial position.  
 b) DC density and potential profiles.

When the parameters are changed, different spectra are measured as can be seen from Fig. 4. Here the fluctuations in the edge are characterised by a narrow frequency peak at 5kHz and its harmonics. These are similar to those seen by other observers[7]. At still other parameters a hybrid between these two types of fluctuations may appear. The change between these regimes is thought to be due to changes in the potential gradient in the plasma edge. Thus a steep potential gradient gives a narrow frequency band while a less steep gradient gives a broader band spectrum. The potential gradient depends on many plasma parameters (hot plate temperature, density and magnetic field for instance) so it is not possible to give an exact description of how to obtain these different spectra.

#### Discussion of the physical origin of the fluctuations

The most conspicuous feature of the oscillations is that they are localized in the edge region of the plasma. In Fig. 5 is shown the fluctuation amplitude as a function of radial position (for the broad band case). For this figure the signal was band-pass filtered at 1 kHz. For reference the DC density and potential profiles are also shown. It is clearly seen that the fluctuation level is highest at the radial position where the potential gradient is largest and not where the density gradient is largest. This seems to indicate that it is the potential gradient that is the driving mechanism for the fluctuations in the edge. The electrical field gives rise to an azimuthal  $\mathbf{E} \times \mathbf{B}$  velocity. Since the electrical field is not homogeneous there will be

a velocity shear in the radial direction, exciting an instability. From fluid dynamics this is known as the *Kelvin-Helmholtz* instability. This has been investigated in detail by Kent et al.[7], mainly for the narrow band case shown in Fig. 4.

The nature of the fluctuations is revealed by a comparison between the two figures in Fig. 3. If the main plasma the fluctuation levels in the two figures are comparable in strength, that is, we can write  $e\tilde{\phi}/T_e \simeq \tilde{n}/n_0(r)$ , or in other words, that the electrons are isothermally Boltzmann distributed. These fluctuations are strongest at the position of the steepest density gradient. They are therefore interpreted as electrostatic drift waves [6-8]. These have a frequency

$$f_s = \frac{\omega_s}{2\pi} = T_e \frac{d \ln n}{2\pi e B_0 R}$$

which with parameters relevant for this experiment gives a frequency of the order of 5kHz, in fair agreement with experimental result.

In the edge region the relation between potential and density fluctuations is  $e\tilde{\phi}/T_e \gg \tilde{n}/n_0(r)$ . This indicates that the fluctuations are of the electrostatic *flute type* or *convective cell type*. This type of fluctuations is characterized by perturbations which are in phase along the magnetic field. In a cylindrical plasma they therefore resemble flutes on an ancient greek column, hence the name. In a homogeneous plasma the relation between density and potential fluctuations should be  $e\tilde{\phi}/T_e \simeq (k\lambda_D)^{-2} \tilde{n}/n_0$  [9]. For the present case where there is a density gradient a relation can be obtained between the ion density fluctuations and the potential fluctuations in the following way. The continuity equation for the ions is

$$\frac{\partial n}{\partial t} + \nabla \cdot (n\mathbf{v}) = 0. \quad (1)$$

It is assumed that there is no DC electrical field and that  $\mathbf{v}_0 = \mathbf{0}$ . In the low frequency range we can write

$$\tilde{\mathbf{v}} = -\nabla\phi \times \frac{\hat{\mathbf{e}}_z}{B_0}.$$

Standard vector relations give  $\nabla \cdot \tilde{\mathbf{v}} = 0$  and hence for Eq. 1 we find when linearising:

$$\frac{\partial \tilde{n}}{\partial t} + \tilde{\mathbf{v}} \cdot \nabla n_0 = 0$$

where  $n = n_0 + \tilde{n}$ . Considering only perturbations of the form  $ae^{i\mathbf{k}x - i\omega t}$  we get

$$\begin{aligned} -i\omega\tilde{n} - i \left( \mathbf{k}\tilde{\phi} \times \frac{\hat{\mathbf{e}}_z}{B_0} \right) \cdot \nabla n_0 &\simeq 0, \\ \frac{\tilde{n}}{n_0} &\simeq \frac{-\mathbf{k}\tilde{\phi} \times \hat{\mathbf{e}}_z \cdot \nabla n_0}{\omega B_0 n_0}. \end{aligned} \quad (2)$$

Finding  $\mathbf{k}$  from the fact that we are dealing with fluctuations with mode number  $m = 2$  (see next section) we find that  $\tilde{n}/n_0 \simeq 0.2e\tilde{\phi}/T_e$  in fair agreement with the results in Fig. 3.

That the fluctuations are really of the flute type was verified by measuring the phase of the fluctuations along the plasma column. It was found that at constant radial and azimuthal position there was no appreciable phase change along the field lines. Also, moving the end plate did not result in changes in the phase.

### Correlation measurements

In order to study the turbulence in greater detail measurements were made of the cross-correlation between the fluctuating quantities in space and time. The correlation measurements were made with two Langmuir probes. One was held at a fixed position while the other could be moved across the plasma column vertically and horizontally. In principle a cross-correlation function between two quantities  $A$  and  $B$  is given by:

$$R_{AB}(r_1, r_2, \tau) = \int_{t_0}^{t_1} A(r_1, t)B(r_2, t + \tau)dt \quad (3)$$

where  $t_1 - t_0$  is a long time interval (compared with typical time scales for the signals). At the time when these measurements were made we did not have equipment to measure accurately long time series of the signals in real time. The measurement was therefore done with a box-car averager. This samples the two signals (with a time difference of  $\tau$ ) and multiplies them. This is repeated at fairly long time intervals (5-20ms) and the results are averaged. Because of the long time interval between each measurement the different measurements are statistically independent of each other. The average (taken over a total of app. 3 seconds) is therefore a good approximation to an ensemble average. By moving one probe around in the plasma a complete correlation function can be obtained. This is shown in Fig. 6. Here is shown the cross-correlation  $R_{\phi\phi}(r_1, r_2, \tau)$  for four different values of  $\tau$ . These measurements (and the following) were made in a square area with around  $20 \times 45$  measuring points. From Fig. 6 one may note many interesting features. First, we see from Fig. 6a that the turbulent fluctuations are fairly homogeneous in the azimuthal direction, with an approximate mode number  $m = 2$ , i.e. the figure depends only on the absolute separation angle between the probes and not on their exact position. In the radial direction, the fluctuations are not at all homogeneous. This is not surprising when comparing with Figs. 3 and 5, where it is seen that the level of fluctuations depends strongly on radial position. The correlation length is also much shorter in the radial direction. In the azimuthal direction the correlation length is approximately half a circumference.

Most prominently, the figures clearly show convective cells moving around the circumference of the plasma column. It is also seen that regions of positive correlation are followed by regions of negative correlation, indicating a number of convective cells of changing polarity around the circumference. In Fig. 7 is shown the azimuthal position of the convective cells as a function of time. From this figure the velocity can be calculated. This value is estimated at  $v \approx 200\text{ms}^{-1}$ . From Fig. 2 an electrical field strength can be estimated in the region of the convective cells of Fig. 6. The radial correlation length is app. 9mm and the estimated electrical field is  $85\text{Vm}^{-1}$ . With a magnetic field strength of 0.35T this gives an  $\mathbf{E} \times \mathbf{B}_0/B_0^2$  drift velocity of  $240\text{ms}^{-1}$ . There is thus good reason to claim that the convective cells are transported around the plasma column by  $\mathbf{E} \times \mathbf{B}$  drift.

Information about the turbulence can also be obtained from cross-correlations between density measurements and between potential and density. This is shown in Fig. 8, still for the broad band case.

The first thing to be noted from this figure is that the fluctuations in the edge are clearly correlated with those in the main plasma. That this should be so is not obvious. As was argued in sec. 2.3 the driving mechanisms are different for the two types of fluctuation: There must then be some coupling mechanism linking the fluctuations. This coupling is thought to be carried out by the ions since these gyrate with a fairly large Larmor radius ( $\sim 2\text{mm}$ ). Thus, by this coupling the edge fluctuations may drive the drift waves in the main plasma unstable. The

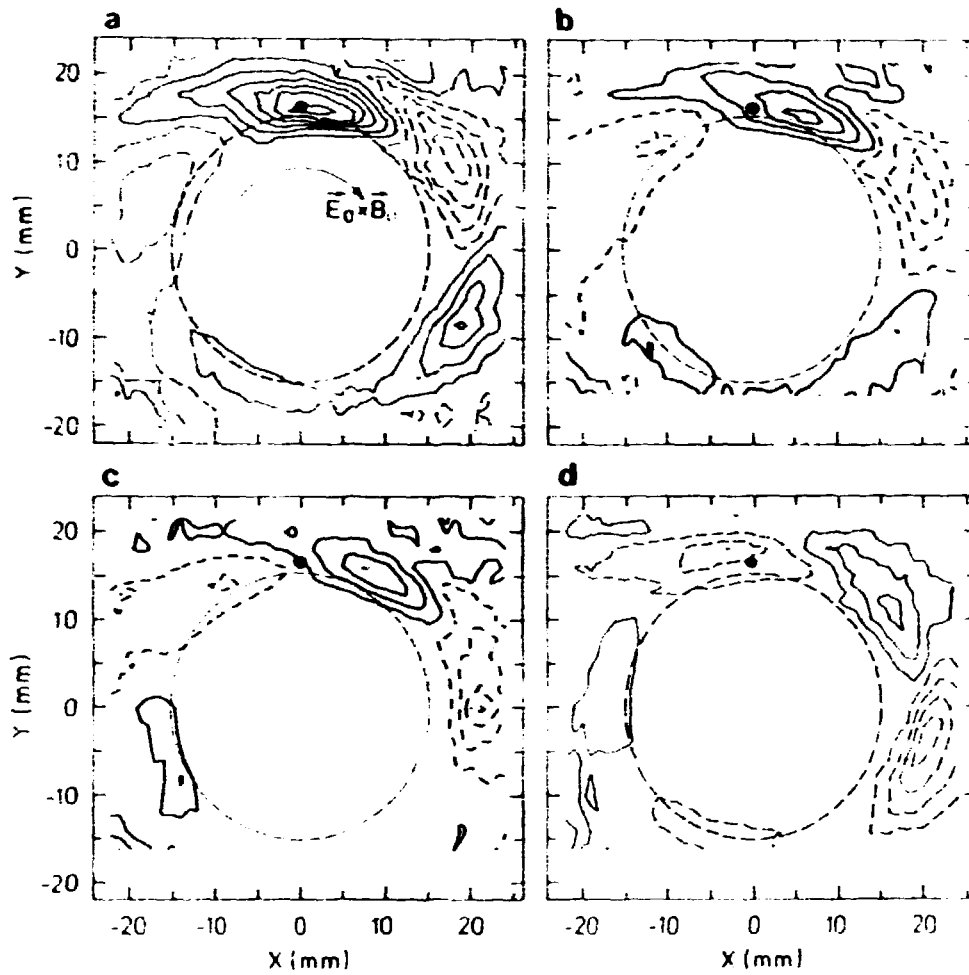


Figure 6. Contour plots of the cross correlation function  $R_{\phi\phi}(r_0, r, \tau) = \langle \tilde{\phi}(r_0, t) \tilde{\phi}(r, t + \tau) \rangle$  for four different values of  $\tau$ , a)  $\tau = 0\mu s$ , b)  $\tau = 25\mu s$ , c)  $\tau = 50\mu s$  and d)  $\tau = 100\mu s$ . Solid contours indicate a positive correlation, dashed contours are negative.  $r_0$  is marked with a  $\bullet$ . Again, the dashed circle marks the extent of the hot plate. For this figure plasma parameters were  $B_0 = 0.35 T$ ,  $n_0(\tau = 0) = 10^{16} m^{-3}$ . The magnetic field vector points into the plane.

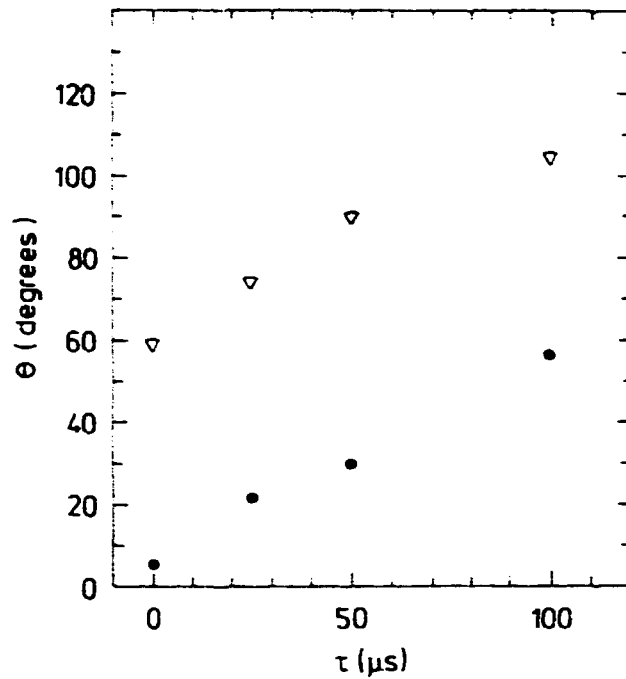


Figure 7. Azimuthal position (angle  $\theta$ ) of the convective cells of the previous figure as a function of  $\tau$ . The positions of one positive cell are marked with  $\nabla$ , those of a negative cell with  $\bullet$ .

mechanism is thought to be the following: The drift instability is not very strong at the plasma parameters in this experiment. Due to end losses the growth rate is further diminished, and so the drift modes may not be unstable at all but on the other hand they are at most weakly damped. The edge fluctuations have a broad spectrum and thus they contain the resonance frequency for the drift waves in the main plasma. Thus the drift waves can be driven by the edge fluctuations.

From the phase relations between the density and potential fluctuations several interesting features of the turbulence can be found. In Fig. 8 is clearly seen that the potential and density are in counterphase (anti-correlated) at the position of the reference probe (the  $\bullet$  in the figure). This is not what one would expect from a simple analysis of flute-type oscillations, where the density is in phase with the electrical field and therefore  $90^\circ$  out of phase with the potential ( $\vec{E} = ik\phi$ ). The simple analysis is also the one giving the maximum growth rate of the instability. However, the fluctuations seen in this experiment are subject to a non-linear interaction, which damps the instability by changing the phase relation. This damping is partly due to finite Larmor radii. An analysis by Chen[10] shows that in the saturated fluctuations the electrical field should be  $90^\circ$  out of phase with the density and therefore the potential should be in counterphase with the density. This analysis is corroborated by the data in Fig. 8. However, though the potential and density are anti-correlated they are not exactly in counterphase as the local minimum for the correlation function is not at the point of the reference probe.

The situation is different in the main plasma. Here it is found that the potential fluctuations in the main plasma are in phase with the density fluctuations at the same azimuthal position. Also the density fluctuations are in phase. Therefore the potential and density fluctuations in the main plasma must be in phase too. This is what is expected for resistive drift modes.

The correlation analysis was also performed for plasma parameters where the fluctuation spectrum has a narrow peak (Fig. 4). The results are shown in Fig. 9.

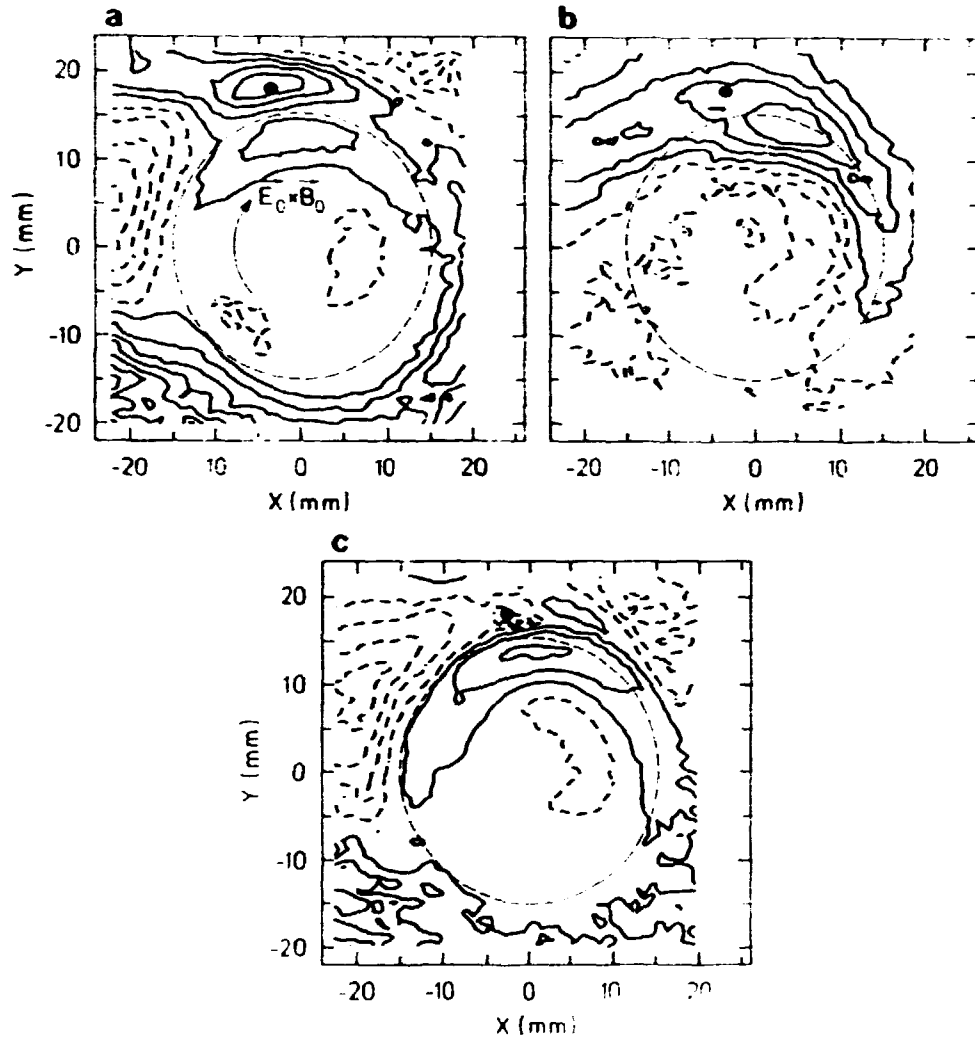


Figure 8. Contour plots of various cross correlation functions. a)  $R_{\phi\phi} = \langle \tilde{\phi}(x_0, t) \tilde{\phi}(x, t) \rangle$ , b)  $R_{nn} = \langle \tilde{n}(x_0, t) \tilde{n}(x, t) \rangle$ , c)  $R_{n\phi} = \langle \tilde{n}(x_0, t) \tilde{\phi}(x, t) \rangle$ . As in Fig. 6, only  $n_0(\tau = 0) = 3 \cdot 10^{16} m^{-3}$  and  $B_0 = 0.28 T$ .

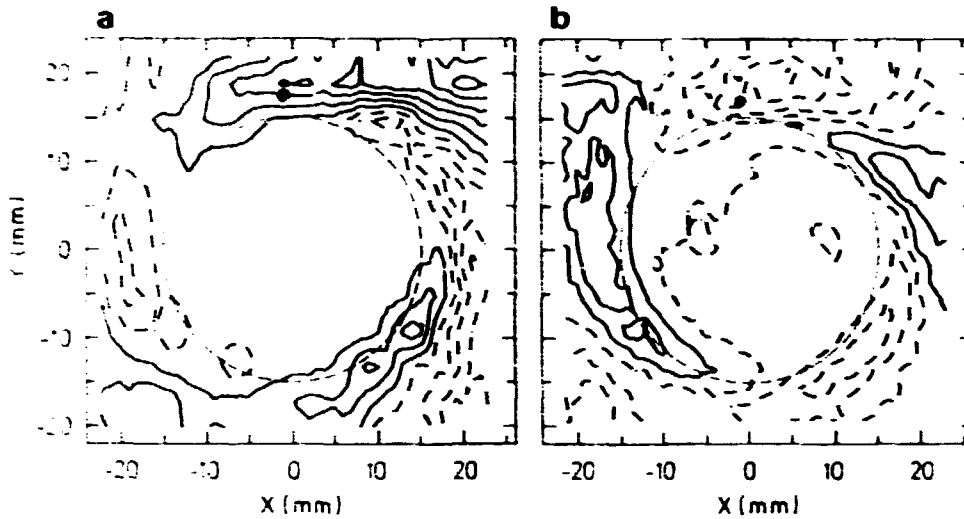


Figure 9. Contour plots of cross correlation functions for narrow band fluctuations. a)  $R_{\phi\phi} = \langle \tilde{\phi}(r_0, t) \tilde{\phi}(r, t) \rangle$ , b)  $R_{n\phi} = \langle \tilde{n}(r_0, t) \tilde{\phi}(r, t) \rangle$ .

From this figure it is easy to see that around the plasma column are two areas of positive correlation and two of negative correlation. Thus the oscillations have an azimuthal mode number  $m = 2$ . Furthermore, here the density and potential are very nearly in counterphase. This is in agreement with the experimental results of Kent et al.[7].

## 2.4 Interaction between the turbulence and an injected convective cell

In the preceding discussion the turbulent fluctuations are generated spontaneously and therefore the properties of the turbulence are independent of the time of measurement. Furthermore, the statistical nature of the measurements means that the interaction between specific structures in the turbulence cannot be studied. By perturbing the plasma one can study the interaction between this perturbation and the spontaneously generated turbulence. Such a perturbation was made with the exciter disc placed at the end plate of the Q-machine (see Fig. 1). The exciter is placed at a radial and azimuthal position close to the fixed reference probe. The perturbation was made by applying a positive voltage pulse to the disc, thereby drawing electrons out of the flux tube impinging on the disc. In other words, a convective cell is injected into the plasma. Typically, the applied voltage was +12V for 20 $\mu$ s. The repetition rate was 100Hz, which is much longer than the correlation time. Correlation functions were measured as in the previous section, only here the time of measurement was triggered by the injection of the convective cell.

### Broad band case

In these measurements the fluctuation spectrum was broad as in Fig. 3. For this situation correlation measurements were made. In Fig. 10 is shown the cross correlation function  $R_c(t_1, t_1) = \langle \tilde{\phi}(r_0, t_1) \tilde{\phi}(r, t_1) \rangle$  for various values of the time  $t_1$  after the injection of the cell. It is seen that the correlation function essentially retains its form in this time interval while the amplitude varies strongly. In Fig. 11



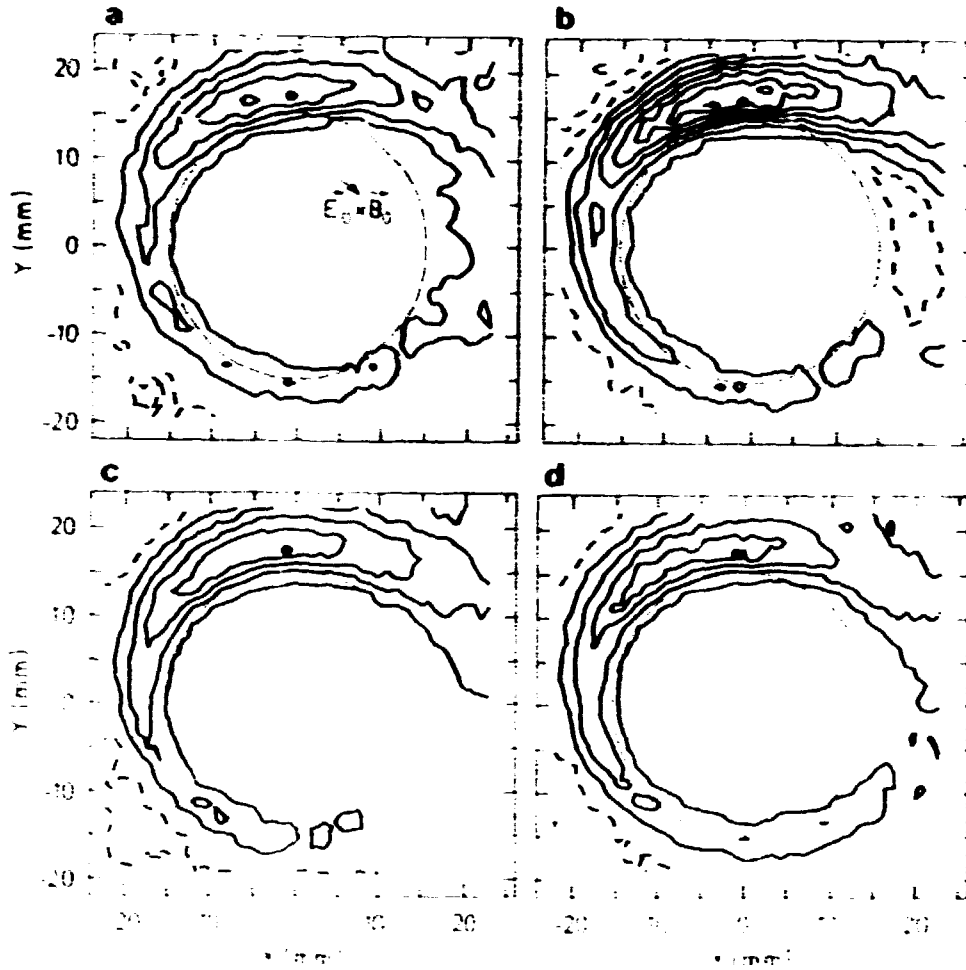


Figure 10. Correlation function  $R_c(t_1, t_1) = \langle \tilde{\phi}(x_0, t_1) \tilde{\phi}(x, t_1) \rangle$ , where  $t_1$  is the time after the injection into the plasma of a positive convective cell, for four different values of  $t_1$ . a)  $t_1 = 30 \mu s$ , b)  $t_1 = 70 \mu s$ , c)  $t_1 = 150 \mu s$ , d)  $t_1 = 400 \mu s$ .

is shown the time evolution of  $R_c(t_1, t_1)$  for different azimuthal positions at a fixed radial position of  $r = 16 \text{ mm}$ . The disturbance due to the convective cell is clearly seen. It grows within  $t_1 \approx 50 \mu s$  and is completely damped out at  $t_1 = 500 \mu s$ .

In order to understand the interaction between the background fluctuations and the injected cell the contributions of the two components to the correlation function must be clearly identified. If the fluctuating potential is written as  $\tilde{\phi}(r, t) = \phi_R(r, t) + \phi_c(r, t)$ , the subscript  $R$  denoting the background fluctuations, the correlation function can be written

$$R_c(t_1, t_1) = \langle \phi_R(x_0, t_1) \phi_R(x, t_1) \rangle + \phi_c(x_0, t_1) \phi_c(x, t_1) \\ + \langle \phi_R(x_0, t_1) \rangle \phi_c(x, t_1) + \phi_c(x_0, t_1) \langle \phi_R(x, t_1) \rangle. \quad (4)$$

$\phi_c$  is not averaged since it must be the same in all statistically independent realizations. Now, if  $\phi_c$  and  $\phi_R$  are statistically independent, that is if the injected cell is simply superimposed on the background turbulence, then the average potential will be  $\langle \tilde{\phi} \rangle = \phi_c$ , whereby Eq. 4 becomes

$$R_c(t_1, t_1) = R(x_0, x, 0) + \phi_c(x_0, t_1) \phi_c(x, t_1). \quad (5)$$

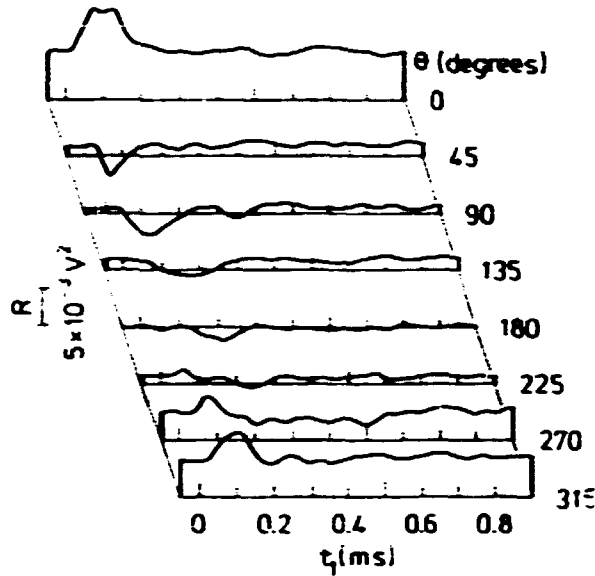


Figure 11. Time evolution of the correlation function as in Fig. 10 for different azimuthal positions at the radial position  $r = 16\text{mm}$ .

$R(r_0, r, 0)$  being the standard potential cross correlation function for zero time delay. Fig. 10 suggests that the injected cell is not simply superimposed on the turbulence. This becomes even more clear in Fig. 12. Here is shown first the correlation function  $R_c$  and the correlation function with no cells injected. Then the two are subtracted. Finally is shown  $\langle \tilde{\phi}(r_0, t_1) \tilde{\phi}(r, t_1) \rangle$ , which would be equal to  $\phi_c(r_0, t_1) \phi_c(r, t_1)$  if the cell and the turbulence did not interact. In that case Figs. 12c & d would be identical. Since they clearly are very different it can be concluded that the cell interacts nonlinearly with the background turbulence. These results confirm similar findings by eg. Pécseli et al.[11]. The increase in the correlation function indicates that the energy of the injected cell is condensed in the lowest order modes,  $m = 0$  and  $m = 1$ . Thus the convective cell modifies the turbulence, making energy flow from high order modes into larger structures.

#### Narrow band case

The experiments discussed in the previous section were also performed for plasma parameters where the fluctuations have a narrow band spectrum as in Fig. 4. Here the fluctuations are much more coherent and it is possible to study in greater detail the interaction between the spontaneous fluctuations and an externally excited convective cell. In Fig. 13 is shown the correlation function  $R_c(t_1, t_1) = \langle \tilde{\phi}(r_0, t_1) \tilde{\phi}(r, t_1) \rangle$  at different times after the injection of the cell. These figures indicate that as long as the cell exists the oscillations are essentially  $m = 1$  modes whereas the background fluctuations without the injected cell have  $m = 2$ . How the background fluctuations are perturbed by the convective cell can be seen from Fig. 14. This shows the time evolution of the average potential fluctuation  $\langle \tilde{\phi} \rangle$  before and after the injection of the cell, for a number of azimuthal positions around the plasma column. As the cells are injected at random time points relative to the background fluctuations, the average potential before the injection is very close to zero. Immediately after the injection the cell is seen, and after the cell has decayed (at 200–300  $\mu\text{s}$ ) the inherent fluctuations reappear. However, the phase of the background fluctuations is locked to the cell even after the cell has

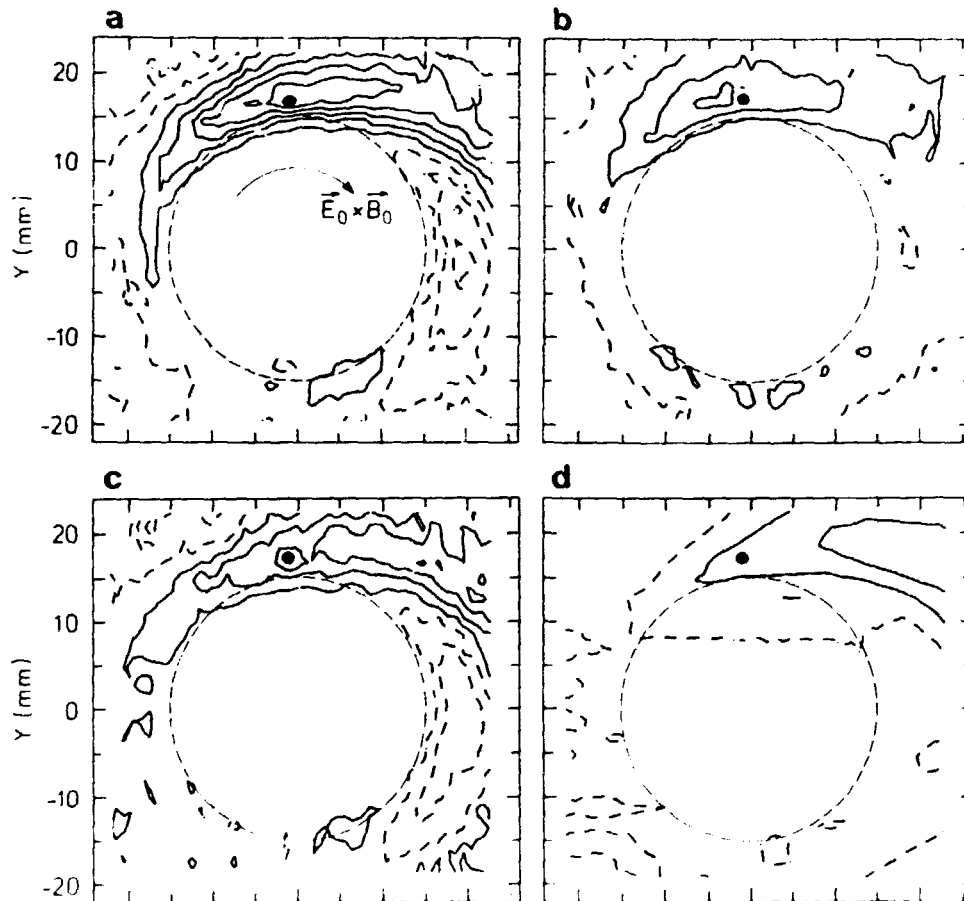


Figure 12. a) Correlation function as in Fig. 10, for  $t_1 = 100\mu s$ . b) Same set-up, but without cell injection. c) Subtraction of a) and b). d)  $\langle \tilde{\phi}(\mathbf{r}_0, t_1) \rangle \langle \tilde{\phi}(\mathbf{r}, t_1) \rangle$ .

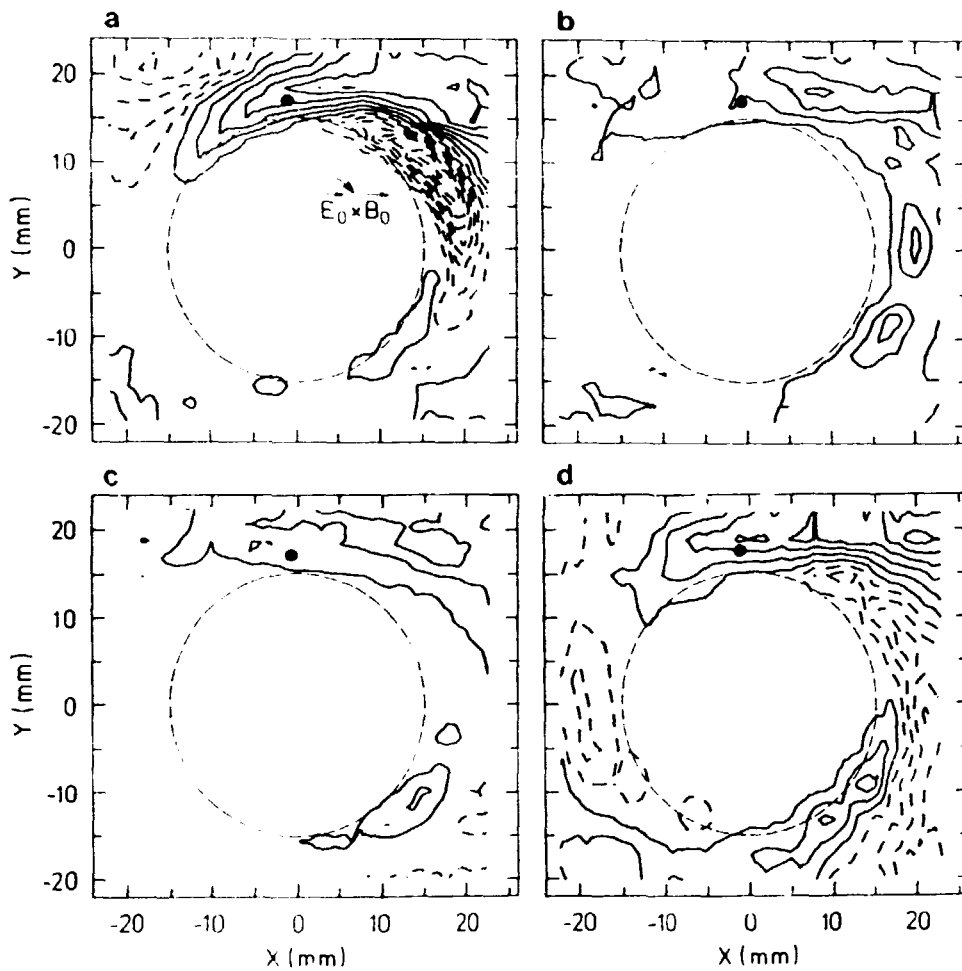


Figure 13. Correlation function  $R_c(t_1, t_1) = \langle \tilde{\phi}(\mathbf{r}_0, t_1) \tilde{\phi}(\mathbf{r}, t_1) \rangle$ , for a case when the spectrum of the fluctuations has a narrow peak. Figure is analogous to Fig. 10. a)  $t_1 = 70 \mu s$ , b)  $t_1 = 150 \mu s$ , c)  $t_1 = 400 \mu s$ , d) Correlation function for the unperturbed plasma.

decayed and so the average potential is nonzero. Thus the cell affects the coherent oscillations for much longer than the lifetime of the cell.

A further examination of this was carried out to determine the relation between the injection time (relative to the inherent mode) and the phase shift. For this measurement the injection time was triggered by the inherent fluctuations. The average potential was then measured at a fixed azimuthal position  $\theta = 90^\circ$ . The results are shown in Fig. 15. This figure clearly shows that the modification of the phase depends on the phase of the injection. When the cell is injected in phase with the fluctuations the phase is not appreciably changed. The maximum phase change comes when the cell is injected  $90^\circ$  out of phase with the inherent mode.

The evolution of the plasma response to the injected cell is shown in Fig. 16 as a function of the azimuthal position. Again, there are clear differences between the cases A and B of Fig. 15. Of special interest is Fig. 17, which shows the Fourier components of a series of curves as those in Fig. 16. The Fourier components can here be considered as "modes" and Fig. 17 then shows the relative strength of the different modes as a function of time after the cell injection. This interpretation of the Fourier components as "modes" should be taken with some caution as the lifetime of these modes is comparable to the frequency of the oscillations.

The most important result to be seen from Fig. 17 is that, after the cell has

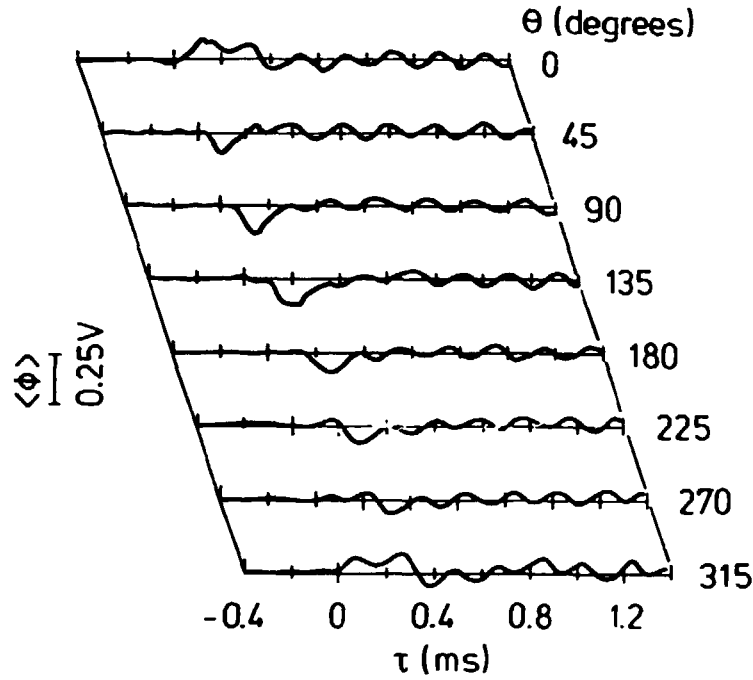


Figure 14. Time evolution of the averaged potential  $\langle \bar{\phi} \rangle$  at various azimuthal positions at the radial position  $r = 18\text{mm}$ . A convective cell is injected at  $t=0$ .

been injected the low order modes ( $m = 0$  and  $m = 1$ ) grow while the inherent  $m = 2$  mode is quenched in the period  $200\mu\text{s} < t < 300\mu\text{s}$ . This indicates that the cell perturbs the inherent mode in a way such as to precipitate an inverse cascade of energy from high to low modes. Furthermore, even when the cell has decayed at  $t > 400\mu\text{s}$  the inherent mode does not retain its former strength for several hundred  $\mu\text{s}$ . This feature is most clearly seen in Fig. 17a pertaining to cell injection in phase with the inherent fluctuations. When the injection is out of phase the picture is less clear. In this case higher modes ( $m \geq 3$ ) are also excited and the  $m = 2$  mode is strongly enhanced in the first  $100\mu\text{s}$  after the cell injection. However, also here the high order modes are quenched for a period after this initial response. The fact that in both cases the  $m = 2$  mode does not fully recover until long after the cell has decayed indicates that there may be some interaction between the modes for this extended period.

## 2.5 Anomalous plasma transport

Due to the randomly varying electrical field, the plasma will be transported with a local velocity  $\bar{v} = \bar{E} \times \mathbf{B}_0 / B_0^2$  (as long as frequencies are much lower than the ion cyclotron frequency). The plasma flux associated with this velocity can be written as  $\bar{\Gamma} = \bar{n}\bar{v}$ . Note that  $\bar{\Gamma}$  does not contain the DC flux in the azimuthal direction. The interesting part of the flux is the transport out of the plasma column, which may be termed an anomalous diffusion, since it gives rise to a diffusion across the field lines which is not of the classical type. The anomalous radial transport will in the following be called  $\bar{\Gamma}_0 = \bar{n}\bar{E}_\theta / B_0$ . A positive value of  $\bar{\Gamma}_0$  corresponds to flux out of the plasma column.

To calculate the flux it is necessary to measure the local fluctuations in the

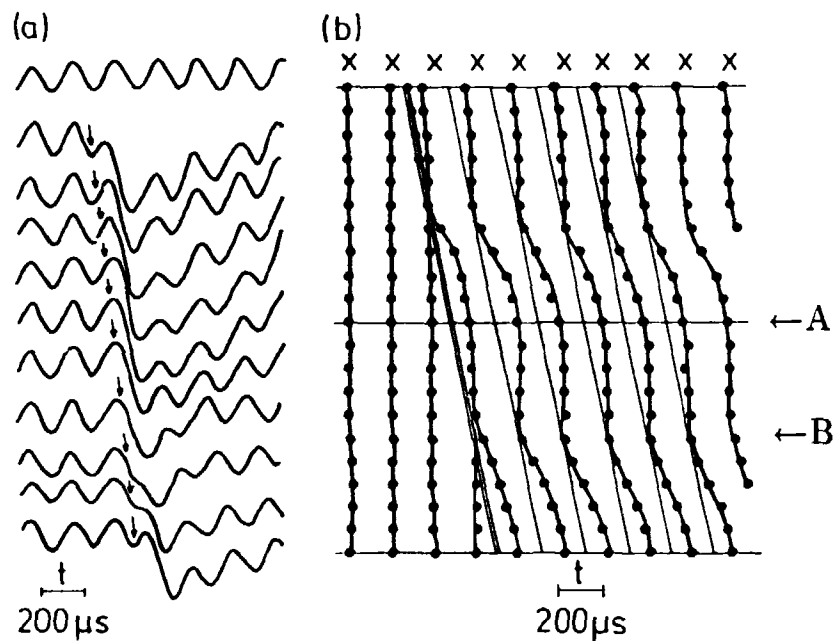


**Figure 15.** Time evolution of the average potential fluctuations when an convective cell is injected. Measurements are here triggered by the inherent fluctuations. a) The time evolution at a fixed point ( $\theta = 90^\circ$ ) for different injection times (indicated by arrows). Top trace shows background fluctuations alone. b) Trace of the peaks in the signal shown in a). In A the cell is injected out of phase with the background mode, in B the injection is in phase. The oblique line shows the time of injection.

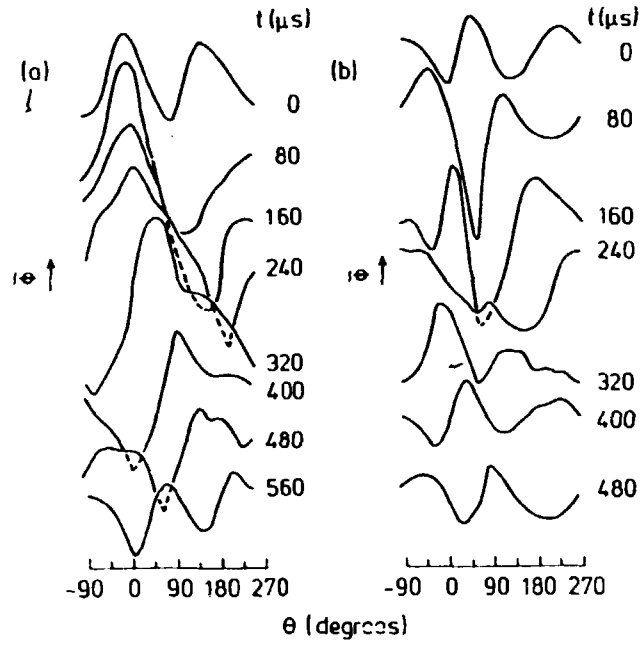


Figure 16. Potential variation as a function of azimuthal position for various times  $t$  after the cell injection. In a) the cell is injected in phase with the inherent fluctuations, in b)  $90^\circ$  out of phase. This corresponds to the cases A and B in Fig. 15.

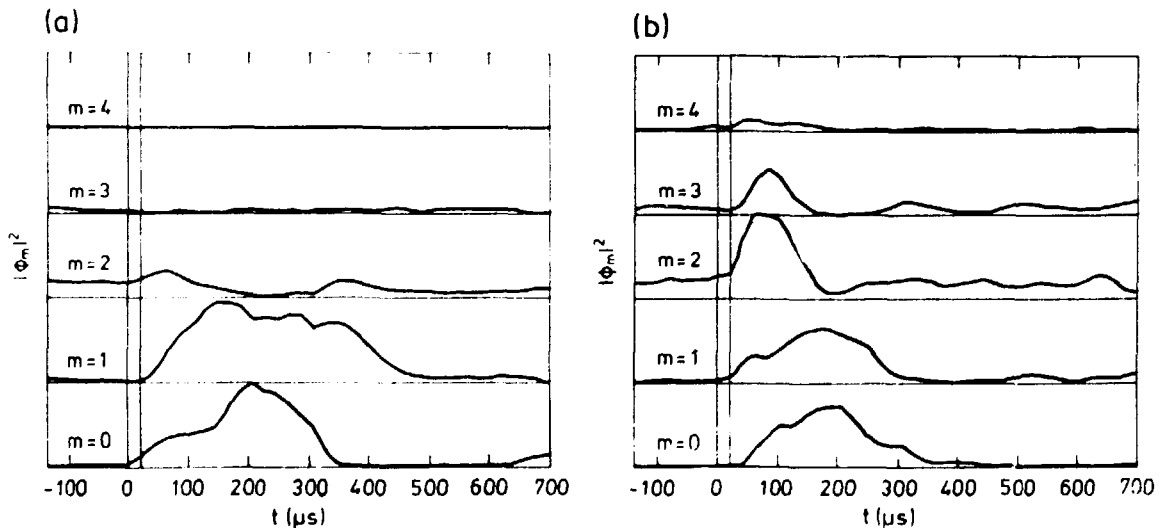


Figure 17. Temporal evolution of the azimuthal mode numbers  $m = 0$  to  $m = 4$  (of the potential). a) shows case A of Fig. 15, b) is for case B.

electrical field and the density simultaneously at approximately the same radial and azimuthal position. This was done using three probes entered from the side of the machine. Two of these were placed at  $r = 17\text{mm}$  and  $10\text{mm}$  apart in the azimuthal direction and left floating. The potential difference then gives the azimuthal electric field. The distance between the probes is large enough that the probe sheaths do not overlap but small enough compared to the scale size of the turbulence that aliasing errors are not significant. To ensure that the measured electrical field really only is the azimuthal component the two probes were fine-adjusted until the DC voltage between them vanished. Between the two floating probes is placed a third probe biased for ion saturation current. This measures the fluctuating density. The fluctuating radial flux is then measured by multiplying the signal from the density probe and the  $E$ -field probes.

### Results with broad band turbulence

The first investigation is in a situation where the turbulence has a broad frequency spectrum as shown in Fig. 3. Using a Hewlett-Packard analog correlator probability densities were obtained for the fluctuating quantities. The results are shown in Fig. 18. From this figure we can see that  $\langle \tilde{n} \rangle = \langle \tilde{E} \rangle = 0$ , as expected. However, the flux has a non-zero average, indicated by the arrow in Fig. 18c. The average flux can thus be measured to  $\langle \tilde{\Gamma}_0 \rangle = 1.1 \cdot 10^{16} \text{m}^{-2} \text{s}^{-1}$ . In addition to this it is seen that while the density and electrical field probability distributions are almost Gaussian distributions the flux distribution is markedly asymmetric. From the figure we find a skewness of  $\sim 0.3$  and a kurtosis of  $\sim 4$ . The positive value of  $\langle \tilde{\Gamma}_0 \rangle$  indicates a net flux out of the plasma column. From this a diffusion coefficient can be defined as  $D_a = \langle \tilde{n} \tilde{v} \rangle / |\nabla n_0|$ , from which  $D_a = 3 \cdot 10^{-3} \text{m}^2 \text{s}^{-1}$ . Compared to the Bohm diffusion coefficient  $D_B = \kappa T / q B_0 = 4 \cdot 10^{-2} \text{m}^2 \text{s}^{-1}$  it is somewhat lower, but it is more than an order of magnitude larger than the classical diffusion coefficient,  $D_c = 2\eta T n / B_0^2 = 1.7 \cdot 10^{-4} \text{m}^2 \text{s}^{-1}$  ( $\eta$  is given by Spitzer[12]:  $\eta = 5.22 \cdot 10^{-5} \ln \Lambda / T^{3/2}$  and  $\ln \Lambda \simeq 15$ ). The transport along the field lines can also be calculated. Using a plasma velocity of  $500 \text{ms}^{-1}$  the plasma flux along the field lines is  $5 \cdot 10^{19} \text{m}^{-2} \text{s}^{-1}$ . If the radial flux is assumed to be constant along the plasma column, the total radial transport is  $1.2 \cdot 10^{15} \text{s}^{-1}$  while the longitudinal transport is  $3.5 \cdot 10^{16} \text{s}^{-1}$ ; in other words about 3% of the plasma is lost radially while the rest is lost by condensing on the end plate.

The processes giving rise to the anomalous diffusion can be investigated in more detail by measuring the autocorrelation functions of the fluctuating quantities. In Fig. 19 is shown the autocorrelation functions  $R_{\tilde{n}}(\tau) = \langle \tilde{n}(t) \tilde{n}(t + \tau) \rangle$ ,  $R_{\tilde{E}}$  and  $R_{\tilde{\Gamma}}$ . While the autocorrelation of  $\tilde{n}$  and  $\tilde{E}$  tend to zero for  $\tau \rightarrow \infty$ ,  $R_{\tilde{\Gamma}}$  tends to a constant nonzero value. The average flux can then be calculated as  $\langle \tilde{\Gamma}_0 \rangle = \sqrt{R_{\tilde{\Gamma}}(\tau \rightarrow \infty)}$ . The value found by this method is close to the one found from Fig. 18. In Fig. 19d is shown the cross correlation function  $R_{\tilde{n} \times \tilde{E}}(\tau)$ . From this it is easily seen that  $\tilde{n}$  and  $\tilde{E}$  are significantly correlated. The normalised correlation is  $R_{\tilde{n} \times \tilde{E}}(0) / (R_{\tilde{n}}(0) R_{\tilde{E}}(0)) \simeq 0.3$ .

A Fourier transform of  $R_{\tilde{n} \times \tilde{E}}$  in time will yield the power spectrum of the flux, using the convolution rule:

$$F(a(t) \cdot b(t)) = \int F(a(t)) F(b(t + \tau)) d\tau.$$

The spectrum is written as  $S(f = \omega/2\pi) = |S(f)| e^{i\Psi(f)}$ . In Fig. 20 is shown  $|S(f)|$  and  $\Psi(f)$ . From the phase spectrum it can be seen that for high frequencies the phase difference between  $\tilde{n}$  and  $\tilde{E}$  is close to zero, but for the lowest frequencies the phase difference is closer to  $\pi/2$ . It will be recalled that according to Chen[10]



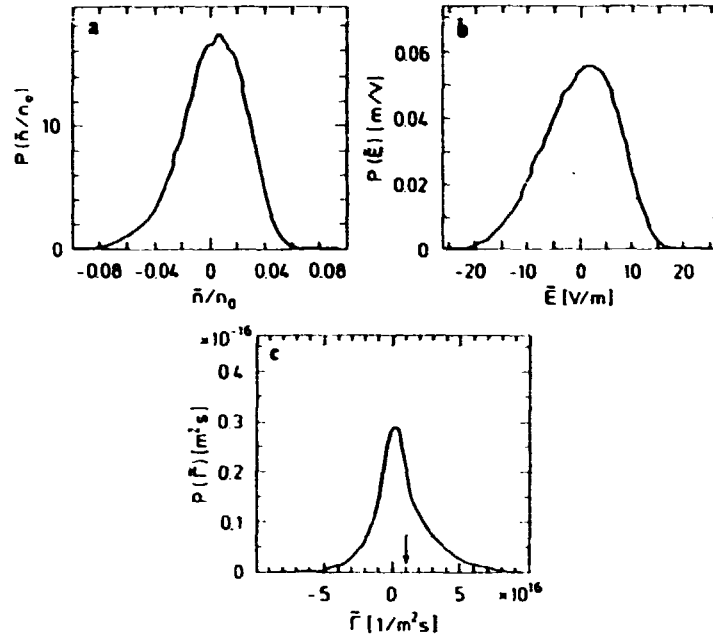


Figure 18. Probability densities (relative occurrence of different instantaneous values) for the fluctuating quantities. a) Normalised density, b) azimuthal electric field, c) radial flux  $\tilde{\Gamma}_0$ . In this experiment  $B_0 = 0.25 T$ ,  $n_0 \approx 5 \cdot 10^{16} m^{-3}$ .

the phase relation should be zero for linear instability but  $\pi/2$  for the saturated fluctuations. Thus Fig. 20 gives a further indication that energy is cascading from high order modes to lower ones. The high frequency modes will then remain linearly unstable because their energy is fed into the lower order modes which then are driven into saturation. It should be noted here, that while  $\Psi(f) \approx 0$  was always observed for the high modes the phase of the low frequency modes was sometimes  $-\pi/2$  rather than  $\pi/2$ .

As the phase of the low frequency modes is close to  $\pi/2$  these modes should not contribute to the net outward flux. That this is indeed so was verified explicitly by filtering the  $\tilde{n}$  and  $\tilde{E}$  signals with a high-pass filter before multiplying them. It was found that the net outward flux,  $\langle \tilde{\Gamma}_0 \rangle$  was not appreciably affected, when the cut-off frequency was below  $\sim 2 kHz$ . However, for higher cut-off frequencies the net flux decreased. This result is somewhat surprising, since the amplitude of these low frequency modes is rather high compared to the high frequency modes.

#### Narrow band case

The preceding investigation was also carried out for a narrow frequency band regime, such as the one seen in Fig. 4. Probability distributions were also obtained for this case for the three fluctuating quantities. Here it was found that the probability distribution for the density,  $P(\tilde{n})$  closely resembled that of a purely sinusoidal oscillation with amplitude  $A$ :  $P(a) = (A/\pi)/\sqrt{(A^2 - a^2)}$  for  $a < A$ , 0 otherwise. There was a bit of "smearing out" due to the very low frequency noise component which is always present. This in fact dominated the result in  $P(\tilde{E})$ . The probability distribution for the radial flux was again asymmetrical, but with a much lower average outward transport.

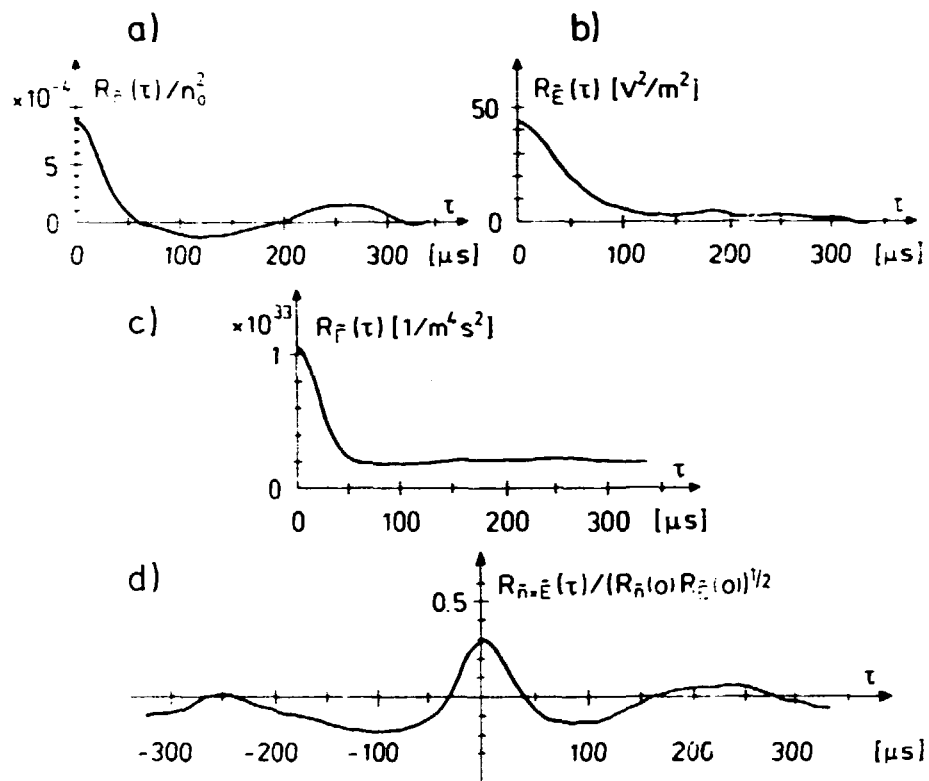


Figure 19. Autocorrelation functions for the fluctuating quantities, a)  $R_{\tilde{n}}(\tau) = \langle \tilde{n}(t)\tilde{n}(t+\tau) \rangle$ , b)  $R_{\tilde{E}}$ , c)  $R_{\tilde{F}}$ . d) Cross correlation function between  $\tilde{n}$  and  $\tilde{E}$ ,  $R_{\tilde{n}\tilde{E}}(\tau) = \langle \tilde{n}(t)\tilde{E}(t+\tau) \rangle$ , normalised by  $R_{\tilde{n}}(0)R_{\tilde{E}}(0)$ . Parameters as in Fig. 18.

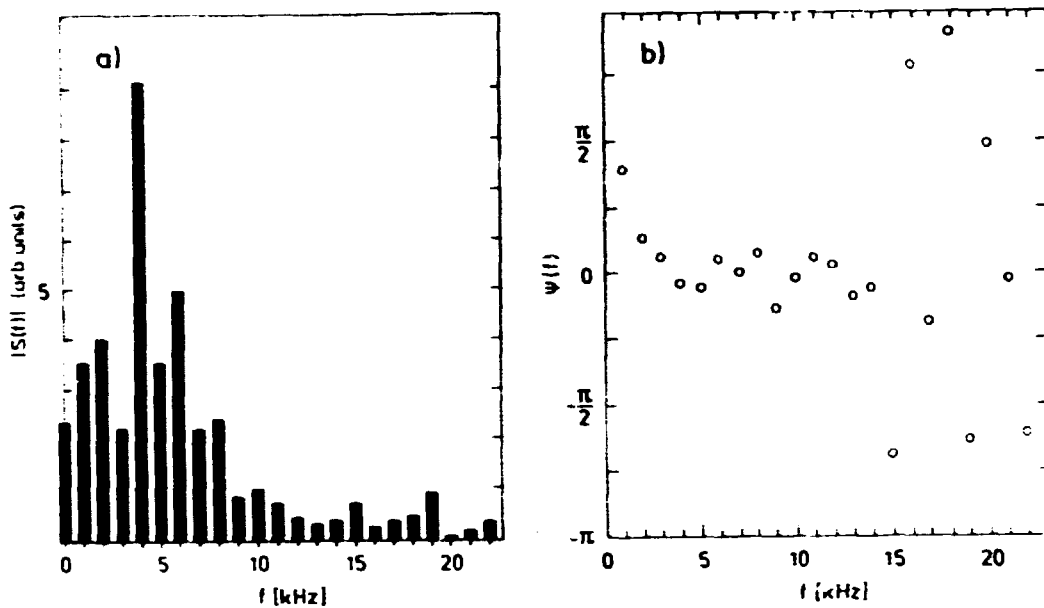


Figure 20. Cross-power spectrum for  $\tilde{n}$  and  $\tilde{E}$ , from a Fourier transform of the results in Fig. 19. a)  $|S(f)|$ , b)  $\Psi(f)$ . For large frequencies where the amplitude is small the phase calculations are not reliable.

In Fig. 21 is shown the autocorrelation functions and the cross correlation between the density and electrical field (similar to Fig. 19). The fluctuation level is somewhat lower than in the broad band case. The correlation between the density and electrical field is in this case very low,  $R_{\tilde{n} \times \tilde{E}}(0)/(R_{\tilde{n}}(0)R_{\tilde{E}}(0)) \simeq 0.03$ . The density and electrical field are approximately  $\pi/2$  out of phase, as is clear from Fig. 21d.

The diffusion coefficient is here estimated to  $D_a = 3 \cdot 10^{-5} \text{m}^2 \text{s}^{-1}$ . This is lower by around two orders of magnitude than the anomalous diffusion in the broad band case. This shows that the anomalous transport is strongly dependent on edge plasma parameters.

#### Modification of the flux by convective cell injection.

It was shown in section 2.4 that the external excitation of a convective cell modified the turbulence in the edge in significant ways. To investigate the influence on the turbulent flux measurements of this were made during injection of convective cells. Thus measurements were made of  $\langle \Gamma_0(t_1) \rangle = \langle \tilde{n}(t_1) \tilde{E}(t_1) \rangle$  where  $t_1$  is the time after the cell injection. One result is shown in Fig. 22. This result was obtained with a broad band spectrum. Just after the injection the flux is enhanced, but afterwards, when the main part of the cell passes the probe, the diffusion diminishes. This behaviour is also present when the spectrum has a single frequency peak, as is shown in Fig. 23 for three different values of  $\theta_D$ . The time of the minimum depends on  $\theta_D$  in a way which indicates that the perturbation of the flux travels around the plasma column with the  $\mathbf{E} \times \mathbf{B}_0 / B_0^2$  velocity. An interesting feature is that the flux may go inwards for a short period after the cell injection. This means that it is possible to change the turbulent flux transiently by external perturbations.

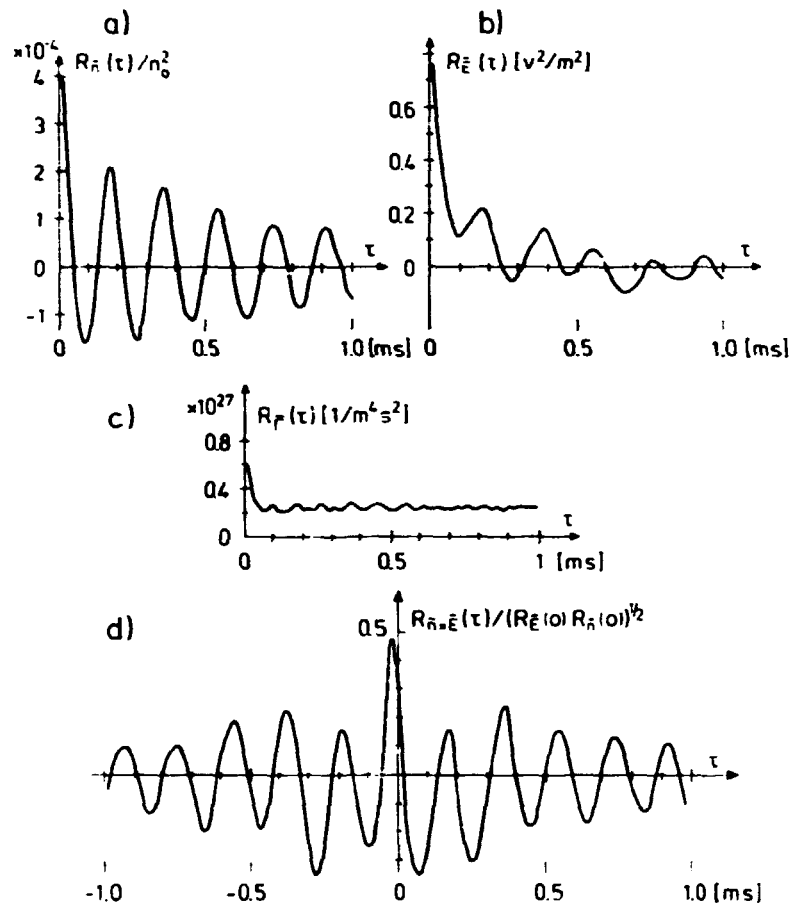


Figure 21. Correlation functions as in Fig. 19 a) Density autocorrelation, b) Electrical field autocorrelation, c) radial flux autocorrelation, d) Cross correlation function  $R_{\vec{n} \times \vec{E}}$ . Plasma parameters:  $B_0 = 0.28 T$ ,  $n_0 = 10^{16} m^{-3}$ .

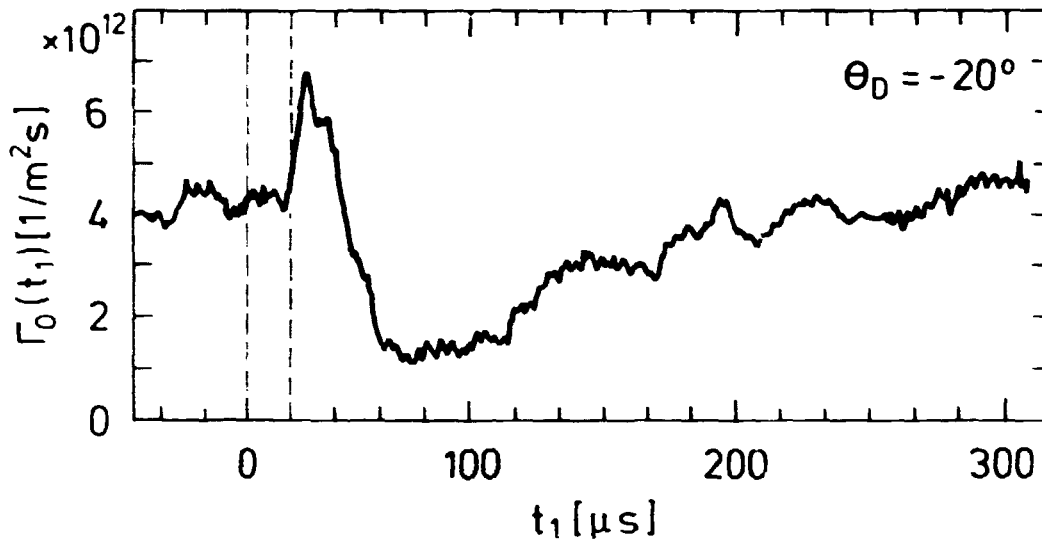


Figure 22. Dynamic response of  $\langle \Gamma_0 \rangle(t_1)$  when a convective cell is injected at  $t_1$ .  $\theta_D$  here denotes the difference in azimuthal position between the probe and the convective cell exciter. The time of the convective cell injection is indicated by the two dashed lines.

However, in these experiments the total flux was not appreciably changed by this method.

## 2.6 Conditional statistical analysis of the turbulence

In the discussion of Fig. 18 it was noted that the probability distribution of the fluctuating radial flux was markedly asymmetric and that it had an anomalously large kurtosis. This seems to indicate that the transport is caused in a large part by large "bursts" of plasma being injected during short intervals of time rather than by a more steady "seeping" of plasma out of the plasma column.

In order to investigate this in more detail a series of experiments have been performed which investigate statistically the conditions in the plasma edge during periods where the plasma transport is anomalously large. Such an investigation has only recently become possible by the availability of fast digital oscilloscopes. A two-channel digital oscilloscope is being used for these measurements in an experimental set-up which closely resembles the one used for the earlier flux measurements. This new set-up consists of the three fixed probes which measure the fluctuating electrical field and density. Added to this is a fourth movable probe which may be placed in any position across the plasma column. This measures the fluctuating potential or density. The potential difference signal from the electrical field probes together with the signal from the moving probe is then fed into the two channels of a digital oscilloscope which in this set-up is used mainly as a transient recorder. It may acquire data scans of up to 32000 points for each channel. The acquisition rate is here put at 50–100kHz which is sufficient to prevent aliasing errors. The acquired traces are then sent to a computer for processing. This processing consists of the following:

- Search the  $E$ -field trace for spikes which fulfill the condition  $\tilde{E} > k \cdot \sigma$ , where  $\sigma$  is the root mean square value of the  $E$ -field trace,  $\sigma = \sqrt{\langle \tilde{E}^2 \rangle}$  and  $k$  is a specified number. (The condition may also be that  $\tilde{E} < k\sigma$  where  $k$  is now a negative number.)

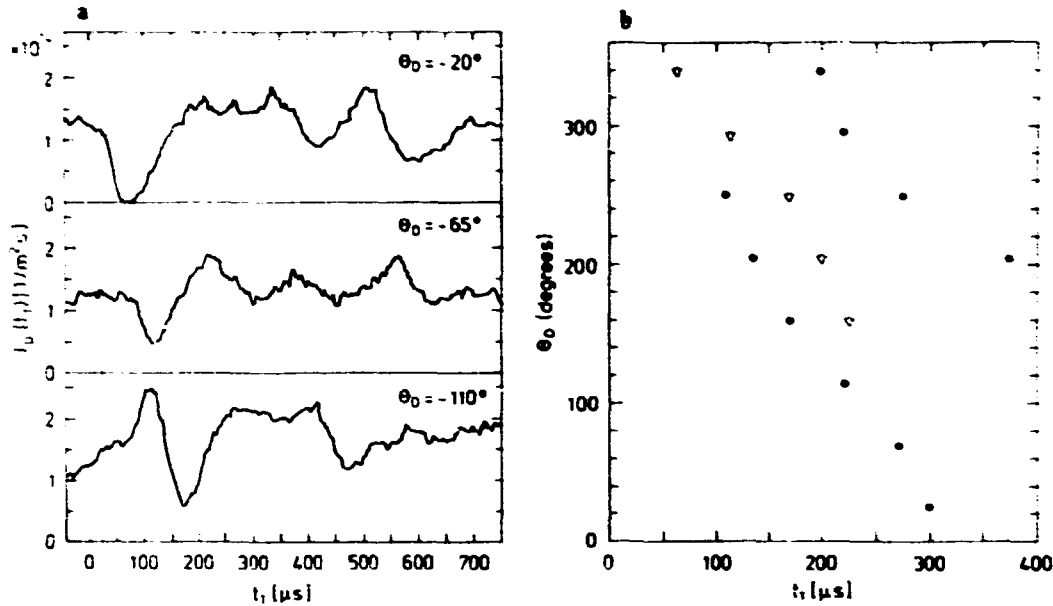


Figure 23. a) Dynamic response of  $(\Gamma_0)(t_1)$  at three different values of  $\theta_D$ .  
 b) Azimuthal position of the two pronounced local maxima  $\bullet$  and the local minimum  $\nabla$  of  $(\Gamma_0)$  as a function of  $t_1$ .

- Every time the condition is fulfilled take out the part of the trace starting a time  $\tau$  before the spike and ending at a time  $\tau$  after the peak. These are then added together. This is done both for the  $E$ -field and for the potential fluctuation trace.
- Repeat the preceding for a number of positions of the potential probe.

By moving the movable probe around and performing this measurement in a grid of points it is possible to obtain an averaged picture of the plasma when the fluctuating electrical field is large (positive or negative) at the position of the fixed probes, or in other words when there is a large instantaneous radial transport of plasma into or out of the plasma column.

An example of a measurement of this kind is shown in Fig. 24. Here the measurement has been made in a grid of  $8 \times 13$  points across half of the plasma column. From the measurements pictures have been reconstructed of the state of the plasma at four times before and after the peak in the electrical field. The plots show an average of a few hundred occurrences.

The figure clearly shows the occurrence of a pair of convective cells of opposite polarity moving past the electrical field probes. At the time  $\tau = 0$  the boundary between the two cells is almost right between the two probes. The polarity of the cells indicates that the instantaneous transport is out of the plasma column. In Fig. 25 is shown a similar measurement where the movable probe measured the fluctuating density. In Fig. 25 the density fluctuations have been normalised by the local DC density. This shows that at the time of a large electrical field the density perturbation at the probe position is clearly negative. This indicates that the fluctuations in the density and electrical field are largely out of phase. Thus the net transport is small and the large structures shown here may be relatively ineffective in transporting the plasma out of the column. This is in agreement with

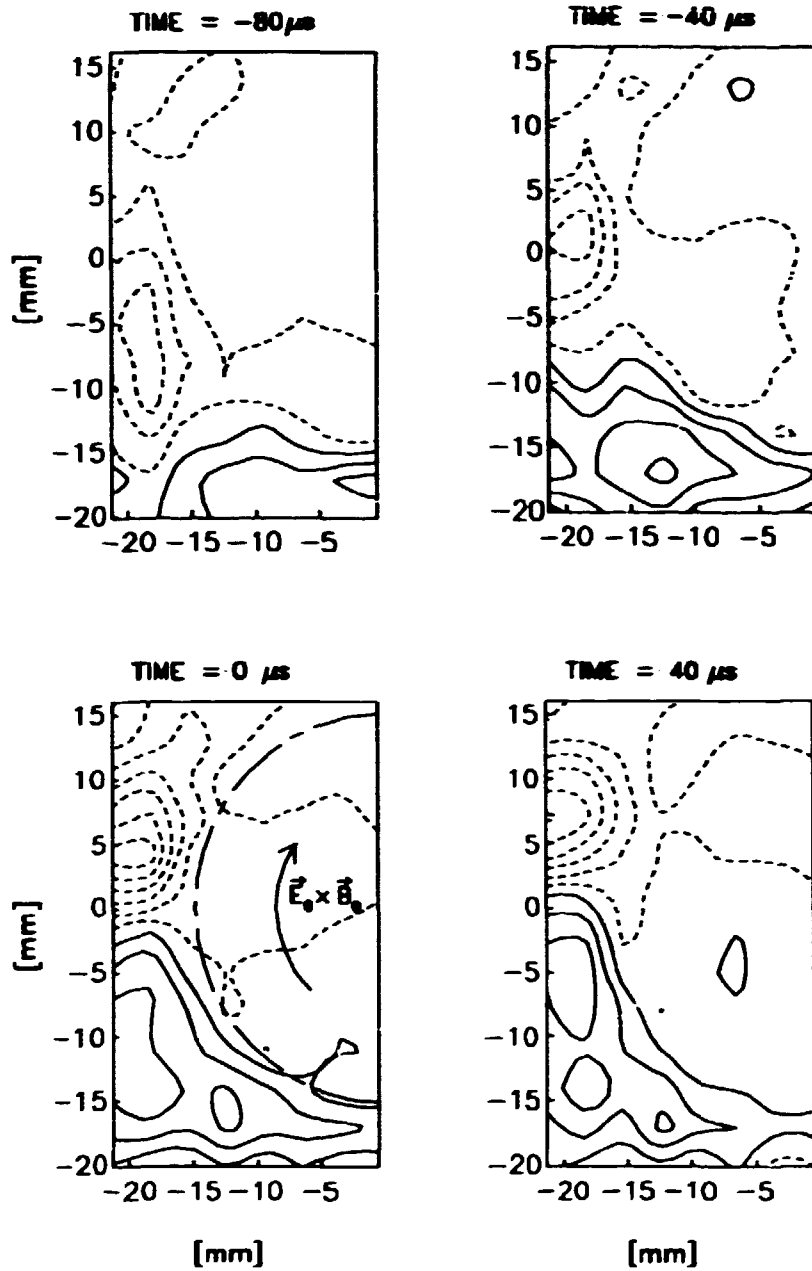


Figure 24. Conditionally averaged potentials for four different times. The electrical field probes were placed in the midplane 10mm apart at  $r \approx 17\text{mm}$ . The condition was  $E_1 > 1.5\sigma$  where  $\sigma$  is the RMS value of the fluctuating electrical field. Negative contours (and the zero contour) are dashed, positive are solid. The direction of the  $\mathbf{E}_0 \times \mathbf{B}_0 / B_0^2$  velocity is indicated by an arrow. The half-circle in the plots indicate the position of the hot plate.  $B_0 = 0.35\text{T}$ ,  $n_0 = 3 \cdot 10^{13}\text{m}^{-3}$ .

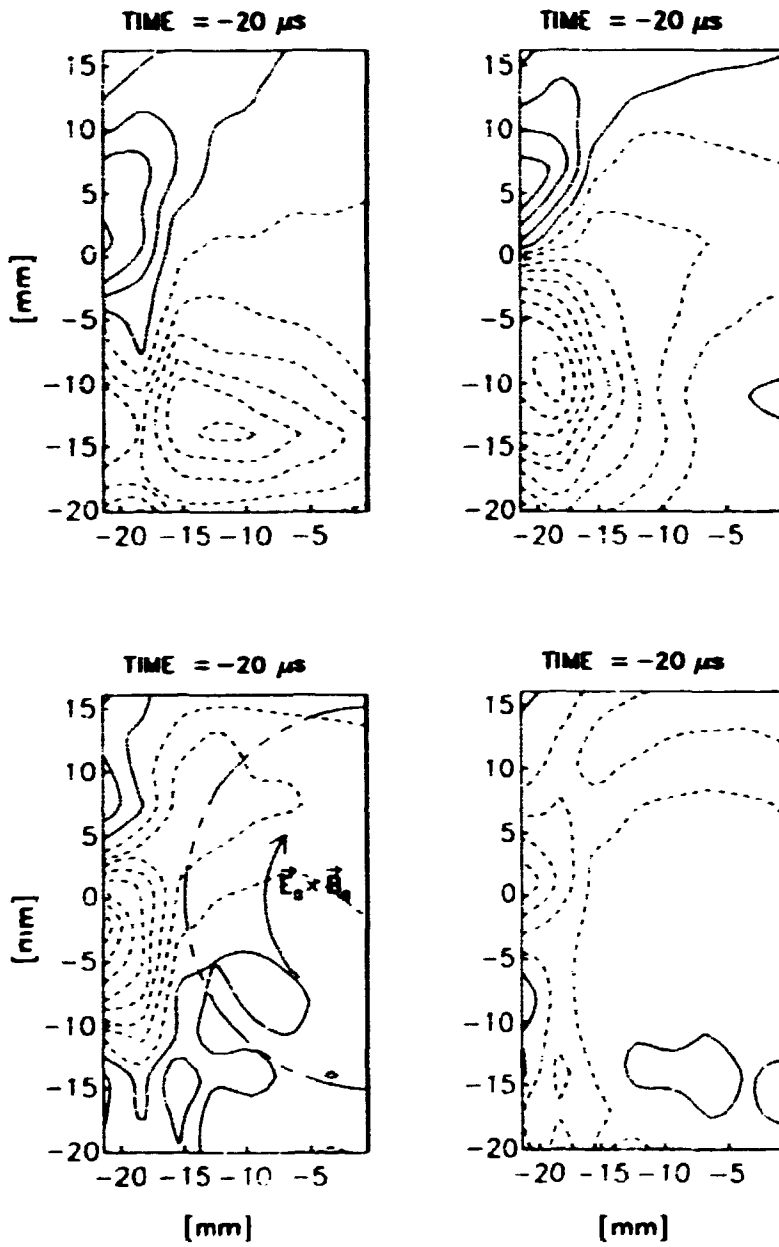


Figure 25. Similar to the previous figure, only here the plot is of the normalised density  $\bar{n}(z)/n_0(z)$ .



the results obtained in the previous section.

In order to avoid storing very large amounts of data the incoming data for Figs. 24–25 are processed at once for each point in the grid. However, this means that it is not possible to make another analysis (e.g. with a different condition) of the same data. For this reason a simpler experiment was performed which allowed us to save the entire trace for a single point. In this way several different conditions can be investigated for the same set of data and the raw data may be manipulated in various ways. The measurement was made with the two fixed  $E$ -field probes and the fixed density probe. Traces of the  $E$ -field and the density fluctuations were obtained. The instantaneous flux due to the fluctuations can then be calculated by multiplying the two signals. Some results are shown in Fig. 26. In this figure is given the conditionally averaged values of the  $E$ -field, the density fluctuations and the flux  $\bar{\Gamma} = \bar{n}\bar{E}$  for two different conditions, one where the  $E$ -field fluctuation is positive and hence the instantaneous transport is outwards and one where the  $E$ -field is negative. In both cases it is clear that the density is perturbed when the electrical field has a large spike. The phase difference between  $E$  and  $n$  lies between 0 and  $\pi/2$  in both the positive and negative case. This causes the somewhat surprising result that the flux has a positive spike both when the transport is outwards and when it is inwards. Even more surprising is the fact that while the flux spike is small when the transport is outwards (in agreement with the experiments described in the previous paragraph) the flux is much larger when the transport is inwards. This means that the greatest contribution to the net flux comes when the instantaneous transport is inwards. There is perhaps a correspondence between this result and the results shown in fig. 18. This shows the probability densities for the various fluctuating quantities. Looking closely at this figure, one may see that both the density and the electric field distributions are slightly skewed in the negative direction, while the flux distribution is clearly skewed in the positive direction. All this indicates that a considerable part of the net flux may be due to these negative  $E$ -field spikes. This is being investigated further at the time of writing.

## 2.7 Plans for the near future

The experiments described above clearly show that large fluctuations do contribute to the net flux out of the plasma column. However, the mechanism is not clear. In particular it is not understood why the greatest (perhaps even dominant) contribution comes when the transport is actually inwards. For this reason there is need of an experiment where potential or density data are acquired from a number of points together with the  $E$ -field data in a way similar to the one described above. However, this time all the data must be saved so that it is possible to apply several different conditions to the same set of data. This requires the storage of large sets of data (typically 10Mbytes) so the experiment must be carefully prepared. It is not practical to store a large number of such experiments.

On a slightly longer timescale it may be possible to perform a similar experiment where the condition is applied to both the electrical field and the flux signal. In this way large flux spikes can be investigated in more detail. However, this will require three or more input channels where at the present only two are available. This may be remedied at some time in the future, the authorities willing.

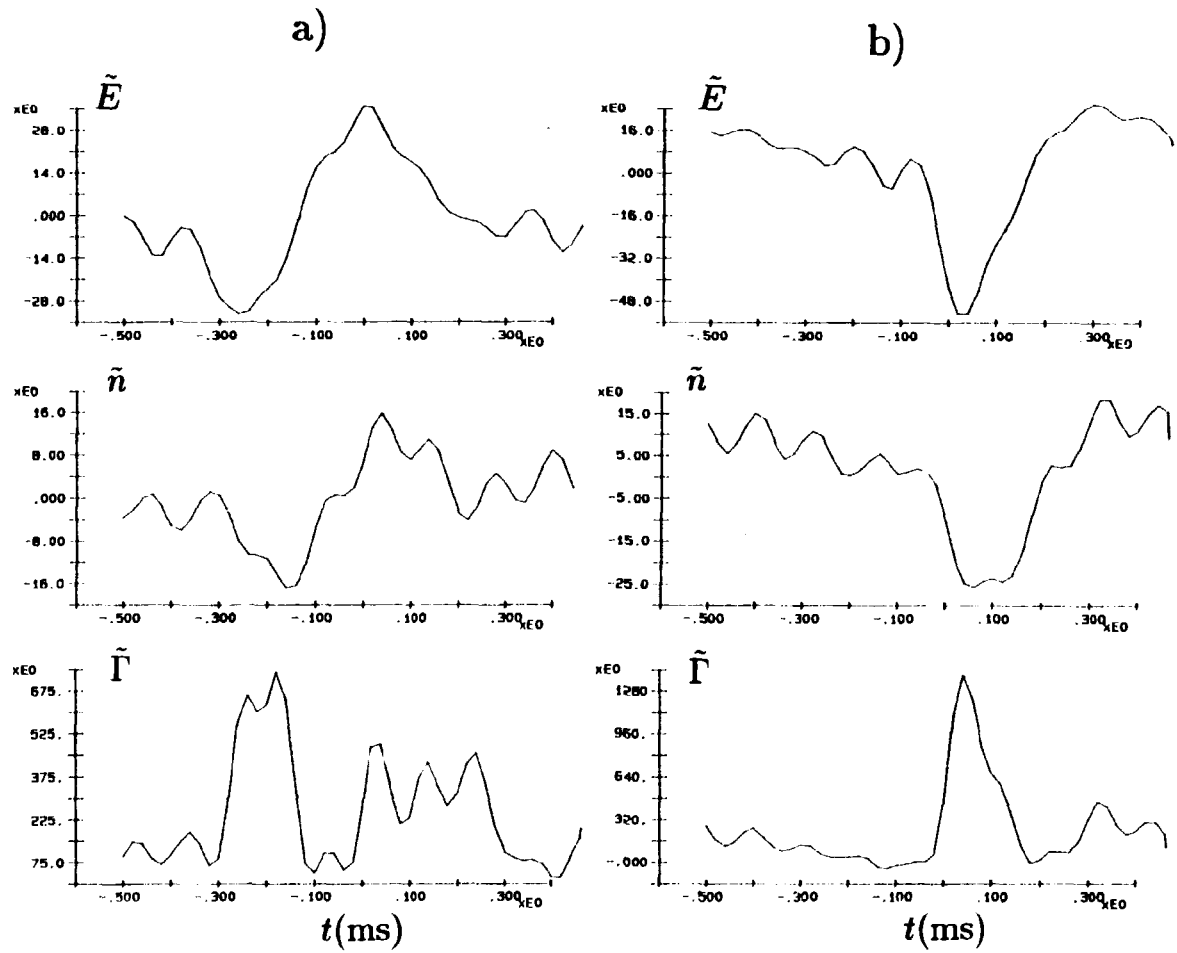


Figure 26. Conditionally averaged values of  $\tilde{E}_0$ ,  $\tilde{n}$  and  $\tilde{\Gamma}$  for two different conditions. a)  $\tilde{E} > 1.5\sigma$ , b)  $\tilde{E} < -1.5\sigma$ , where  $\sigma$  is the root mean square of the fluctuating  $E$ -field.  $B_0 = 0.35 T$ ,  $n_0 = 3 \cdot 10^{15} m^{-3}$ .

### 3 Numerical simulation of Q-machine edge plasma

#### 3.1 Formulation of the problem

Due to the magnetic field the plasma in the Q-machine can be considered essentially two-dimensional. Therefore it may be worthwhile to try to make a numerical simulation of the processes in the plasma and especially in the edge of the plasma which is dominated by large density and electrical field gradients. This chapter describes a method for simulating a disk- or ring-shaped two-dimensional plasma.

The starting point for the simulation is the fluid equations of continuity for the electrons and ions:

$$\frac{\partial n_{i,e}}{\partial t} + \mathbf{v} \cdot \nabla n_{i,e} = 0. \quad (6)$$

Here  $n_{i,e}$  are the ion and electron densities respectively. The velocity  $\mathbf{v}$  should really be calculated from the higher order fluid equations. However, here only the lowest order approximation is taken into account, in which the velocity is the  $\mathbf{E} \times \mathbf{B}$  velocity given by:

$$\mathbf{v} = \frac{\mathbf{E} \times \mathbf{B}}{B^2}. \quad (7)$$

The flow is here taken to be incompressible and inviscid, and it is assumed that higher-order effects can be ignored so that  $\mathbf{v}_i = \mathbf{v}_e$ . If we assume that all ions are singly ionised we can get an equation for the charge density  $\rho = n_i - n_e$  by subtracting the two continuity equations. Using then Poisson's equation and the fact that  $\mathbf{E} = -\nabla\phi$  the following closed system of equations is obtained:

$$\frac{\partial \rho}{\partial t} + \mathbf{v} \cdot \nabla \rho = 0 \quad (8)$$

$$\mathbf{v} = \frac{\mathbf{E} \times \mathbf{B}}{B^2} \quad (9)$$

$$\nabla^2 \phi = -\frac{\rho}{\epsilon_0} \quad (10)$$

where  $\phi$  is the electrical potential. Equation 8 is known in fluid dynamics as *Euler's equation*. These equations, together with appropriate initial and boundary conditions, form the system that is to be solved. Note however, that several assumptions have been made in the process of simplification. As already mentioned incompressibility has been assumed. When we subtracted the mass conservation equations we lost all information about the plasma density and density gradients. This is especially grave for a simulation of the main plasma in the Q-machine since this part of the plasma is characterized by strong density gradients and hardly any electrical fields. This simulation will therefore be restricted to the edge of the Q-machine plasma. Furthermore, all external forces except electrical and magnetic fields have been disregarded. Finally, despite the use of  $\mathbf{E} \times \mathbf{B}$  drift velocities finite Larmor radius effects have been ignored, even for the ions.

The equations to be solved describe an incompressible plasma in a magnetic field. However, a mathematically entirely analogous problem exists in fluid dynamics. If  $\psi$  denotes the stream function,  $\omega = \nabla \times \mathbf{v}$  the vorticity (a pseudo-scalar in this two-dimensional problem,  $\omega = 0, 0, \omega_z$ ) and  $\mathbf{v}$  the velocity we have the following equations for an inviscid incompressible fluid:

$$\frac{\partial \omega}{\partial t} + \mathbf{v} \cdot \nabla \omega = 0 \quad (11)$$

$$\omega = \nabla \times \mathbf{v} \quad (12)$$

$$\nabla^2 \psi = \omega \quad (13)$$

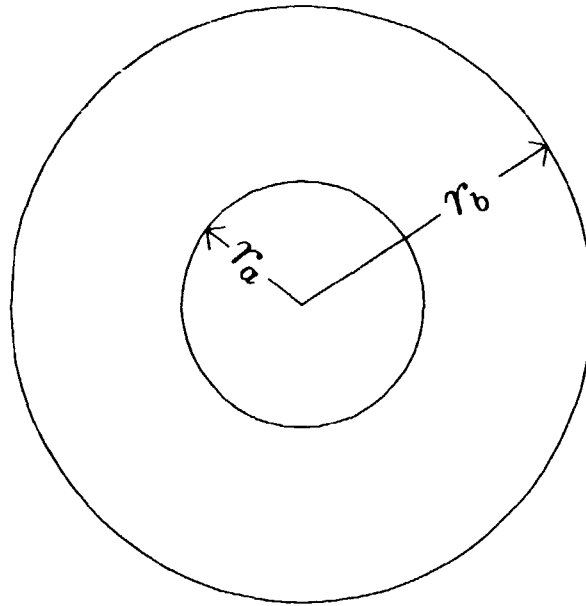


Figure 27. The shape of the region in which the equations are to be solved.

where the sign convention is taken from [13]. It is easy to see that apart from a sign in Poisson's equation these equations are analogous to Eqs. 8-10.

The equations are solved in an annulus-shaped region as shown in Fig. 27.  $r_a$  is the inner and  $r_b$  is the outer radius of the annulus. The shape of the region makes cylindrical (polar) coordinates an obvious choice. In cylindrical coordinates equations 8 and 10 look like this where  $r$  is the radial and  $\theta$  the azimuthal coordinates:

$$r \frac{\partial \rho}{\partial t} + \frac{1}{B_z} \left[ \frac{\partial \phi}{\partial \theta} \frac{\partial \rho}{\partial r} - \frac{\partial \phi}{\partial r} \frac{\partial \rho}{\partial \theta} \right] = 0, \quad (14)$$

$$r^2 \frac{\partial^2 \phi}{\partial r^2} + r \frac{\partial \phi}{\partial r} + \frac{\partial^2 \phi}{\partial \theta^2} = -r^2 \frac{\rho}{\epsilon_0}. \quad (15)$$

Eq. 10 has been multiplied by  $r^2$  in the process. On the two boundaries the potentials are constant around the annulus though not necessarily equal. This means that we have  $E_\theta = 0$  at both boundaries and since  $v_r = -E_\theta/B_z = 0$  there can be no transport across the boundaries.

## 3.2 The Numerical Methods

### General method

Equations 14 and 15 can be combined to form one nonlinear partial differential equation with derivatives in both space and time. This is a mixed initial-boundary value problem. The boundary conditions for this equation are:  $\phi(r_a, \theta, t) = V_a$ ,  $\phi(r_b, \theta, t) = V_b$ ,  $\phi(r, 0, t) = \phi(r, 2\pi, t)$ . The initial condition is  $\phi(r, \theta, 0) = f(r, \theta)$ . The method used here for solving it uses a finite difference (time-differencing) method for the time variable [14, 15], since this is unbounded. For the space variables we use one of the so-called pseudospectral methods [16, 17]. These methods work by sampling the functions of the equations at discrete points (collocation points) and then expanding these data in a series of orthogonal functions. The system of equations can then be solved by working on the coefficients of these

functions to give a solution for each time step. The trick lies in selecting expansion functions that are well-behaved. The most commonly used expansion is the Fourier expansion because it has nice properties with respect to differentiation [18]. But Fourier expansion is only possible if the problem has cyclical boundary conditions. In the present problem this is only the case in the azimuthal direction, where we use a real (not complex) Fourier expansion.

However, one may use many other sets of linearly independent functions. For this problem the variables are expanded in the radial direction in Chebyshev polynomials of the first kind. (In the following they will simply be called Chebyshev polynomials). The generating function for the  $n$ 'th Chebyshev polynomial is:

$$T_n(x) = \cos(n \arccos x), \quad (16)$$

and the first few polynomials are:

$$\begin{aligned} T_0(x) &= 1 \\ T_1(x) &= x \\ T_2(x) &= 2x^2 - 1 \\ T_3(x) &= 4x^3 - 3x \\ &\vdots \end{aligned}$$

As can be seen from the generating function Chebyshev polynomials are only defined in the interval  $-1 \leq x \leq 1$ . At the edges of this interval we have for all  $n$ :

$$T_n(-1) = (-1)^n \quad (17)$$

$$T_n(1) = 1. \quad (18)$$

This means that the annulus must have a width  $r_b - r_a = 2$ , and the radial distance must be transformed like this:

$$x = r - a$$

where  $a$  is the mean radius of the annulus  $a = (r_a + r_b)/2$  (see Fig. 27). The expansion of the functions will thus be of the form:

$$F(x, \theta) = \sum_{n=-\infty}^{\infty} \left( \sum_{m=0}^{\infty} a_{mn} T_m(x) \right) e^{in\theta} \quad (19)$$

with  $0 \leq \theta \leq 2\pi$ ,  $-1 \leq x \leq 1$ .

The function is expanded in infinite series of orthogonal functions, something that is fairly impossible to do on a computer. An explanation on how to truncate to a finite number of expansion functions (modes) is given in section 3.2. In the azimuthal direction we have periodic boundaries and so we can perform a Fourier expansion in this direction. Numerical methods for Fourier expansion (transformation) are well known [19]. However, there is no method which will directly expand a function given at discrete points in Chebyshev polynomials. To remedy this the grid points in the radial direction have been chosen in the following way:

$$x_i = -\cos\left(\frac{\pi i}{M}\right), \quad 0 \leq i \leq M. \quad (20)$$

With this choice of points Eq. 16 will look like this:

$$T_n(x_i) = \cos\left(n \arccos\left[-\cos\left(\frac{\pi i}{M}\right)\right]\right) = -\cos\left(\frac{n\pi i}{M}\right). \quad (21)$$

The Chebyshev polynomials are now expressed by a cosine function and so the Chebyshev expansion can be performed by a cosine transform which is closely related to a Fourier transform.

### Fourier expansion methods

The general method for expanding a periodic function in a Fourier series is found in standard mathematical textbooks and looks like this:

$$f(x) = \sum_{n=-\infty}^{\infty} c_n e^{inx} \quad (22)$$

where the complex numbers  $c_n$  are given by

$$c_n = \frac{1}{2\pi} \int_{-\pi}^{\pi} f(x) e^{-inx} dx. \quad (23)$$

$f(x)$  is periodic with period length  $2\pi$ .

This method demands the calculation of an infinite number of factors  $c_n$ , so it is not very well suited for numerical treatment. However, there are several ways of making approximations to this system. One is to simply truncate the sum:

$$f(x) \simeq \sum_0^N c_n e^{inx}. \quad (24)$$

This method is called the Galerkin or true spectral method. Note that  $f(x)$  is still continuous. The method we have chosen is a little different. Instead of approximating the function at all points we choose a number of equidistant discrete points,  $f(x_j)$  and demand that the expansion be exact at these points. This is the so-called pseudospectral or collocation method. (The use of these names in the literature is not consistent.) The points  $x_j$  are called collocation points. The expansion now looks like this:

$$f(x_j) = \sum_{k=0}^{N-1} c_k e^{ijx_k} = \sum_{k=0}^{N-1} c_k e^{i \frac{2\pi}{N} jk} \quad (25)$$

with the  $c_k$ 's given by:

$$c_k = \frac{1}{N} \sum_{j=0}^{N-1} f(x_j) e^{-i \frac{2\pi}{N} kj}. \quad (26)$$

A proof that these two equations are consistent with each other is given in App. B.

In the present case  $f(x)$  is a real function but the  $c_k$ 's are complex. Thus twice as much space is needed to store the function values in "transformed space" (i.e. expanded) as in "real space" but of course there is no more information stored. This amounts to a considerable waste of computer memory. For this reason a real (not complex) Fourier expansion (transform) has been chosen. Here the expansion is in sines and cosines:

$$f(x_j) = \frac{1}{2} a_0 + \frac{1}{2} a_{N/2} \cos(\pi j) + \sum_{k=1}^{N/2-1} \left( a_k \cos\left(\frac{2\pi}{N} jk\right) + b_k \sin\left(\frac{2\pi}{N} jk\right) \right) \quad (27)$$

where the coefficients  $a_k$  and  $b_k$  are given by:

$$\begin{aligned} a_k &= \frac{2}{N} \sum_{j=0}^{N-1} f(x_j) \cos\left(\frac{2\pi}{N} kj\right), \\ b_k &= \frac{2}{N} \sum_{j=0}^{N-1} f(x_j) \sin\left(\frac{2\pi}{N} kj\right). \end{aligned} \quad (28)$$

The proof of consistency for these equations is very similar to the complex transform case.

The real Fourier transform lends itself well to the transformation of data in the azimuthal direction. However, it was found in Eq. 21 that Chebyshev polynomials

can be represented as cosine functions. Therefore the data must be transformed in the radial direction into an expansion in cosines. This is done in a way very similar to the real Fourier transform:

$$f(x_j) = \sum_{k=0}^N a_k \cos\left(\frac{\pi}{N}jk\right) \quad (29)$$

with the  $a_k$ 's given by:

$$a_k = \frac{1}{2N} \sum_{j=0}^N f(x_j) \cos\left(\frac{\pi}{N}kj\right). \quad (30)$$

Note that here we expand in  $N + 1$  functions and that the transformation and the inverse transformation are symmetrical<sup>2</sup>.

### Solving Poisson's equation

Poisson's equation in cylindrical equations is given in Eq. 15. After transformation this equation gives an equation for the infinite series given in Eq. 19 which looks like this for each  $n$ :

$$\begin{aligned} (x+a)^2 \frac{d^2}{dx^2} \left( \sum_{m=0}^{\infty} \phi_{mn} T_m(x) \right) + (x+a) \frac{d}{dx} \left( \sum_{m=0}^{\infty} \phi_{mn} T_m(x) \right) - n^2 \sum_{m=0}^{\infty} \phi_{mn} T_m(x) \\ = -(x+a)^2 \sum_{m=0}^{\infty} \rho_{mn} T_m(x) \end{aligned} \quad (31)$$

where  $\rho$  has been used for  $\rho/\epsilon_0$ . (This will be done from now on.) This equation contains the first and second derivatives of series of Chebyshev polynomials multiplied by powers of  $x$ . The polynomials ensuing from differentiation of Chebyshev polynomials and multiplications with polynomials are not themselves Chebyshev polynomials and so cannot be used directly for this calculation. But formulas are available for calculating the derivatives of functions that are expressed as Chebyshev series. A function  $f(x)$  which is expanded:

$$f(x) = \sum_{m=0}^{\infty} a_m T_m(x)$$

can be expressed as a new series of Chebyshev polynomials. Formulas are given in Appendix A which will be useful for this purpose.

<sup>2</sup>In the otherwise excellent treatment of the Fast Fourier Transform in Numerical Recipes[19] the authors mistakenly assert that the cosine transform is not symmetrical and devote much discussion to the problem of how to make it so.

Using the relations in Appendix A, Eq. 31 can be written:

$$\begin{aligned}
& \left( (x+a)^2 \frac{d^2}{dx^2} + (x+a) \frac{d}{dx} - n^2 \right) \sum_{m=0}^{\infty} \phi_{mn} T_m(x) \\
&= \left( \frac{1}{2} \sum_{\substack{p=2, \\ p \text{ even}}}^{\infty} p(p^2-2)\phi_{pn} + a \sum_{\substack{p=3, \\ p \text{ odd}}}^{\infty} p(p^2-1)\phi_{pn} + \frac{1}{2}a^2 \sum_{\substack{p=2, \\ p \text{ even}}}^{\infty} p^3\phi_{pn} + \sum_{\substack{p=2, \\ p \text{ even}}}^{\infty} p\phi_{pn} \right. \\
&+ a \sum_{\substack{p=1, \\ p \text{ odd}}}^{\infty} p\phi_{pn} - n^2\phi_{0n} \left. + \sum_{m=1}^{\infty} (m(m-1)\phi_{mn} + \sum_{\substack{p=m+2, \\ p+m \text{ even}}}^{\infty} p(p^2-m^2-2)\phi_{pn} \right. \\
&+ 4am(m+1)\phi_{m+1,n} + 2a \sum_{\substack{p=m+3, \\ p+m \text{ odd}}}^{\infty} p(p^2-m^2-1)\phi_{pn} + a^2 \sum_{\substack{p=m+2, \\ p+m \text{ even}}}^{\infty} p(p^2-m^2)\phi_{pn} \\
&+ m\phi_{mn} + 2 \sum_{\substack{p=m+2, \\ p+m \text{ even}}}^{\infty} p\phi_{pn} + 2a \sum_{\substack{p=m+1, \\ p+m \text{ odd}}}^{\infty} p\phi_{pn} - n^2\phi_{mn} \left. \right) T_m(x) \\
&= -(x+a)^2 \sum_{m=0}^{\infty} \rho_{mn} T_m(x). \tag{32}
\end{aligned}$$

Several of these terms cancel and the end result is:

$$\begin{aligned}
& \left( \frac{1}{2}(a^2+1) \sum_{\substack{p=2, \\ p \text{ even}}}^{\infty} p^3\phi_{pn} + a \sum_{\substack{p=1, \\ p \text{ odd}}}^{\infty} p^3\phi_{pn} - n^2\phi_{0n} \right) + \sum_{m=1}^{\infty} \left( (a^2+1) \sum_{\substack{p=m+2, \\ p+m \text{ even}}}^{\infty} p(p^2-m^2)\phi_{pn} \right. \\
&+ 2a \sum_{\substack{p=m+1, \\ p+m \text{ odd}}}^{\infty} p(p^2-m^2)\phi_{pn} + (m^2-n^2)\phi_{mn} \left. \right) T_m(x) \\
&= -(x+a)^2 \sum_{m=0}^{\infty} \rho_{mn} T_m(x) \\
&= - \sum_{m=0}^{\infty} \rho_{mn}^* T_m(x). \tag{33}
\end{aligned}$$

In this system truncation to a finite number of modes is done by choosing a number of collocation points as explained in section 3.2. Then the upper boundary on the sums can be replaced by the number of modes  $M$  which we want to retain. (Note that the expansion coefficients,  $\phi_{mn}$ , for the retained terms are not exactly identical to the coefficients of the same modes in the full expansion.) We thus get for each Fourier mode a set of  $M+1$  linear equations with the  $M+1$  unknowns  $\phi_{0n}, \phi_{1n}, \dots, \phi_{Mn}$ . The  $m$ 'th equation has the following form:

$$\begin{aligned}
& (m^2 - n^2)\phi_{mn} + 2a(m+1)(2m+1)\phi_{m+1,n} + (1+a^2)(m+2)(4m+4)\phi_{m+2,n} + \dots \\
& + a^*(M)(M^2 - m^2)\phi_{Mn} = -\rho_{mn}
\end{aligned}$$

with  $a^*$  either equal to  $2a$  or  $1+a^2$  depending on whether  $m$  is odd or even. The structure of the system of equations is shown in Fig. 28. This system is triangular, (it is also singular, as there is a zero in the diagonal where  $m^2 = n^2$ , more about that later). Solving a triangular system by back-substitution requires a few times  $M^2$  floating point operations. So to solve for  $\phi$  requires of the order of  $N \cdot M^2$  operations. If we want to solve the equations using a large number of modes we can run into trouble, even on a large computer. Luckily, there is a way around this. If we denote the  $m$ 'th equation  $E(m)$  we can make the operation





$E^*(m) = E(m) + \alpha E(m+2) + \beta E(m+4)$ . By choosing  $\alpha$  and  $\beta$  correctly we can eliminate all terms except for the first five in all the equations. If you look at Eq. 33 and Fig. 28 you will see that the  $p$ 'th and  $p+1$ 'th columns of the triangular matrix will look like this ( $p$  is odd in this example):

$$\begin{bmatrix} \alpha p^3 & \frac{1}{2}(1+\alpha^2)(p+1)^3 \\ (1+\alpha^2)p(p^2-1) & 2\alpha(p+1)((p+1)^2-1) \\ 2\alpha p(p^2-4) & (1+\alpha^2)(p+1)((p+1)^2-4) \\ \vdots & \vdots \\ (1+\alpha^2)p(p^2-m^2) & 2\alpha(p+1)((p+1)^2-m^2) \\ 2\alpha p(p^2-(m+1)^2) & (1+\alpha^2)(p+1)((p+1)^2-(m+2)^2) \\ (1+\alpha^2)p(p^2-(m+2)^2) & 2\alpha(p+1)((p+1)^2-(m+2)^2) \\ 2\alpha p(p^2-(m+3)^2) & (1+\alpha^2)(p+1)((p+1)^2-(m+3)^2) \\ \vdots & \vdots \end{bmatrix}$$

From this it is fairly easy to see that we can write two equations for  $\alpha$  and  $\beta$ :

$$p(p^2-m^2) + \alpha p(p^2-(m+2)^2) + \beta p(p^2-(m+4)^2) = 0,$$

$$((p+1)^2-m^2) + \alpha((p+1)^2-(m+2)^2) + \beta((p+1)^2-(m+4)^2) = 0.$$

These equations must hold for all values of  $m$  and  $p$ , so we can solve for  $\alpha$  and  $\beta$ .

The result is:

$$\alpha = \frac{-2(m+2)}{m+3}, \quad (34)$$

$$\beta = \frac{m+1}{m+3}. \quad (35)$$

So we end up with a set of equations of the following form:

$$\begin{aligned} & (m^2-n^2)\phi_{mn} + 2\alpha(m+1)(2m+1)\phi_{m+1,n} + (4(1+\alpha^2)((m+2)(m+1) \\ & - \alpha((m+2)^2-n^2))\phi_{m+2,n} + 2\alpha(2m^2+9m+7)\phi_{m+3,n} + \beta((m+4)^2-n^2)\phi_{m+4,n} \\ & = -\rho_{mn} - \alpha\rho_{m+2,n} - \beta\rho_{m+4,n}. \end{aligned} \quad (36)$$

For  $m=0$  and for the last few equations this will look a little different.

Now we have a triangularised, pentadiagonal system of equations. This can be solved using  $O(M)$  operations. But the system is still singular and we have not taken account of boundary conditions. Both can be resolved by noting that at the boundaries we get:

$$\sum_{m=0}^M (-1)^m \phi_{mn} = a_n, \quad (37)$$

$$\sum_{m=0}^M \phi_{mn} = b_n. \quad (38)$$

If the last two equations in the system are replaced with these two, a regular system of equations is obtained. The last two equations in the system are the ones which should be removed since they only contain information about the highest modes and are not very accurate because of the truncation. One obstacle remains. If you look at Eq. 36 you will see that for  $m \geq n$  the coefficients of the second and third term is larger than that of the first term which is the diagonal element. This means that the matrix is ill-conditioned (the diagonal element should be the largest numerically) which will impair the accuracy of the solution, especially when a large number of modes is used. In fact, it was found that already for  $M > 32$  the

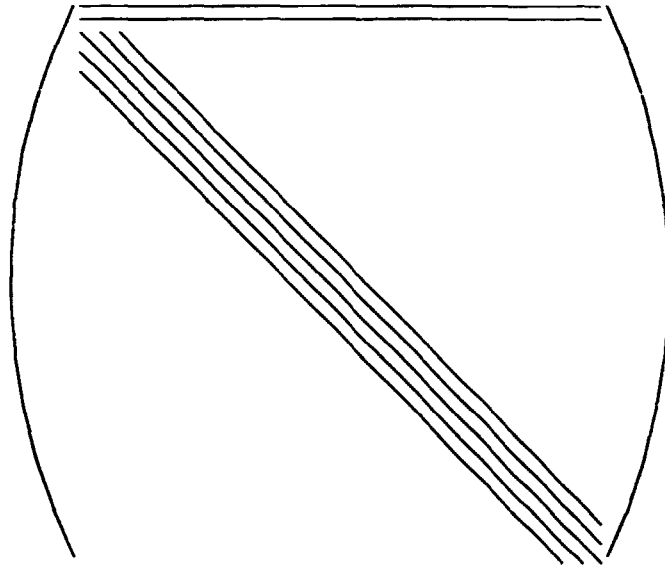


Figure 29. The structure of the matrix after manipulations and insertion of the boundary conditions.

accuracy became unacceptably low. This problem can be solved by putting the two boundary conditions on top of the array and pushing all the other equations down two places. The resulting array has the form outlined in Fig. 29. Now the third term of Eq. 36 is the diagonal element and the matrix is well-conditioned.

This system which can easily be triangularised and solved by back- or forward-substitution. The number of floating operations used to solve this system is  $O(M)$  operations for each azimuthal mode or  $O(M \times N)$  operations for the solution to Poisson's equation. This is less than the amount of computation needed for the Fourier transform which needs  $O(M \log_2(M) \times N + N \log_2(N) \times M)$  operations. This means that it will be feasible to use a large number of modes, eg.  $128 \times 512$ .

#### Calculating the derivatives and other things

As can be seen from Eqs. 8-10 the gradients of both  $\rho$  and  $\phi$  must be calculated. In cylindrical coordinates the gradient operator is:

$$\nabla \rho = \begin{pmatrix} \frac{\partial \rho}{\partial r} \\ \frac{1}{r} \frac{\partial \rho}{\partial \theta} \end{pmatrix} \quad (39)$$

In transformed space the  $\theta$  derivative is calculated very easily, since it is just a differentiation of a Fourier series, i.e. each mode must be multiplied by the mode number:

$$\frac{\partial}{\partial \theta} \left( \sum_{n=0}^N \rho_{mn} e^{-2\pi i n / N} \right) = \frac{-2\pi i}{N} \sum_{n=0}^N n \rho_{mn} e^{-2\pi i n / N}. \quad (40)$$

The calculation of the  $r$  derivative is a bit more tricky since it involves derivatives of series of Chebyshev polynomials. But we can use Eqs. 92 and 93 of Appendix A.

Thus we get:

$$r \frac{\partial \rho}{\partial r} = \alpha \sum_{\substack{p=1, \\ p \text{ odd}}}^M p \rho_{pn} + \sum_{\substack{p=2, \\ p \text{ even}}}^M p \rho_{pn}$$

$$+ \sum_{m=1}^M \left( m\rho_{mn} + 2a \sum_{\substack{p=m+1, \\ p+m \text{ odd}}}^M p\rho_{pn} + 2 \sum_{\substack{p=m+2, \\ p+m \text{ even}}}^M p\rho_{pn} \right). \quad (41)$$

The new coefficients are the sums of the old ones and the amount of calculation needed for taking the gradient seems to be around  $N \times M^2$  multiplications. Again, a simple trick saves the day. Denoting the new coefficients for the derivatives  $\rho'_{mn}$  we get:

$$\begin{aligned} \rho'_{m-2,n} &= (m-2)\rho_{m-2,n} + 2a(m-1)\rho_{m-1,n} + 2m\rho_{mn} + 2a \sum_{\substack{p=m+1, \\ p+m \text{ odd}}}^M p\rho_{pn} \\ + 2 \sum_{\substack{p=m+2, \\ p+m \text{ even}}}^M p\rho_{pn} &= (m-2)\rho_{m-2,n} + 2a(m-1)\rho_{m-1,n} + m\rho_{mn} + \rho'_{mn}. \end{aligned} \quad (42)$$

Now we can calculate the gradients using only a few times  $N \times M$  multiplications and this calculation is not a limiting factor.

In solving Poisson's equation the right-hand side is  $r^2\rho$ , but in most of the rest of the calculations we need just  $\rho$ . Therefore we need a way to multiply and divide by  $r^2$  in transformed space. To this end we can use Eqs. 90 and 91. It is easy to see that if we want to calculate  $r^2\rho$  from  $\rho$  we can get each new coefficient as a sum of a few of the old ones. But if we want to go the other way we have to solve a linear system of equations, each of which looks like:

$$\frac{1}{4}\rho_{m,n-2} + a\rho_{m-1,n} + \left(\frac{1}{2} + a^2\right)\rho_{mn} + a\rho_{m+1,n} + \frac{1}{4}\rho_{m+2,n} = \rho'_{mn}. \quad (43)$$

(Again, the first few equations look a little different.) This system is a pentadiagonal system of equations and can be solved in  $O(M)$  operations for each Fourier mode.

#### Calculation of $\frac{\partial \rho}{\partial t}$ and time integration schemes

In the previous section we saw how to solve Poisson's equation. Now we can plug the solution into the Euler equation and look for ways to solve that. The equation to be solved is given by Eq. 14:

$$r^2 \frac{\partial \rho}{\partial t} = r \left( -\frac{\partial \phi}{\partial r} \frac{\partial \rho}{\partial \theta} + \frac{\partial \phi}{\partial \theta} \frac{\partial \rho}{\partial r} \right). \quad (44)$$

It can be solved in configuration space, transforming the terms necessary for the calculation back into real space before calculating the time derivative. It is easily seen that four terms are needed for this, and each must be back-transformed. After a new value for  $\rho$  has been obtained we must once again transform this into transformed space. So altogether 5 transformations are needed for each time step. It turns out that these transformations take around 70% of the total computation time of the code. It would seem that it was far easier to do the time-stepping in transformed space. This would be possible but would not be any easier for the following reason. On the right-hand side of Eq. 44 we have to calculate two products of terms. This is easily done in real space but in transformed space products become convolution integrals (integrals in the Fourier transform, double sums in the Fourier expansion):

$$F(f(x) \cdot g(x)) = \int F(f(x))F(g(x + \xi))d\xi.$$

Therefore these multiplications must be done in real space and so it makes no difference at this stage whether the timestepping is done in real or in transformed space.

Now that we have calculated the right-hand-side of Eq. 44 we can employ a finite-difference method to solve for  $\rho$ . Several methods exist which are described in literature. In the following I will use the notation used by Gazdag[15]. If we have an equation of this form:

$$\frac{\partial \rho}{\partial t} = G(\rho, r, \theta, t),$$

we can approximate the solution at the time points  $m\Delta t$ . The simplest way is a straightforward extrapolation:

$$\rho^{m+1} = \rho^m + G^m \cdot \Delta t \quad (45)$$

where  $G^m = G(\rho^m, r, \theta, m\Delta t)$ . This method is known as the "Euler" method. It is very easy to use but unfortunately it is unconditionally unstable, i.e. the solution diverges exponentially from the correct solution. Another way is the so-called "leapfrog" method:

$$\rho^{m+1} = \rho^{m-1} + G^m \cdot 2\Delta t. \quad (46)$$

This method too is very simple but is also prone to become unstable. A slightly more involved method is the *partially corrected second-order Adams-Bashforth Scheme* which consists of two steps, a predictor step:

$$\tilde{\rho}^{m+1} = \rho^m + (3\tilde{G}^m - \tilde{G}^{m-1}) \cdot \frac{\Delta t}{2}, \quad (47)$$

and a corrector step:

$$\rho^{m+1} = \rho^m + (\tilde{G}^m + \tilde{G}^{m+1}) \cdot \frac{\Delta t}{2}. \quad (48)$$

Here we first calculate a value of  $\rho$  from the old derivatives  $\tilde{G}^{m-1}$  and  $\tilde{G}^m$ . Then we calculate a new value of the derivative,  $\tilde{G}^{m+1}$  and use this to calculate a corrected value for  $\rho^{m+1}$ . Note that we do not calculate new values for the derivatives but use the ones obtained from the predicted values of  $\rho$  (thus the tildes on these terms). This is why it is called "partially corrected". If the derivative  $G^{m+1}$  is updated with the corrected value of  $\rho$  the scheme is called "fully corrected".

Methods like the 2nd order Adams-Bashforth require more computer memory than the leapfrog and similar schemes because it is necessary to save the derivative for two time steps.

A third method and the one that was chosen initially for this problem is the *third order partially corrected Adams-Bashforth Scheme*. It works much like the second order version. The two steps look like this:

$$\tilde{\rho}^{m+1} = \rho^m + [23\tilde{G}^m - 16\tilde{G}^{m-1} + 5\tilde{G}^{m-2}] \frac{\Delta t}{12}, \quad (49)$$

$$\rho^{m+1} = \rho^m + [5\tilde{G}^{m+1} + 8\tilde{G}^m - \tilde{G}^{m-1}] \frac{\Delta t}{12}. \quad (50)$$

This method has good stability characteristics. On the other hand it requires the saving of three versions of the derivative at all times. Also we need to know the derivative at two previous time points. This means that we can not just start with the initial condition and use the third order Adams-Bashforth scheme. To get the code "up and running" the following starting procedure is used:

1. Take a step to  $\Delta t/2$  with the Euler method.
2. Take a step to  $\Delta t$  with the leapfrog method.
3. Go out to  $2\Delta t$  with the 2nd order Adams-Bashforth.
4. For all following time steps use the 3rd order Adams-Bashforth.

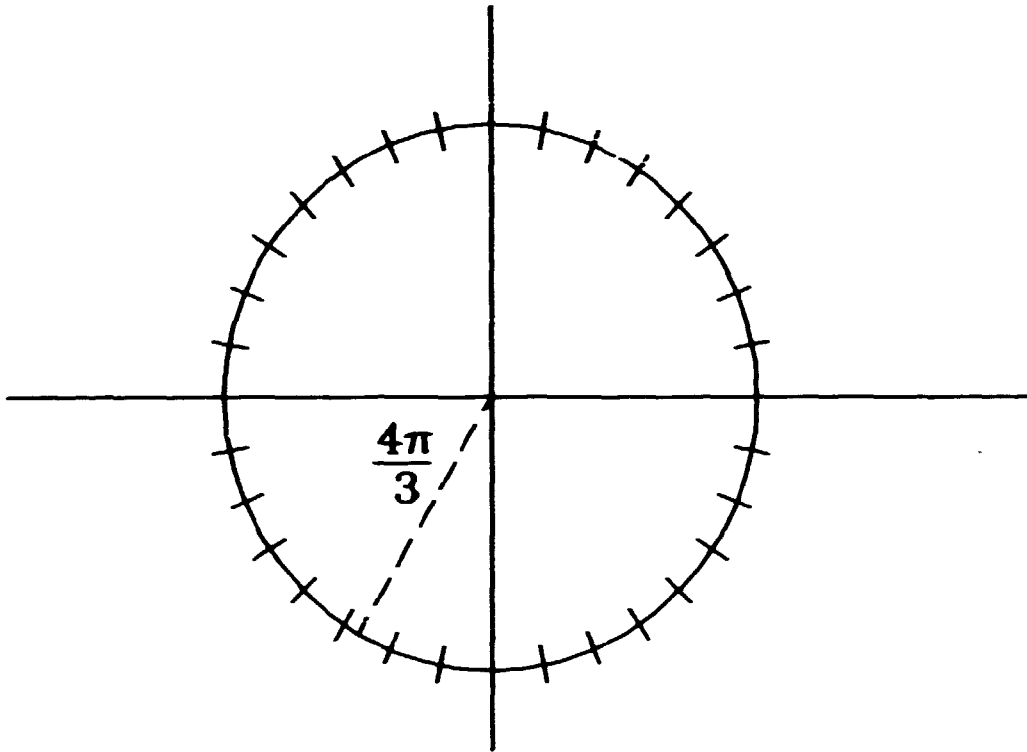


Figure 30. The  $N$  arguments for the sine and cosine expansions in the azimuthal direction,  $2\pi j/N$ , can be represented as angles in a unit circle. Here  $N = 32$ . The dashed line indicates the start of the "forbidden" area where aliasing occurs.

#### Dealiasing

In the previous section it was seen that it is necessary to do a couple of multiplications of terms in order to solve the system of equations. But in doing these multiplications we encounter a new difficulty. When two Fourier expansions of functions are multiplied we effectively multiply all modes with each other. In other words we get terms of the form

$$a_j a_k \cos\left(\frac{2\pi j}{N}\right) \cos\left(\frac{2\pi k}{N}\right) = \frac{1}{2} a_j a_k \left[ \cos\left(\frac{2\pi}{N}(j+k)\right) + \cos\left(\frac{2\pi}{N}(j-k)\right) \right].$$

(Similar terms arise if the function is expanded in a combination of sines and cosines.) Here we get new cosine terms with frequencies that are respectively the sum and the difference of the old ones. This applies even if the multiplication is done in real space, since these new terms will show up once the function is transformed again.

In a continuous representation this would not matter but here we have a discrete number of points in which the function is "sampled". Since we have only a finite number of modes the new modes may have frequencies that are too high to be represented with the given number of modes and so information about the system disappears out of the high end of the spectrum. But what is worse, these terms will show up in the low end of the spectrum. The reason for this can be seen in Fig. 30. In this figure are shown the arguments for the expansions in sines and cosines,

$$a_j \cos\left(\frac{2\pi}{N} j\right) + b_j \sin\left(\frac{2\pi}{N} j\right)$$

for the transformation in the azimuthal direction. The expansion goes from 0 to  $N/2 - 1$ , so the points only cover the upper half of the circle. (The situation in the radial direction is the same since there we step  $\pi/N$   $N$  times and so still go from 0 to  $\pi$ .) Now if two sufficiently high modes are multiplied the new term will move into the lower half of the circle. But as we have that

$$\cos(\pi + \pi) = \cos(\pi - \pi)$$

and

$$\sin(\pi + \pi) = -\sin(\pi - \pi)$$

we see that the modes in the lower half of the circle will give a false contribution to the modes in the upper half. In the extreme case, if the highest modes,  $\cos(2\pi/N \cdot N/2)$  are multiplied together they will contribute to the DC-level, which is certainly not physical. This phenomenon is completely analogous to the situation in analog-to-digital signal processing when one attempts to sample a signal with a sampling frequency lower than two times the highest frequency present in the signal. This problem is known as *aliasing*.

One may choose many different ways of avoiding this problem. The one employed here to "dealias" is very simple. If we remove all modes with a frequency higher than two-thirds of the maximum frequency we will cut out a "pie slice" of the circle. (see Fig. 30). The angle of the slice is  $2\pi/3$ . Now if we multiply the highest retained modes together, the product will fall into the part that was cut out. It will no longer be possible to excite modes in the lower part of the circle. Of course the cut-out part will be filled with terms when the multiplication is performed and these modes must be removed again after the multiplication. This method works well as can be seen from the results from the code below. The obvious drawback is that we effectively only use  $(\frac{2}{3})^2 = \frac{4}{9}$  or around 44 % of the modes we have represented.

#### Evaluating the solution by calculating invariant quantities.

Due to the finite number of modes and the finite-difference time step the obtained solution will not be exact. We therefore need some indication of how well the code is performing. For this purpose we can use some quantities which should be invariant in time for this particular problem. Two of these are:

$$\int_{\mathcal{A}} |\mathbf{v}|^2 d\sigma = \text{const.} \quad (51)$$

and

$$\int_{\mathcal{A}} \rho^2 d\sigma = \text{const.} \quad (52)$$

Since the fluid is incompressible Eq. 51 simply expresses that  $\frac{1}{2}\rho|\mathbf{v}|^2$  is invariant, in other words that kinetic energy is conserved. The other invariant is not quite as self-evident, but it is easy to derive from the original equations. Euler's equation can be written as:

$$\frac{\partial \rho}{\partial t} = -\nabla \cdot (\rho \mathbf{v}).$$

By multiplying with  $\rho$  we get

$$\rho \frac{\partial \rho}{\partial t} = -\rho \nabla \cdot (\rho \mathbf{v}) \quad \Rightarrow$$

$$\frac{1}{2} \frac{\partial \rho^2}{\partial t} = -\frac{1}{2} \nabla \cdot (\rho^2 \mathbf{v}).$$

Integrating over the entire area gives:

$$\frac{1}{2} \frac{\partial}{\partial t} \int_A \rho^2 d\sigma = -\frac{1}{2} \int_A \nabla \cdot (\rho^2 \mathbf{v}) d\sigma$$

and using Gauss' theorem we can write:

$$\int_A \nabla \cdot (\rho^2 \mathbf{v}) d\sigma = \oint_{S_i+S_o} \rho^2 \mathbf{v} \cdot \mathbf{n} ds$$

where the contour integral is to be taken over both the inner and outer boundaries. But since transport across the boundaries is not allowed  $\mathbf{v}_r = 0$  on the boundaries and hence  $\mathbf{v} \cdot \mathbf{n} = 0$ . This yields:

$$\frac{\partial}{\partial t} \int_A \rho^2 d\sigma = 0$$

from which we immediately get Eq. 52.

This proves that these two quantities are conserved in time for an exact solution. In our case we only employ a finite number of modes to describe the solution. It is possible to prove that in pseudospectral methods where only Fourier expansion is used these quantities will still be conserved even though only a finite number of modes is present ("rugged invariance"[18]). However, in the present case the solution is partly described by Chebyshev polynomials. Furthermore the invariance of  $\rho^2$  and  $v^2$  will be destroyed both by the dealiasing and by the finite-difference method used for the time integration. So we would not expect these "invariants" to be invariant. But they do offer information about how far the solution has diverged from the exact one. These quantities are thus calculated every few timesteps and the results saved in a file from which they may be read and displayed after the program has run.

### 3.3 Numerical results.

#### Code optimisation

The code for this simulation has been implemented on two different computers: the VAX-8700 at Risø and the Amdahl VP-1100 supercomputer<sup>3</sup> at UNI-C. The VAX only has one processor and so there is not much to be done in optimizing the code. On the VP-1100, however, the performance can depend very strongly on small adjustments in the code.

The VP-1100 is a vectorprocessor and so has the ability to perform several identical tasks simultaneously. The compiler automatically vectorizes DO-loops in FORTRAN, provided the tasks in the loop are independent. For instance, in the two examples given here:

```
DO I=1, 1000
  C(I) = A(I) + B(I)
END DO
```

```
DO I=1, 1000
  C(I) = A(I) + C(I-1)
END DO
```

the loop on the left hand side can be vectorized while the other cannot, as the result in the i'th step depends on the i-1'th. When executing nested DO-loops the compiler can vectorize the innermost loop but not the outer ones.

On the VP1100 there is a facility to analyze the vectorization of a given program. This consists of simply stopping the program at random points and asking whether

<sup>3</sup>Well, almost supercomputer



the instruction being performed is vectorized or not. The degree of vectorization is expressed in % for each subroutine.

Some parts of the program lend themselves particularly well to vectorization. Thus the subroutine solving Poisson's equation can reach a degree of vectorization of around 98%. For this reason the time taken to solve Poisson's equation is only around 7% of the total CPU time. Other parts are equally efficient, such as the differentiation and division in transformed space. The greatest problem lies with the Fast Fourier Transform (FFT). Traditionally, a two-dimensional FFT has been performed on the VAX by first doing a one-dimensional FFT on each column in the array, and then doing the same on each row. However, the FFT requires many rearrangements of the elements in the vector to be transformed (actually a reversal of the bits in the address of each element[19]). Therefore the one-dimensional FFT is hard to vectorize. Implementing the VAX code unaltered on the VP1100 yielded a vectorization degree of only a few percent. Even the vectorized library routines for one-dimensional FFT on the VP1100 could only attain about 40%. The solution is to perform all the FFT's at once. Instead of exchanging the place of two numbers in a vector two entire vectors are exchanged simultaneously. Thus the vectorization of the FFT's approach 90%. These vectorization degrees cannot be translated directly into a measure of performance. But this change yielded an overall increase in speed of a factor 2.5, even over the vectorized one-dimensional FFT. Still, the two FFT's together take up around 70% of the time spent running the code, so it is important not to perform any unnecessary transformations.

Another fine-tuning of the code relates to the so-called *memory bank conflict*. On the VP-1100 the RAM memory is divided into 128 banks and successive bytes of data are stored in different banks. Different banks can be accessed simultaneously but two numbers in the same bank require two successive read operations. So if the bytes to be read are stored at intervals of 128 they will all lie in the same bank and require many read operations. This is the bank conflict. It is best resolved by always having arrays with an odd number of elements. In the case considered here, where we require that the number of modes be a multiple of 2 there is a great risk of memory bank conflict. To avoid this the number of elements in each dimension was increased by one (unused) element. This seemingly innocuous modification actually increased the speed of the code by 20 % at a price of a small amount of wasted memory!

Altogether the code has become very efficient. When a large number of modes is employed (e.g.  $32 \times 128$  or greater) the program runs at a speed of  $\sim 50-60$  MFlops (million floating point operations per second). The theoretical maximum for the VP-1100 is 286 MFlops. However, this limit is hardly ever approached for realistic programs. Among programs performing a variety of tasks this code is actually one of the faster ones implemented on the VP-1100.

### Initial results

To check the correctness of the code implementation the first runs were made with special initial and boundary conditions. Solutions were found which were stationary or uniformly rotating. It was explicitly verified that these runs behaved as expected.

To excite the Kelvin-Helmholtz the initial condition was taken to be  $\phi(a) = \phi(b) = 0$  and

$$\rho(x, \theta, t = 0) = \left[ P \cdot \left( \frac{B}{\cosh^2(Bx)} \right) + \frac{1}{x+A} \cdot \tanh(Bx) + \epsilon \cos(k\pi n\theta) \right] \cdot (1-x^2)^2 \quad (53)$$

where  $A$ ,  $B$  and  $P$  are adjustable parameters and  $n$  is an integer. This will set up

a strong shear in the motion of the fluid. However, this will not in itself excite the instability. This situation is an unstable equilibrium as there is no  $\theta$ -dependence. To disturb the equilibrium a small sinusoidal variation in the azimuthal direction is superimposed.

There are two remaining independent parameters to be specified in order to run the code. One is the time step size,  $\Delta t$  and the other is the radius  $a$  (see Fig. 27). In some respect these two parameters are not quite independent, because of the *Courant criterion*. This makes the requirement that

$$v \cdot \frac{\Delta t}{\Delta x} \ll 1$$

where  $v$  is the fluid velocity in some direction and  $\Delta x$  the spacing between any two grid points. This criterion states that within one time step the fluid must move a distance that is much smaller than the grid spacing if the calculation is to remain stable. The reason for this is that the explicit time integration uses information about the conditions at earlier time points. This information is used together with the present state of the system to calculate the evolution (sec. 3.2). Therefore the old information must pertain to approximately the same fluid element as the present information. Hence, if the radius is diminished, the grid points will lie closer, especially on the inner boundary and thus the time step size must also be diminished. For the same reason the number of modes is higher in the azimuthal direction than radially (normally  $4 \times$  higher). A special feature has been included in the program to calculate the Courant criterion in both radial and azimuthal direction. It calculates the fluid velocity using Eq. 7.

A trial run with  $32 \times 128$  modes and  $k$  in Eq. 53 equal to 2 is seen in Fig. 31. The evolution of  $\rho$  and  $\phi$  is shown here for six different times. The most obvious feature of this run is the emergence of two vortices seen in both figures. This clearly shows that the flow is indeed unstable and that vortices develop spontaneously from very small deviations from equilibrium. The experimental analogue of Fig. 31b is Fig. 6. The similarity is quite clear. Of course this does not necessarily indicate that the driving mechanisms are the same in the experiment and the simulation. Also the conditions are not exactly the same. In the experiment all the plasma moves in the same direction, only with different angular velocities. In the simulation some of the plasma moves in the opposite direction. Therefore the vortices seem to be stationary or at least moving only slowly in the simulation whereas they have a large azimuthal velocity in the experiment. Nevertheless, this simulation shows that a velocity gradient is sufficient for the instability to arise and form vortices.

Another, less fortunate feature of Fig. 31 is the emergence in the last pictures in Fig. 31a of regions of very large positive and negative charge. This is not a physical phenomenon but an artefact of the numerical method. The fast fluctuations arise when an attempt is made to Fourier (or Chebyshev) transform a function with large gradients. This is known as *Gibbs' phenomenon* or *ringing* and is discussed in more detail in for instance Coutias et al.[20]. The sharp gradients occur when the vortices form. As can be seen from the figure thin threads connect the forming vortices. The ringing arises around these threads. The reason it only occurs in  $\rho$  and not in  $\phi$  is that  $\rho$  is the second derivative of  $\phi$  and therefore has the largest gradients.

The ringing is self-amplifying and will sooner or later ruin the simulation. The evolution of the "invariants" is shown in Fig. 32. The sharp rise in both curves is mainly due to the ringing.

The most obvious way to remedy this is to introduce a larger number of grid points (and thus more modes). In Fig. 33  $64 \times 256$  modes have been used. It is

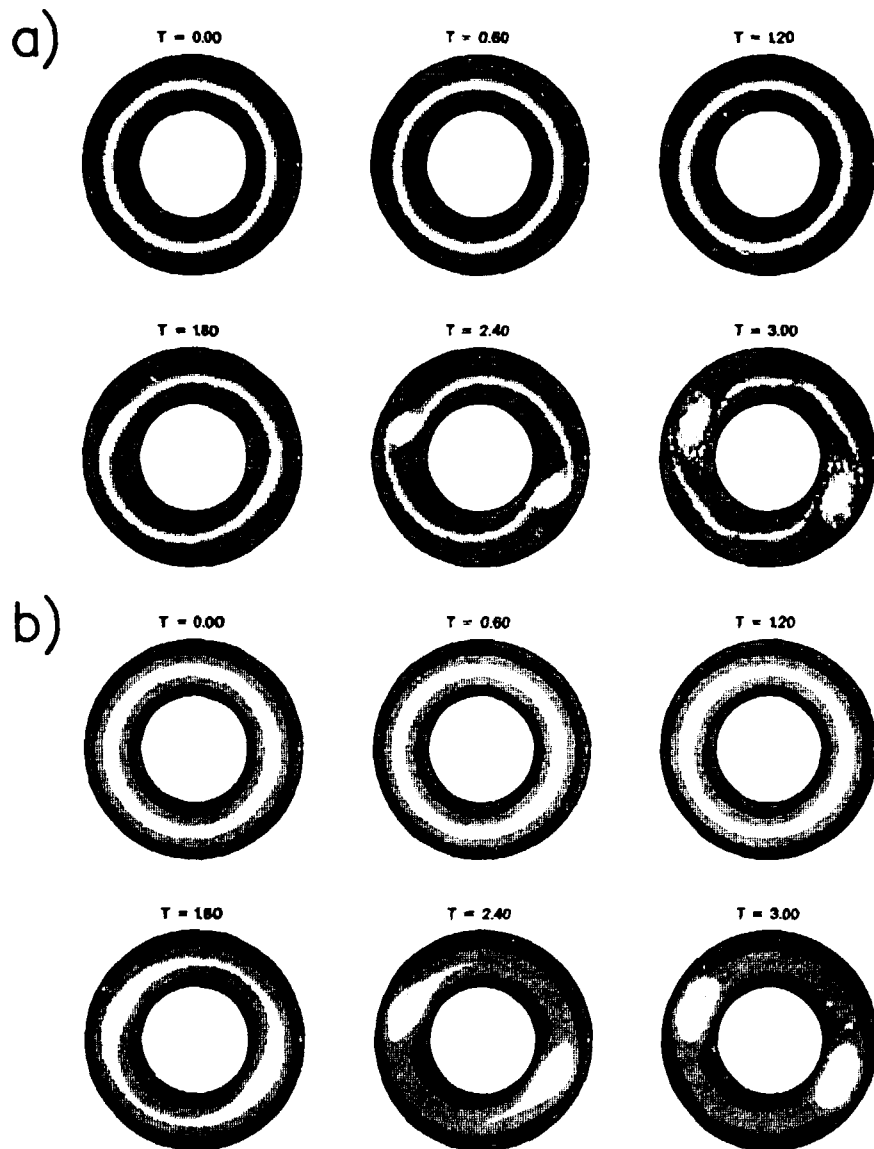


Figure 31. a)  $\rho(x, \theta, t)$  for six different times. Here  $\alpha = 3.0$ ,  $\Delta t = 1 \cdot 10^{-3}$ ,  $P = 3$ ,  $B = 5$ , and  $\epsilon = 0.2$ . b)  $\phi(x, \theta)$  at the same time points. High values are white, low values dark in the plots.

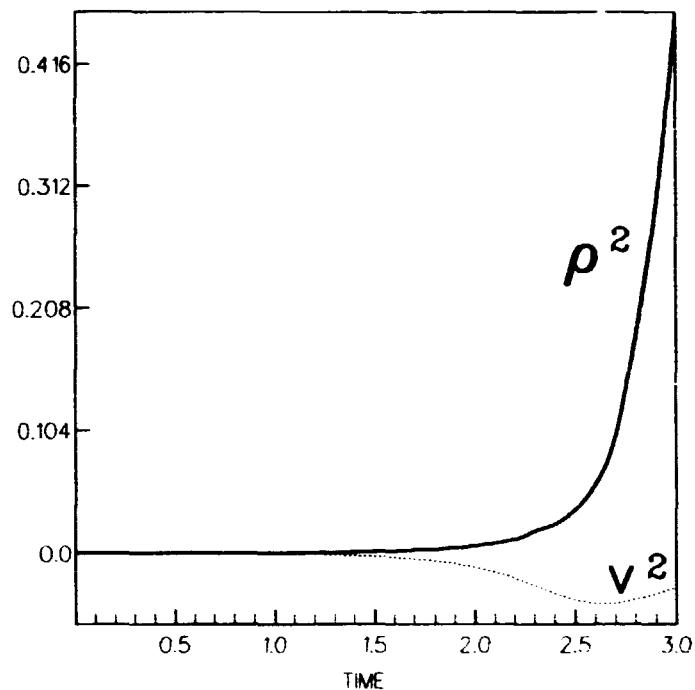


Figure 32. Invariants of  $\rho^2$  and  $v^2$  for the simulation in Fig. 31. The curve shows the evolution of the relative change from the initial value.

clear that this gives a large improvement though the price is a factor of 8 in the execution time (the time step must be halved to satisfy the Courant criterion). However, this remedy only postpones the problems. In the last pictures in Fig. 33 the ringing arises again.

It was also found that applying a fully corrected time integration scheme improved things. With the fully corrected scheme the ringing still arises but it does not grow nearly as fast as in the partially corrected scheme. In Fig. 34-35 are shown sample runs with  $32 \times 128$  modes and  $k = 7$ , both with partially and with fully corrected schemes. However, the fully corrected scheme cannot prevent the ringing from arising.

Though the fully corrected time integration cannot entirely solve the problem of the ringing it has enabled us to perform some experiments on the code. For instance we may try a different perturbation. In Fig. 34b is shown a run where  $k = 7$ . It is clearly seen that this time seven vortices form out of the sheared flow. This shows that we may control the number of vortices simply by applying a suitable perturbation.

Another possibility is to give an initial perturbation which is not strictly sinusoidal. In this way the vortices forming will not be equidistant and thus they may interact. Fig. 36 shows an example of such a simulation where the perturbation is of the form  $\epsilon_1 \sin(7\theta) + \epsilon_2 \sin(\theta)$ . At first, the vortices form in much the same way as in Fig. 34b, but later on the vortices start to coalesce. This is not surprising since the vortices have the same polarity (as can be seen from the plots of the potential which corresponds to the stream function). At the end of the run almost all the charge (vorticity) has been sucked into one large blob. This simulation has a close experimental analogy in an experiment performed by Pécseli et al.[21]. In this experiment two convective cells were injected into the edge of a Q-machine. It was observed that when the two cells were of the same polarity they would

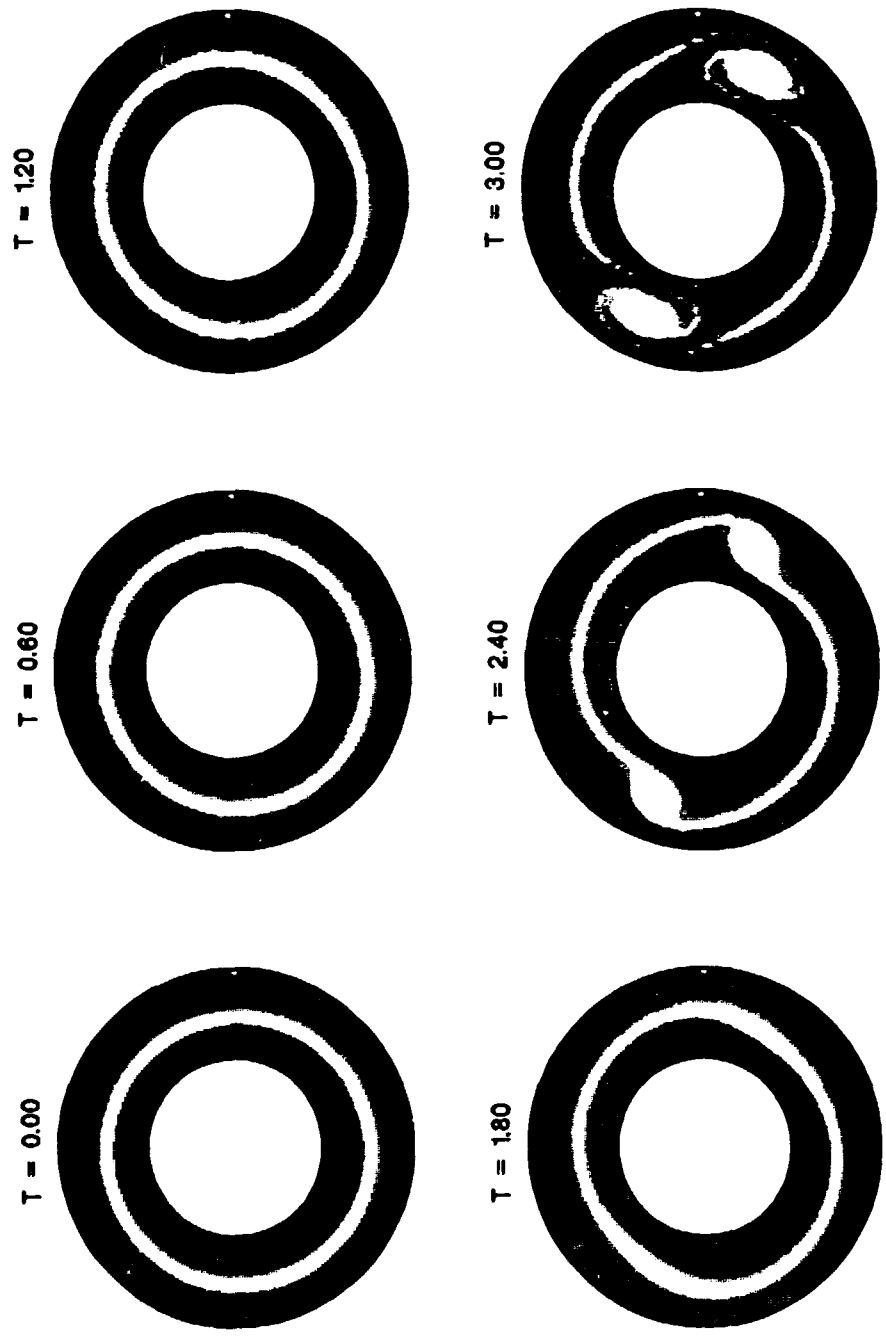
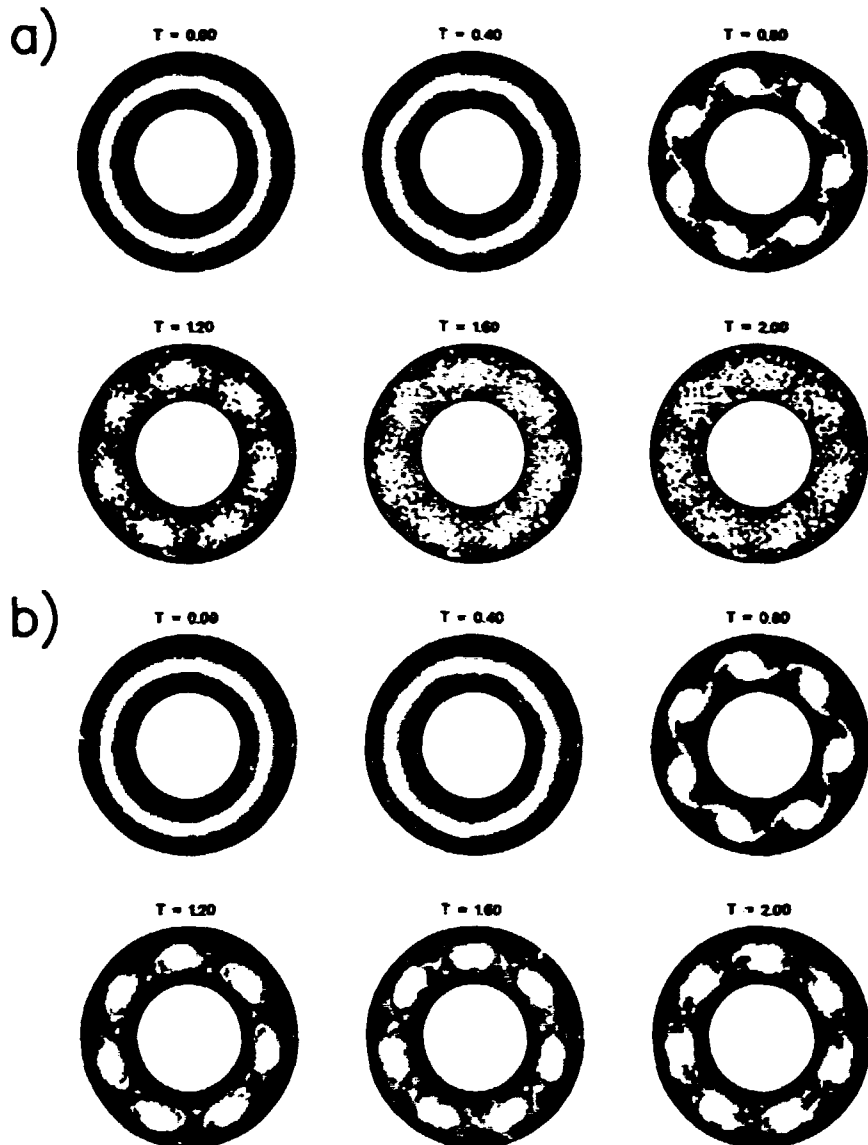


Figure 33. As Fig. 31a, only for  $64 \times 256$  modes and with  $\delta t = 5 \cdot 10^{-1}$ .



**Figure 34.** a)  $\rho$  at 6 different times with  $32 \times 128$  modes and  $k = 7$ ,  $P = 6$  and  $\epsilon = 0.5$  with partially corrected time integration. b) As a) but with fully corrected time integration.

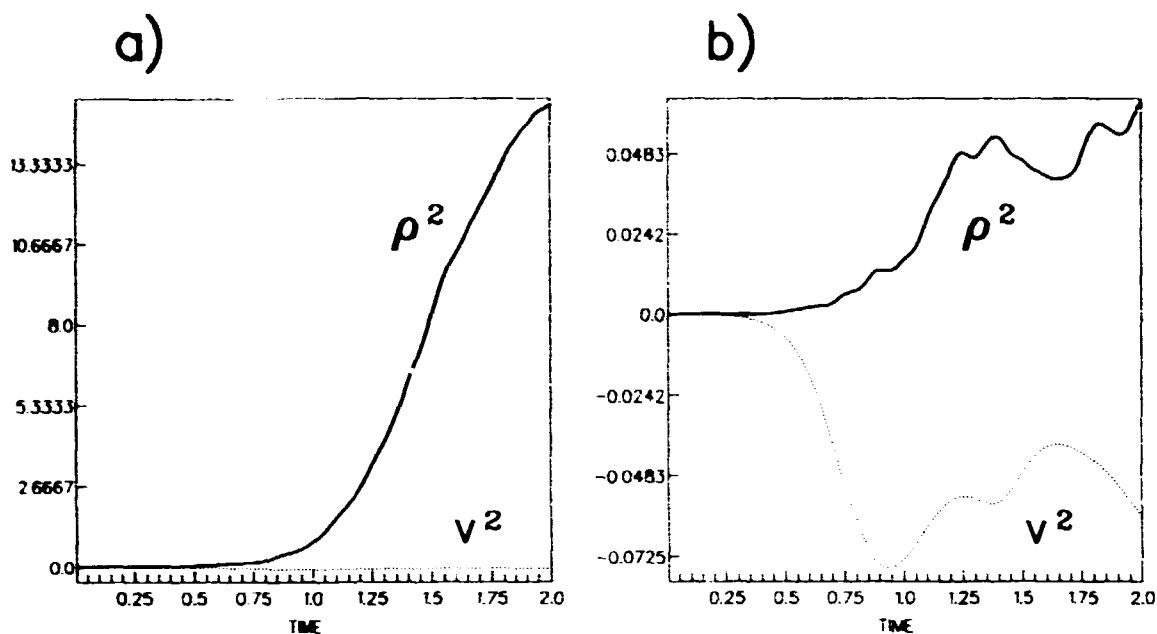


Figure 35. Evolutions of the invariants in the two runs of Fig. 34. a) partially corrected scheme, b) fully corrected scheme. Note the different scales in the two plots.

coalesce in a manner similar to that seen in this simulation.

### 3.4 Attempts at removing the ringing

It is the attempt to transform functions with large gradients that leads to the ringing. The result is that the high order modes are amplified disproportionately. Therefore it may make sense to selectively damp these high modes. This can be done by simply applying a filter to the high modes in transformed space, but the relevance of this method to physical phenomena is not clear. A more "natural" method would be to introduce viscosity into the equations of motion for the fluid. In the hydrodynamic equations this enters into the two-dimensional Navier-Stokes equation:

$$\frac{\partial \mathbf{v}}{\partial t} + \mathbf{v} \cdot \nabla \mathbf{v} - \nabla p + \nu \nabla^2 \mathbf{v} = 0 \quad (54)$$

where  $p$  is the pressure and  $\nu$  denotes the strength of the viscosity. Taking the curl of this equation yields:

$$\frac{\partial \boldsymbol{\omega}}{\partial t} + \mathbf{v} \cdot \nabla \boldsymbol{\omega} + \nu \nabla^2 \boldsymbol{\omega} = 0 \quad (55)$$

where  $\boldsymbol{\omega} = \nabla \times \mathbf{v}$ . The pressure gradient vanishes identically.

The Laplacian of the charge can be calculated in a way similar to that of the gradient operator. In principle then, this new term could simply be incorporated into the timestepping. However, this would be very prone to become unstable. The reason for this can most readily be seen when looking at the Fourier transform in the azimuthal direction. The second derivative of the Fourier terms will be of the form  $\nu \Delta t (-n^2) \rho_{m,n}$ . If  $\nu$  is chosen correctly, this new term will cancel

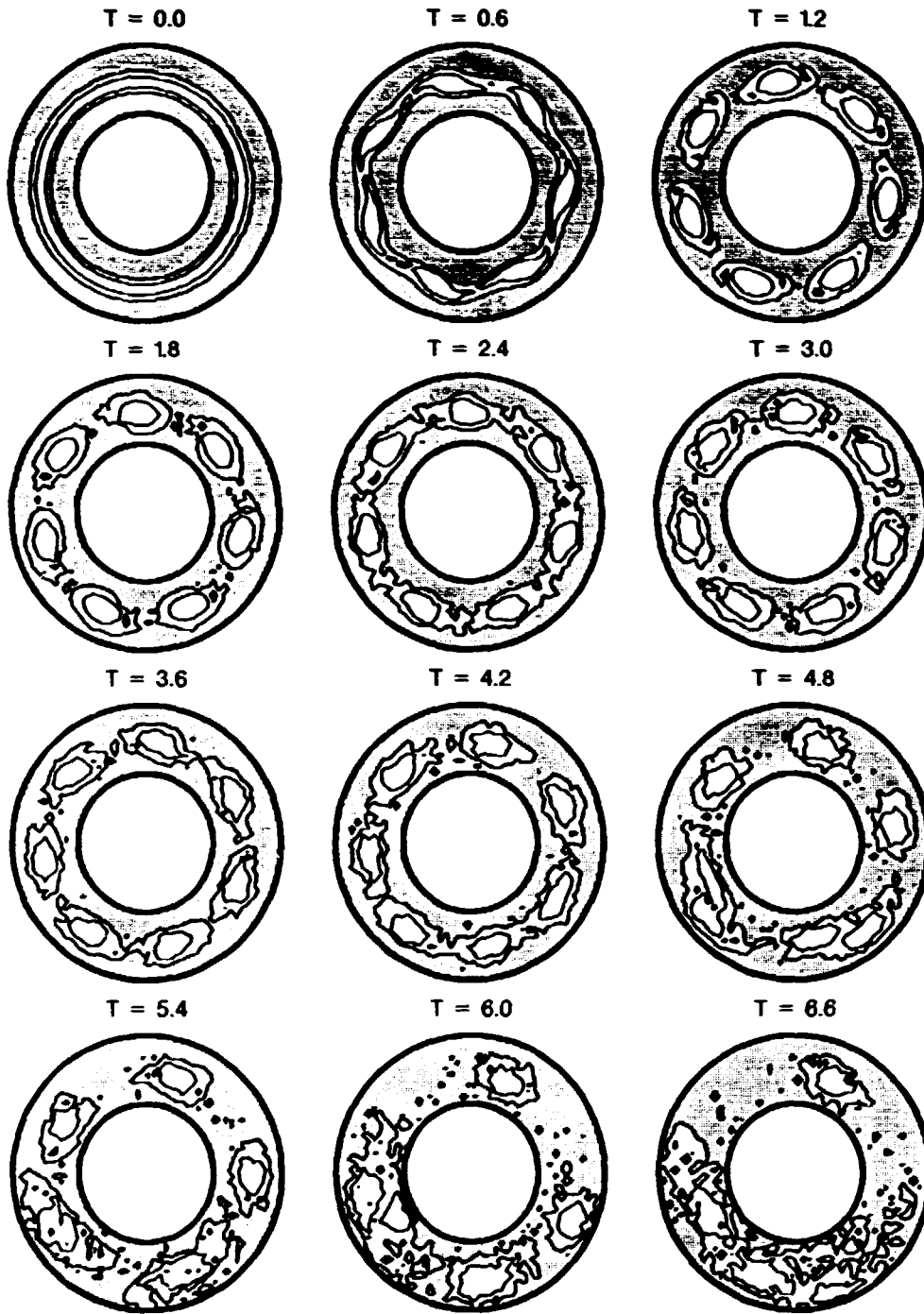


Figure 36. a)  $\rho$  at 12 different times with  $64 \times 256$  modes and  $k = 7$ , with a further asymmetrical perturbation of the form  $\sin(\theta)$ .



the contributions to the high modes, which is just what viscosity is supposed to do. But if  $\nu$  is too large the viscosity term may actually make the high modes numerically larger and thus lead to an instability.

The way around this difficulty is to solve the timestepping for the new term in an implicit way. The third order (fully corrected) Adams-Bashforth time integration would then look like:

$$\tilde{\rho}_{m+1}^* = \rho_m^* + [23G_m - 16G_{m-1} + 5G_{m-2}] \frac{\Delta t}{2} + \nu \Delta t \nabla^2 \rho_{m+1}^*, \quad (56)$$

$$\rho_{m+1}^* = \rho_m^* + [5\tilde{G}_{m+1} + 8G_m - G_{m-1}] \frac{\Delta t}{2} + \nu \Delta t \nabla^2 \rho_{m+1}^*, \quad (57)$$

where  $\rho^* = r^2 \rho$ . This can be written as

$$(r^2 - r^2 \nu \Delta t \nabla^2) \tilde{\rho}_{m+1}^* = \rho_m^* + [23G_m - 16G_{m-1} + 5G_{m-2}] \frac{\Delta t}{2}, \quad (58)$$

$$(r^2 - r^2 \nu \Delta t \nabla^2) \rho_{m+1}^* = \rho_m^* + [5\tilde{G}_{m+1} + 8G_m - G_{m-1}] \frac{\Delta t}{2}. \quad (59)$$

The left hand sides in Eqs. 58- 59 can be solved in a way similar to the solving of Poisson's equation. Indeed we already have a code for solving  $r^2 \nabla^2 \phi = -r^2 \rho$ . In this case, since there is one more term here, the system of equations becomes nonadiagonal and not pentadiagonal as the standard Poisson solver. However, since Eq. 55 is now a *fourth* order differential equation for  $\phi$  in space it becomes necessary to specify an additional set of boundary conditions. The simplest way is to prescribe a fixed  $\rho$  at the boundaries. However, this may create sharp gradients in  $\rho$  close to the boundaries. This will lead to a numerical instability which completely destroys the solution in only a few timesteps, unless  $\nu$  is very large (of the order of unity) in which case everything decays exponentially and the flow is no longer unstable.

Other simple solutions have been tried, such as ignoring boundary conditions altogether or forcing them to be equal to their values at the previous timestep. These too however, lead to strong numerical instabilities which completely destroy the solutions in only a few timesteps. Therefore the problem of adding viscosity is not yet solved. Further ideas are under investigation, but no definite results have yet appeared. Therefore this will not be further described here.

### 3.5 Future developments

If (when) the problems with ringing are solved the code will be used for several purposes. One is to study the diffusion of test particles due to the instability. This will be done in a way similar to the one described by Knorr et al.[18]. This will be of great interest since it allows a comparison with the experimental results of chapter 2.

Another potential use of this simulation is to study vortex dynamics in greater detail. Recent investigations[22] have indicated that a wide range of phenomena, such as for instance the red spot on Jupiter can be simulated by an instability due to a velocity shear in a cylindrical region. These investigations have focused on the evolution of an already existing vortex. With this code it may be possible to study the emergence of vortices in such systems as well as their evolution.

## 4 Experiments on wave propagation and instability in a plasma with an ion beam

### 4.1 Introduction

One of the most widely investigated problems in plasma physics is the problem of a beam of charged particles injected into a plasma, or alternatively, of a plasma in which one species of particles is moving relative to the others. One example of this is a current carrying plasma where the electrons will have a nonzero average velocity relative to the ions. This will in some cases give rise to the *two-stream* or *beam instability*. In the Risø Double-Plasma machine a beam of moderately fast ions is injected into a stationary plasma. Depending on the beam velocity and intensity we may excite the ion beam instability, or we may study other phenomena of the interaction between the beam and the plasma.

This chapter is divided into a theoretical and an experimental part. In the theoretical part I will present some analytical calculations of the plasma response to a weak beam of charged particles and present some computer calculations of this. Then I will give a brief exposé of the theory of the beam instability. In the experimental I will describe the results obtained with the DP-machine on Čerenkov radiation from a weak supersonic beam and on the beam instability.

### 4.2 Analysis of the plasma response to a dilute beam of fast ions.

In this section the problem of the plasma response to the injection of a dilute beam of ions will be discussed. The mathematical treatment of this problem is essentially due to H. L. Pécseli.

The term "dilute" is here used to denote a beam of ions so weak that the ions in the beam do not interact perceptibly. Also, the weak beam cannot excite the beam-plasma instability. Therefore the plasma response can be seen as the superposition of the response to a single ion and it is this response which will be calculated here. Also, in the following the effect of the plasma on the beam ions will not be taken into account.

#### Calculations in one spatial dimension

The natural starting point for this calculation is the Vlasov equation for the ions:

$$\frac{\partial f}{\partial t} + \mathbf{v} \cdot \nabla f + \frac{e\mathbf{E}}{M_i} \frac{\partial f}{\partial \mathbf{v}} = 0 \quad (60)$$

where  $f$  is the normalised distribution function for the ions. We shall here consider a perturbed stationary solution. Thus we have  $\mathbf{E}_0 = 0$  and  $f_0 = f_0(\mathbf{v})$  with  $\int f_0(\mathbf{v}) d\mathbf{v} = 1$ . Initially, we will take the perturbation to be that of a single ion with charge  $q$  introduced at  $t = 0$  and  $\mathbf{x} = 0$  and immediately removed again. The disturbance will then be of the form  $q\delta(\mathbf{x})\delta(t)$ . For simplicity we shall start with the one-dimensional Vlasov equation, which in its linearised form is:

$$\frac{\partial f}{\partial t} + v \frac{\partial f}{\partial x} - \frac{e}{M_i} \frac{\partial \phi}{\partial x} f'_0(v) = 0 \quad (61)$$

where we have introduced  $\mathbf{E} = -\nabla\phi$ , i.e. the electrostatic approximation.

A second relation between  $f$  and  $\phi$  can be obtained by using Poisson's equation:

$$\nabla^2 \phi = \frac{e(n_e - n_i)}{\epsilon_0} \quad (62)$$

We shall make two further assumptions. One is that the electrons behave isothermally and are distributed according to the Boltzmann distribution, i.e.  $n_e = n_{e0} e^{-\phi/T_e}$ . The other is that we have quasineutrality,  $n_e = n_i$ . With these assumptions the left hand side of Eq. 62 vanishes and we have

$$n_i = \int f(x, v, t) dv = \frac{e\phi}{T_e} - \phi(x)\delta(t) \quad (63)$$

where  $n_i$  is the perturbed ion density, normalised by  $n_{i0}$ .

We now perform a Fourier transform in space and a Laplace transform in time, where we use  $i\omega$  for the traditional Laplace variable  $s$ . Eqs. 61 and 63 then become:

$$-i\omega f(k, \omega, v) + ikv f(k, \omega, v) - \frac{e}{M_i} ik\phi(k, \omega) f_{i0}(v) = 0 \quad (64)$$

and

$$\int f(k, \omega, v) dv = \frac{e}{T_e} \phi(k, \omega) - q \quad (65)$$

where  $f$  and  $\phi$  now denote the transformed functions. We have here used the initial condition  $f(x, v, t = 0) = 0$  and the fact that the Laplace and Fourier transform of a delta function is unity. It should be noted that here  $\omega$  is a complex number with a positive imaginary part, while  $k$  is real.

Eliminating  $f$  we get:

$$\frac{e\phi}{T_e} - q = \int \frac{e}{M_i} \phi \frac{f'_{i0}(v)}{v - \frac{\omega}{k}} dv = \frac{e\phi}{T_e} \frac{T_e}{M_i} \int \frac{f'_{i0}(v)}{v - \frac{\omega}{k}} dv. \quad (66)$$

But due to the quasineutrality we have  $e\phi/T_e = n(k, \omega)$  and so we get

$$n(k, \omega) = \frac{q}{1 + \frac{T_e}{M_i} \int \frac{f'_{i0}(v)}{v - \frac{\omega}{k}} dv}. \quad (67)$$

This equation can then be solved by performing the inverse Fourier and Laplace transforms. The inverse Fourier transform will be treated first. This is given by

$$n(x, \omega) = \frac{q}{2\pi} \int_{-\infty}^{\infty} n(k, \omega) e^{ikx} dk. \quad (68)$$

The solving of this is not an obvious matter. Here we will follow the method of Mason[23] in the way used by Andersen et al.[24]. In the integral in the denominator we have a pole at  $v = \omega/k$ . When  $k < 0$  the imaginary part of  $\omega/k$  is negative. Thus when we integrate along the real  $v$ -axis we integrate above the pole. Similarly, when  $k > 0$  we integrate below the pole. Therefore we should split the integral in Eq. 68 into two:

$$n(x, \omega) = \frac{q}{2\pi} \left( \int_{-\infty}^{\omega} n_1(x, \omega) e^{ikx} dk + \int_{\omega}^{\infty} n_2(x, \omega) e^{ikx} dk \right) \quad (69)$$

where  $n_{1,2}(x, \omega)$  are given by

$$n_{1,2}(x, \omega) = \frac{1}{1 + \frac{T_e}{M_i} \int_{1,2} \frac{f'_{i0}(v)}{v - \frac{\omega}{k}} dv}. \quad (70)$$

The two integration paths in Eq. 70 run above and below the pole, respectively.

If we consider the line  $\omega/k = v$  in the complex  $k$ -plane as shown in Fig. 37 we see that in the region to the left of the line we have  $\text{Im} \omega/k < 0$ , i.e. the integration along the real  $v$ -axis runs above the pole. Therefore  $n_1(k, \omega)$  is defined in this region. Similarly,  $n_2(k, \omega)$  is defined in the region to the right of the line. Therefore we can perform an integration around a closed contour in each region. The results of these integrations will depend only on the poles of the functions in eq. 70. These poles can only arise from the denominator becoming equal to zero. Now, it may be shown by a Nyquist analysis that the functions  $n_{1,2}(k, \omega)$

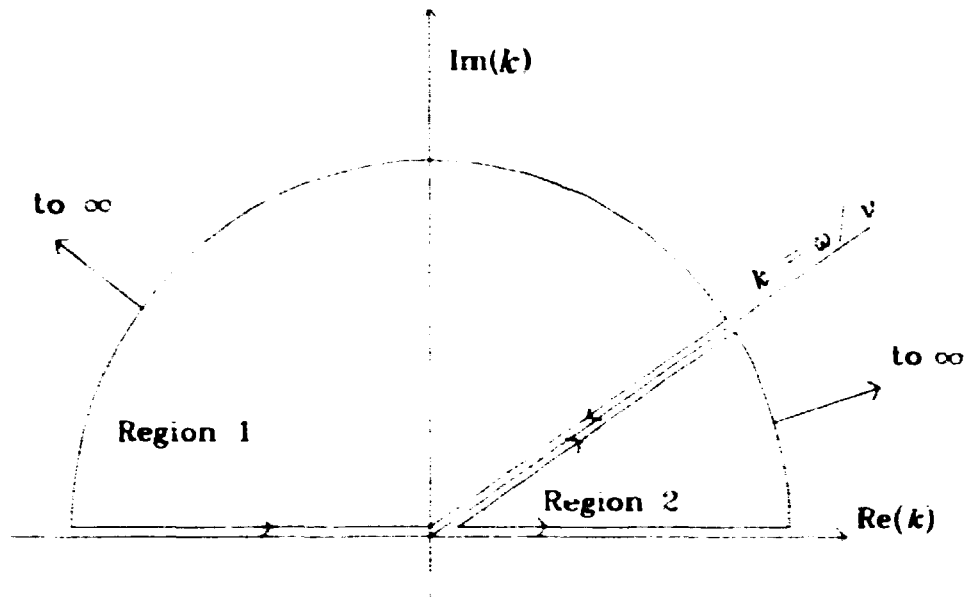


Figure 37. Integration contours in the  $k$ -plane.

are both analytical in the areas where they are defined (see App. C). Thus there are no poles for the functions inside the integration contours and both contour integrals are equal to zero. The integrals along the  $k$ -axis are then equal to the integrals along the line  $k = \omega \nu$  with the directions shown in fig. 37. Eq. 69 will then become

$$\begin{aligned} n(x, \omega) &= \frac{q}{2\pi} \left( \int_{-\infty}^{\infty} n_1(\nu) \frac{-\omega}{\nu^2} e^{i\omega\nu} d\nu - \int_0^{\infty} n_2(\nu) \frac{-\omega}{\nu^2} e^{i\omega\nu} d\nu \right) \\ &= \frac{q}{2\pi} \int_0^{\infty} \frac{\omega}{\nu^2} (n_1(\nu) - n_2(\nu)) e^{i\omega\nu} d\nu. \end{aligned} \quad (71)$$

The inverse Laplace transform is easily performed by noting that the inverse Laplace transform of  $-\omega e^{i\omega\nu} = \delta'(\frac{x}{\nu} - t)$  where  $\delta'(x)$  is the derivative of Dirac's delta function. We then get:

$$n(x, t) = \frac{-i}{2\pi} \int_0^{\infty} \frac{1}{\nu^2} (n_1(\nu) - n_2(\nu)) \delta'(\frac{x}{\nu} - t) d\nu. \quad (72)$$

To solve this we make the substitution  $z = \frac{x}{\nu}$  whereby

$$n(x, t) = \frac{-i}{2\pi x} \int_0^{\infty} (n_1(\frac{x}{z}) - n_2(\frac{x}{z})) \delta'(z - t) dz.$$

We use integration by parts to obtain

$$\begin{aligned} n(x, t) &= \frac{-i}{2\pi} \int_0^{\infty} \frac{1}{z^2} (n_1'(\frac{x}{z}) - n_2'(\frac{x}{z})) \delta(x - z) dz \\ &= \frac{-i}{2\pi} (n_1'(\frac{x}{t}) - n_2'(\frac{x}{t})). \end{aligned} \quad (73)$$

Making use of the fact that

$$\int_1 \frac{h(v)}{x-v} dv = \left( \int_2 \frac{h(v)}{x-v} dv \right)' \quad \text{for } x \text{ real}$$

with the usual integration paths (see App. C) we find

$$n(x, t) = \frac{q}{\pi t^2} h'(\frac{x}{t}) \quad (74)$$

where

$$\begin{aligned}
 h(\xi) &= \text{Im} \left( \frac{1}{1 + \frac{T_e}{M_i} \int \frac{f'_0(v)}{\xi - v} dv} \right) \\
 &= \text{Im} \left( \frac{1}{1 - \left( \frac{T_e}{M_i} \rho \int \frac{f'_0(v)}{v - \xi} dv - i\pi f'_0(\xi) \right)} \right) \\
 &= \pi \frac{\frac{T_e}{M_i} f'_0(v)}{\left( 1 - \frac{T_e}{M_i} \rho \int \frac{f'_0(v)}{v - \xi} dv \right)^2 + \left( \pi \frac{T_e}{M_i} f'_0(\xi) \right)^2}.
 \end{aligned} \tag{75}$$

If we assume that the unperturbed ion distribution is Maxwellian we can express the response in terms of the plasma dispersion function. We then have:

$$\begin{aligned}
 f_0(v) &= \sqrt{\frac{M_i}{2\pi T_i}} e^{-\frac{M_i v^2}{2T_i}} \\
 f'_0(v) &= -\frac{1}{\sqrt{2\pi}} \left( \frac{M_i}{T_i} \right)^{3/2} v e^{-\frac{M_i v^2}{2T_i}}
 \end{aligned}$$

The integral in the denominator of  $h$  can now be evaluated. By making the substitutions  $y = \sqrt{M_i/2T_i}v = v/v_{ti}$  and  $\gamma = \sqrt{M_i/2T_i}\xi$  with  $v_{ti}$  being the ion thermal speed we get

$$\begin{aligned}
 \int_{-\infty}^{\infty} \frac{f'_0(v)}{v - \xi} dv &= \sqrt{\frac{M_i}{2\pi T_i}} \cdot \left( -\frac{M_i}{T_i} \right) \int_{-\infty}^{\infty} \frac{v e^{-\frac{M_i v^2}{2T_i}}}{v - \xi} dv \\
 &= \frac{1}{\sqrt{\pi}} \cdot \left( -\frac{M_i}{T_i} \right) \int_{-\infty}^{\infty} \frac{y e^{-y^2}}{y - \gamma} dy \\
 &= \frac{1}{\sqrt{\pi}} \cdot \left( -\frac{M_i}{T_i} \right) \left[ \sqrt{\pi} + \gamma \int_{-\infty}^{\infty} \frac{e^{-y^2}}{y - \gamma} dy \right] \\
 &= -\frac{M_i}{T_i} (1 + \gamma Z(\gamma)) = \frac{M_i}{2T_i} Z'(\gamma)
 \end{aligned} \tag{76}$$

where  $Z$  is the plasma dispersion function. Then we get

$$h(\gamma) = \frac{1}{1 - \frac{T_e}{M_i} \frac{M_i}{2T_i} Z'(\gamma)} = \frac{\frac{1}{2} Q \text{Im} Z'(\gamma)}{\left( 1 - \frac{1}{2} Q \text{Re} Z'(\gamma) \right)^2 + \left( \frac{1}{2} Q \text{Im} Z'(\gamma) \right)^2} \tag{77}$$

where  $Q = T_e/T_i$ .

Now we have the plasma response to a perturbation of the form  $q\delta(x)\delta(t)$ . In the following this will be denoted  $n_\delta(\frac{x}{t})$ . The response to a moving charge with a path given by  $x = v_0 t$  is found by considering the moving charge as a continuous succession of delta functions. This can be written as:

$$\begin{aligned}
 n^{(1)}(x, t) &= \int_0^t \int_{-\infty}^{\infty} \delta(x' - v_0 t') n_\delta(x - x', t - t') dx' dt' \\
 &= \frac{-q}{2\pi} \int_0^t \frac{1}{(t - t')^2} h' \left( \frac{x - v_0 t'}{t - t'} \right) dt'.
 \end{aligned}$$

By substituting  $\chi = \frac{x - v_0 t'}{t - t'}$  the above integral becomes

$$\frac{-q}{2\pi} \int_{x/t}^{\infty} \frac{1}{x - v_0 t} h'(\chi) d\chi = \frac{q}{2\pi(x - v_0 t)} h \left( \frac{x}{t} \right). \tag{78}$$

### Calculations in three dimensions

The plasma response in three spatial dimensions can now be calculated in a similar way. Here we will make the postulate that the response to a perturbation of form  $q\delta(\mathbf{r})\delta(t)$  has the following form

$$n_{\delta}^{(3)}(\mathbf{r}, t) = \frac{q}{t^n} H\left(\frac{\mathbf{r}}{t^m}\right).$$

The response in one dimension can be calculated from the above in the following way:

$$\begin{aligned} n_{\delta}^{(1)}(x, t) &= \frac{q}{t^n} \int \int \int_{-\infty}^{\infty} \delta(x') H\left(\frac{\sqrt{(x-x')^2 + (y-y')^2 + (z-z')^2}}{t^m}\right) dx' dy' dz' \\ &= \frac{q}{t^n} \int \int_{-\infty}^{\infty} H\left(\frac{\sqrt{x^2 + (y-y')^2 + (z-z')^2}}{t^m}\right) dy' dz' \\ &= \frac{2\pi q}{t^n} \int_0^{\infty} H\left(\frac{\sqrt{x^2 + \xi^2}}{t^m}\right) d\xi \\ &= \frac{\pi q}{t^n} \int_{x^2}^{\infty} H\left(\frac{\sqrt{\gamma}}{t^m}\right) d\gamma \end{aligned}$$

where first  $\xi^2 = (y-y')^2 + (z-z')^2$  and later  $\gamma^2 = \xi^2 + x^2$  was introduced. This is now the one-dimensional response to a delta function in time and space. But this must then be equal to the result obtained in Eq. 74. We therefore have:

$$\frac{\pi q}{t^n} \int_{x^2}^{\infty} H\left(\frac{\sqrt{\gamma}}{t^m}\right) d\gamma = \frac{q}{\pi t^2} h'\left(\frac{x}{t}\right).$$

Differentiating this by  $x$  we get

$$\frac{-2\pi q}{t^n} x \cdot H\left(\frac{x}{t^m}\right) = \frac{-q}{\pi t^2} h''\left(\frac{x}{t}\right) \cdot \frac{1}{t}$$

or

$$\frac{1}{t^n} H\left(\frac{x}{t^m}\right) = \frac{1}{2\pi^2} \frac{1}{t^1} \left[ \frac{t}{x} h''\left(\frac{x}{t}\right) \right]. \quad (79)$$

From this we see that  $n = 4$  and  $m = 1$ . Thus we have

$$n_{\delta}^{(3)} = \frac{q}{2\pi^2 t^4} \frac{t}{x} h''\left(\frac{x}{t}\right). \quad (80)$$

The response to a moving charge in three dimensions can now be calculated in the same way as for the one-dimensional case. The charge is moving in the positive  $x$ -axis with speed  $v_0$ . This yields:

$$n(\mathbf{r}, t) = \int_0^t \frac{1}{(t'-t)^4} \frac{t'-t}{\sqrt{x^2 + y^2 + (z-v_0 t')^2}} h''\left(\frac{\sqrt{x^2 + y^2 + (z-v_0 t')^2}}{t'-t}\right) dt'. \quad (81)$$

This is the response of the plasma to a charge moving with constant velocity  $v_0$ . This expression can easily be evaluated numerically. Since the theory is linear this expression can be extended to a spatial distribution of moving ions simply by superposition. This is also done easily numerically as will be shown in the next section.

### Numerical calculation of the plasma response

The evaluation of Eq. 81 by numerical means is a fairly straightforward procedure. Here will only be presented the general methods and the results. Since the result is symmetric about the line of propagation of the disturbance the plasma response has only been calculated in two dimensions.

We will assume that the unperturbed distribution function is Maxwellian. The first task is to calculate the derivative of the plasma dispersion function. According to "The Plasma Dispersion Function"[25] we can write

$$Z(\gamma) = \frac{1}{\sqrt{\pi}} \int_2 \frac{e^{-y^2}}{y-\gamma} dy = \frac{1}{\sqrt{\pi}} \left[ \rho \int_{-\infty}^{\infty} \frac{e^{-y^2}}{y-\gamma} dy + i\pi e^{-\gamma^2} \right].$$

where the integration path runs below the pole. If  $\gamma$  is real (as is the case here) we may rewrite the integral in the following way:

$$\rho \int_{-\infty}^{\infty} \frac{e^{-y^2}}{y-\gamma} dy = -2\sqrt{\pi} e^{-\gamma^2} \int_0^{\gamma} e^{t^2} dt. \quad (82)$$

This in turn can be expanded as a series:

$$e^{-\gamma^2} \int_0^{\gamma} e^{t^2} dt = \frac{1}{2\gamma^2} \left[ 1 + \frac{1}{2\gamma^2} + \frac{3}{4\gamma^4} + \dots \right].$$

The calculation of this function which is called the *Dawson integral* can be performed by a library subroutine at the Ris VAX mainframe.

The calculation of the plasma response to a single ion introduced at  $(r, z, t) = (0, 0, 0)$  will then consist of the following steps:

- First the function  $h(\gamma)$  is calculated using the Dawson integral procedure. A table of  $h$ -values is constructed for a range of  $\gamma$ 's. This step only depends on  $Q$ .
- Then the second derivative of  $h$  is calculated. This is done by performing a *cubic spline interpolation* (see Appendix D) on the tabulated  $h$ -values and *differentiating numerically twice*. The results are saved in a table.
- The response for given values of  $r$  and  $z$  can now be calculated using Eq. 81. The integral is evaluated by constructing a table of the function to be integrated (using the table of  $h''$ ) and doing spline interpolation on this table. This can then be integrated analytically.
- $n(x, t)$  is calculated in a grid of points in the  $r, z$ -plane.

### Numerical results

The starting point for the calculation of the plasma response is the function  $h$ . The only parameter which enters this function is the temperature ratio  $Q$ . In Fig. 38  $h$  is shown as a function of the independent variable  $\xi$  together with its second derivative for three different values of  $Q$ . Note how  $h$  steepens and narrows with increasing  $Q$ .

The function  $h''$  is used for calculating the plasma response to a point charge. Here we would expect the response to depend qualitatively on the speed of the injected charge and the temperature ratio. More precisely, we should see radically different behaviour depending on whether the speed of the charge is below or above the ion sound speed,  $C_s$ . This is given by  $C_s = \sqrt{(\gamma_i T_i + \gamma_e T_e)/M_i} = \sqrt{(\gamma_i + Q\gamma_e)T_i}/M_i$ . Here,  $\gamma_{i,e}$  denotes the ratio of specific heats for the ions and electrons, respectively. At relevant  $v_0$ 's the electrons can be taken as isothermal while the ion response is adiabatic, i.e.  $\gamma_e = 1$  and  $\gamma_i = 3$  (see [26]). The calculated results of the response to a point charge are shown in Figs. 39-41.

In Fig. 39 we see the plasma response (density perturbation) to a positive point charge introduced at  $t = 0$  at three different times after the injection. Here  $v_0/v_{ti} = 5$ , so the motion is supersonic. Note the "wavefronts" propagating at an angle away from the path of the moving charge. Note also the negative perturbation which follows the positive perturbation (the primary response to a positive charge).

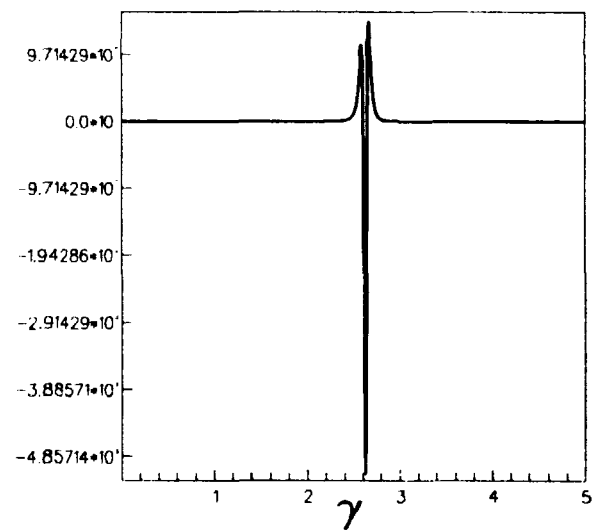
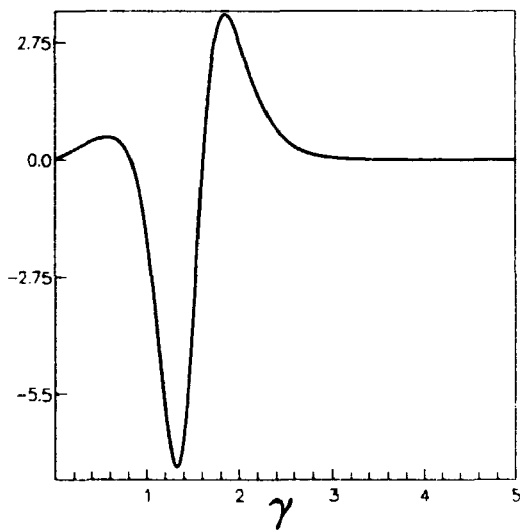
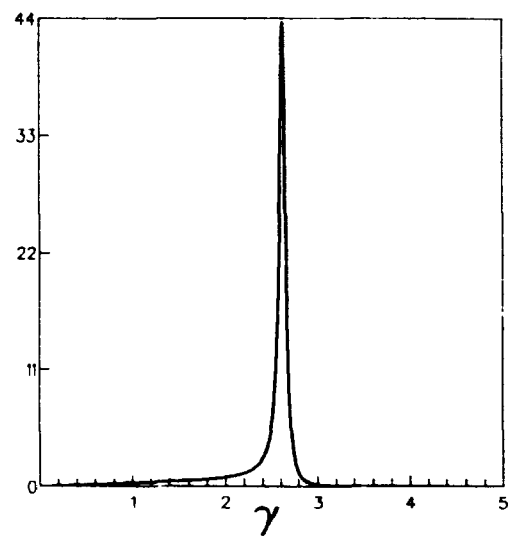
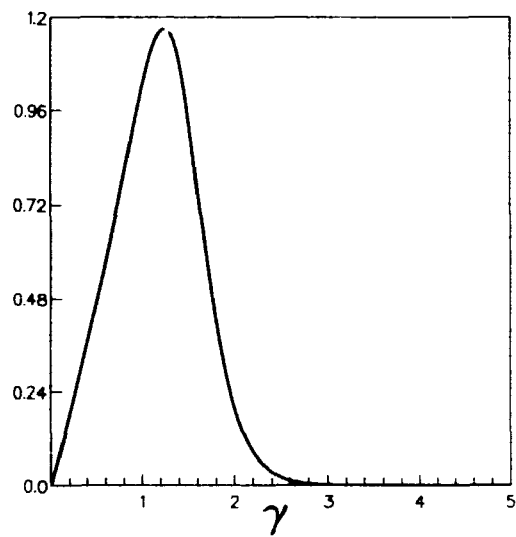


Figure 38. a) The function  $h(\gamma)$  at  $Q = 1$ , b) at  $Q = 10$ . c)  $h''(\gamma)$  at  $Q = 1$ , d) at  $Q = 10$ .



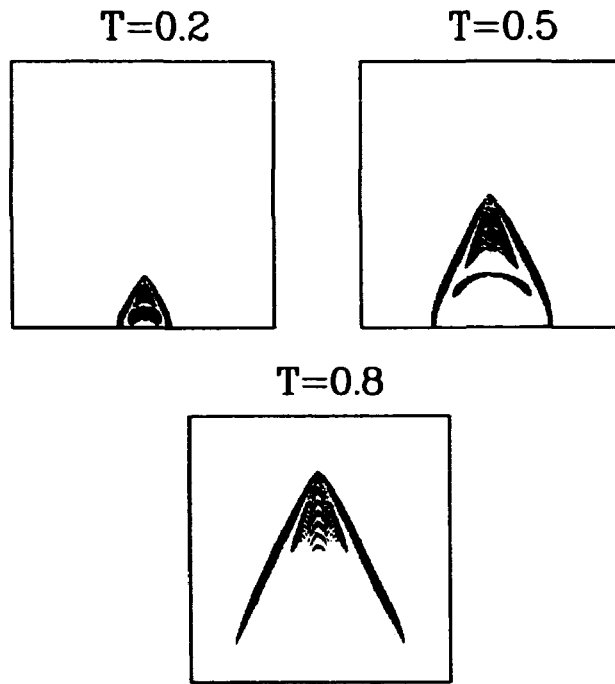


Figure 39. Plasma response to a point charge injected at  $(r, z) = (0, 0)$  and the time  $t = 0$ , calculated for three later times. Here  $Q = 5$  and  $v_{in}/v_{ti} = 5$ . Areas of positive charge are black, negative areas are grey in this and the following figures.

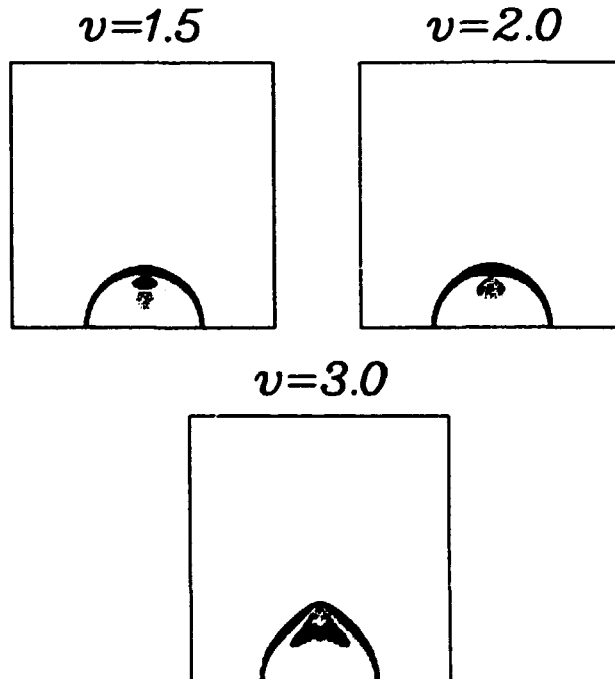


Figure 40. Plasma response to a point charge for three different injection speeds.  $Q = 5$  in all plots, whereby  $C_s \approx 2.83v_{ti}$ .

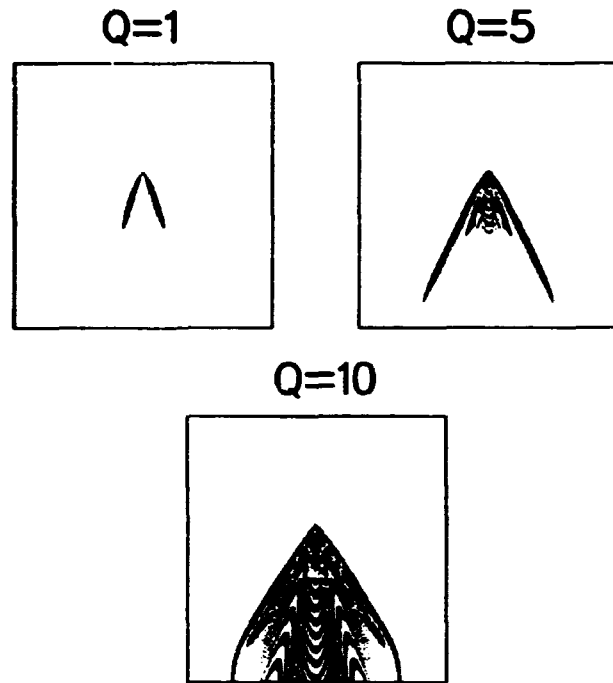


Figure 41. Plasma response to a point charge for three different values of  $Q$ .  
 $v_{i1} = 5v_{t1}$  in all plots.

In Fig. 40 is shown the response for three different injection speeds. In the first two frames  $v_{i1} < C_s$  while in the third the speed is supersonic. This is clearly seen from the figures. At subsonic speeds a semicircular perturbation propagates from origo ahead of the moving charge and the perturbation around the injected charge is more or less circular (less at increasing speeds). At supersonic speeds two almost plane "wavefronts" appear. These must travel at  $C_s$  and so must form an angle  $\theta$  with the normal to the trajectory of the charge given by  $\cos \theta = C_s/v_{i1}$ . This is analogous to the Čerenkov radiation known from high energy physics.

The plasma response depends strongly on the temperature ratio,  $Q$ . This is seen in Fig. 41. At low values of  $Q$  the perturbation is quickly damped while at high  $Q$  the ripples created by the perturbation propagate with hardly any attenuation. This is consistent with the fact that Landau damping exhibits the strongest damping of low-frequency waves when  $T_e$  is low. Note that in the last frame in Fig. 41 some of the ripples behind the moving charge may be an artefact of the calculation. The reason for this is the very sharp spike of  $h''$  (see Fig. 38). A small error in the calculation of the argument for this function could change the result drastically.

If we want to calculate the plasma response to a moving charge distribution this can be done by simple superposition. Of course this will only produce meaningful results (i.e. relevant to experimental results) if the charge distribution is so dilute that it does not affect the trajectories of its constituents. In this case the response to a spatial distribution of point charges moving at uniform velocity can be calculated simply by calculating the response to a single charge and adding the response itself shifted in space. This has been done in Fig. 42. Here is shown the response to a disc-shaped distribution of ions. The disc is orientated perpendic-

T=0.5

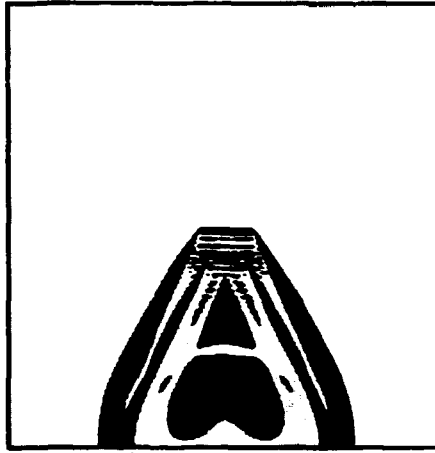


Figure 42. Plasma response to disc of ions injected at  $(r, z, t) = (0, 0, 0)$  at the time  $t = 0.5$ . Here  $v_i = 5v_{ti}$  and  $Q = 5$ .

ular to the plane of the figure and is moving in this plane. The relevance of this example to experiment will become clear in the next section.

### 4.3 Briefly on the ion beam instability.

In the previous section the plasma response to a very low intensity beam was discussed. Under those circumstances the plasma response can be calculated analytically using linear theory. If we now move to larger beam intensities we encounter the *beam instability*. An accurate solution of the plasma response in this case would require the use of the full nonlinear Vlasov equation. This is not a feasible undertaking, so in the following I will restrict myself to discuss briefly the dispersion relation for unstable waves in a two-stream plasma.

The starting point is again the linearised Vlasov equation, Eq. 61 and Poisson's equation, Eq. 62. In this case, however, we will not require quasineutrality. Then Eq. 62 becomes when transformed:

$$-k^2\phi = \frac{e(n_e - n_i)}{\epsilon_0} \quad (83)$$

and Eq. 63 becomes:

$$n_i = \int f dv \simeq \frac{e}{T_e} \phi + \frac{\epsilon_0 k^2}{n_0 e} \phi.$$

When transformed, the Vlasov equation looks like this:

$$(-i\omega + ik)f = \frac{e}{M_i} ik\phi f_0(v) + g(k, v) \quad (84)$$

where  $g(k, v)$  is the transform of  $f(x, v, t = 0)$ . Proceeding as in the previous section we obtain for  $\phi(k, \omega)$ :

$$\phi(k, \omega) = \frac{-i \frac{T_e}{n_e} \int \frac{g(k, r)}{v - \frac{\omega}{k}} dr}{1 + \lambda_d^2 k^2 - \frac{T_e}{n_e M_i} \int \frac{f_0'(v)}{v - \frac{\omega}{k}} dv} \quad (85)$$

with  $\lambda_d = \sqrt{\epsilon_0 T_e / n_0 e^2}$  being the Debye length. The denominator of Eq. 85 is the plasma dielectric function  $\epsilon(k, \omega)$  [27]. The dispersion relation for small scale oscillations is given by

$$\epsilon(k, \omega) = 1 + k^2 \lambda_d^2 - \frac{T_e}{n_e M_i} \int \frac{f_0'(v)}{v - \frac{\omega}{k}} dv = 0 \quad (86)$$

where the integration runs below the pole in  $v = \omega/k$ .

A calculation of stability requirements for the dispersion relation is performed in App. C. It is shown there that if  $f_i(v)$  is a Maxwellian the dispersion relation will only have damped solutions. But if the distribution function has more than one maximum the dispersion relation may have growing solutions. If the distribution function is a sum of two drifting Maxwellians, each with drift velocity  $v_j$ , the dispersion relation can be written as

$$1 + (\lambda_d k)^2 - \frac{T_r}{2T_i} \sum_{j=1}^2 n_j Z' \left[ \left( \frac{\omega}{k} - v_j \right) \sqrt{\frac{M_i}{2T_i}} \right] = 0 \quad (87)$$

where the  $n_j$ 's are the relative densities of the two ion components,  $n_1 + n_2 = 1$ .

The stability criterion can be calculated in a way similar to that of appendix C. It will be found that the stability of the beam-plasma system depends strongly on  $Q$  and  $v_j$ . For low  $Q$ -values there is strong Landau damping and thus no instability. Similarly, if  $v_j$  becomes too large the instability is not excited.

From Eq. 86 the general dispersion relation for low frequency modes can be calculated. This requires the use of the complex plasma dispersion function which may be found tabulated[25] or can be calculated numerically. In Fig. 43 is shown the dispersion relation for a set of parameters relevant to the experiments in the DP-machine. The dispersion relation is calculated both for the background plasma alone and for a plasma with an ion beam.

In the background plasma there is one low-frequency mode, the ion acoustic mode. However, in the ion beam plasma two different modes may be excited. That this is so may be easily seen when considering the beam in its reference frame. There will then be one ion acoustic mode running forward and one running backward. But in the laboratory frame both these modes will propagate in the direction of the beam. It is furthermore seen that the slow mode is unstable for these parameters whereas the fast mode is weakly damped. The background ion acoustic wave is strongly damped at high frequencies (Landau damping again).

The above calculations were all done using the one-dimensional Vlasov equation. In reality the ion beam introduces an anisotropy into the calculations and the modes behave differently along the beam and in the radial direction. I will not here try to perform calculations on this problem but only briefly relate some numerical results obtained by various workers, e.g. Doveil and Grésillon[28] and Johnsen[29]. They found that at low beam velocities (less than about  $1.5v_{ti}$ ) the unstable modes are propagating almost parallel to the beam. At greater beam velocities oblique modes become unstable and at  $v_b > 2v_{ti}$  the oblique modes dominate.

These results assume a uniform three-component plasma (ions, electrons and beam ions). If the beam is of finite diameter these results may need modification. This, however, is a major undertaking and will not be attempted here.

## 4.4 Experiments on the DP-machine

### Experimental set-up

Experiments on ion acoustic waves and the beam instability requires a largely unmagnetized plasma, preferably without DC-currents, which may disturb the plasma stability properties. These requirements are fulfilled in a *Double Plasma (DP) machine*. A schematic diagram of the Ris DP machine is shown in Fig. 44a. The DP machine consists of a cylindrical vacuum chamber of height 110 cm and

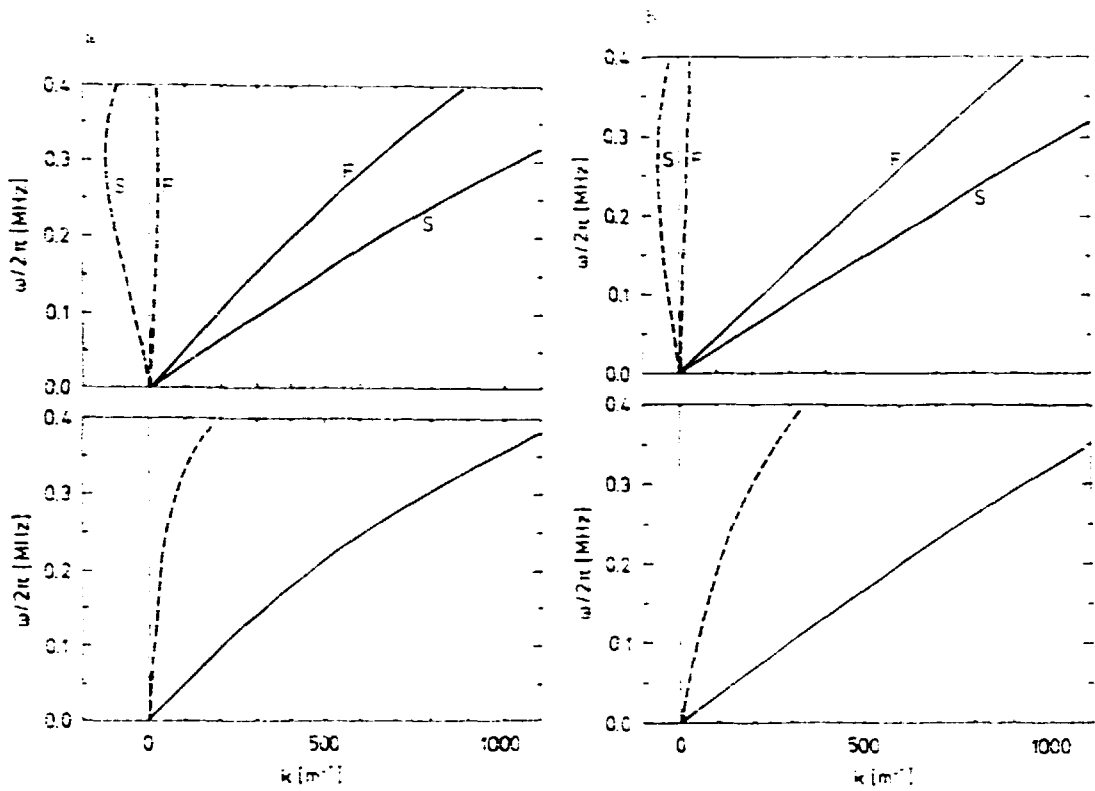


Figure 43. Dispersion relation for the ion acoustic modes. Upper figures show the fast and slow beam modes, lower figures the plasma mode when the beam is not present. Solid lines show the real part, dashed lines the imaginary part of  $\omega$ . Plasma parameters are:  $T_{ib}/T_{ii} = 0.05$ ,  $v_b = 5v_{th}$ ,  $n_b/n_0 = 0.05$ ,  $n_0 = 10^{11} \text{ m}^{-3}$ . In a)  $Q = T_r/T_i = 15$ , in b)  $Q = 5$ .

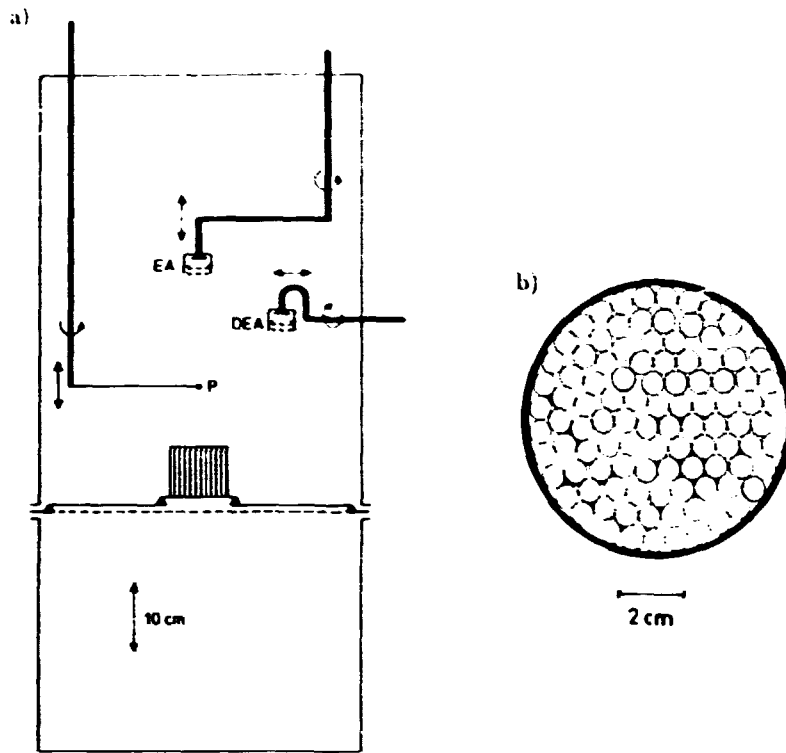


Figure 44. a) Schematic drawing of the experiment. b) The "chimney" used for collimating the beam.

diameter 50 cm. The chamber is divided into two parts separated by a metal plate with a central hole of diameter 10 cm. The two chambers may be electrically biased relative to each other. Along the sides of both chambers are placed rows of glow filaments (not shown in the figure) which may be heated to emit electrons. The filaments may be biased relative to the walls of the chambers (normally  $\sim 40V$ ). The resulting current ionizes the gas in the chambers to produce a plasma. Argon gas has been used in these experiments, at neutral pressures of  $4 \cdot 10^{-5}$ – $1 \cdot 10^{-1}$  mbar. Both chambers may be fitted on the outside with arrays of small permanent magnets to improve plasma confinement near the wall.

Between the two chambers is placed a metal mesh which is biased at a high negative potential ( $\sim -80V$ ). This is to ensure that electrons do not pass from one chamber to the other. Ions however, may travel freely from one to the other. If the two chambers are at different potentials an ion beam will pass between the chambers through the hole in the dividing wall. In our experiment the lower chamber (the *driver* chamber) is always at a higher potential than the upper (the *target* chamber).

The machine is similar in structure to most other DP machines (see e.g. [30, 31]). The main new feature is the metal plate which separates the two chambers. This allows a beam of finite width to be injected into the target plasma where in normal DP machines the beam extends to the walls.

Diagnostics are placed in the target chamber. These are of two types. First there are two energy analysers. These are similar to the ones used by Andersen et al. [32] except that a second mesh has been added in front of the analyzer. This is biased at a high negative level ( $\sim -60V$ ) to repel the fast (non-thermal) electrons which may be present in the DP machine. One energy analyser enters from the top of the

machine (see the figure) and may be moved across the ion beam as well as along it. The other is inserted through the side of the machine. It can only be placed at a few fixed vertical positions but may be rotated at an angle to the beam.

The other type of diagnostic is a plane Langmuir probe of diameter 5mm. This too can be moved along and across the beam.

#### Collimating the beam

In order to study the propagation of ion acoustic waves inside and outside the beam it is important to know precisely the radial extent of the beam. However, the beam ions may be deflected by the strong electrical fields in the vicinity of the mesh separating the two chambers. To ensure that the ions are unidirectional we have used various collimators in front of the hole between the chambers. An example of these collimators is shown in Fig. 44b. It consists of a metal cylinder of diameter 80mm and height 50mm. The cylinder is filled with thin-walled metal tubes of diameter 8mm. (These dimensions vary between the different collimators.) This will ensure that the beam is completely collimated within an angle of  $9^\circ$  and almost entirely collimated within  $5^\circ$ . The collimator can be raised above the bottom plate. This helps electrons to enter the collimator and neutralise space charges.

An analogous system is used to enhance the directional sensitivity of the energy analysers. Here the first grid is replaced with a brass plate of thickness 2.5mm. In this has been drilled a large number of holes with diameter 0.4mm. This allows only ions impinging at an angle of  $< 9^\circ$  to enter the analyser. The transparency of this collimator is about 50%.

#### Plasma and beam characteristics.

Basic plasma parameters were measured in fairly standard ways. The electron temperature,  $T_e$ , was inferred from the ion acoustic sound speed,  $C_s$ .  $C_s$  was measured in the background by exciting ion acoustic waves of known frequency and measuring the wavelength. From this  $T_e$  can be calculated using the assumption (valid in this type of plasma)  $T_i \ll T_e$ . We found  $T_e = 2.2\text{eV}$ .  $T_i$  was not measured directly but it is known that in DP-machines  $T_i \sim 0.1T_e$ .

The plasma density was measured by the Langmuir probe, from the ion saturation current. The value depends on the parameters of the plasma discharge (notably the current from the filaments to the wall) but is normally around  $10^{14}\text{m}^{-3}$ .

By applying a voltage difference (positive at the driver) between the two chambers a beam is injected into the target chamber. The beam profile in the target chamber is shown in Figs. 45&46 for two different beam intensities, measured from the analyser characteristic. In these two examples the collimator was not mounted.

From these figures we note several features. In Fig. 45 the beam widens as it propagates in the background plasma, while in Fig. 46 the beam does not widen perceptibly. This is consistent with the fact that in the first case the beam is much stronger than in the second, in fact the beam density is almost comparable to the background density. The widening is due to repulsion by the electrical field caused by excess space charge.

The beam profile at the opening is somewhat peculiar in the strong beam case, with a central dip in beam density. This is thought to be caused by edge effects near the hole between the chambers where electrical fields are very strong. The same phenomenon is seen when the collimator is used.

As the beam propagates through the plasma it is strongly attenuated. This is due to charge exchange collisions with the neutral background gas. The attenuation

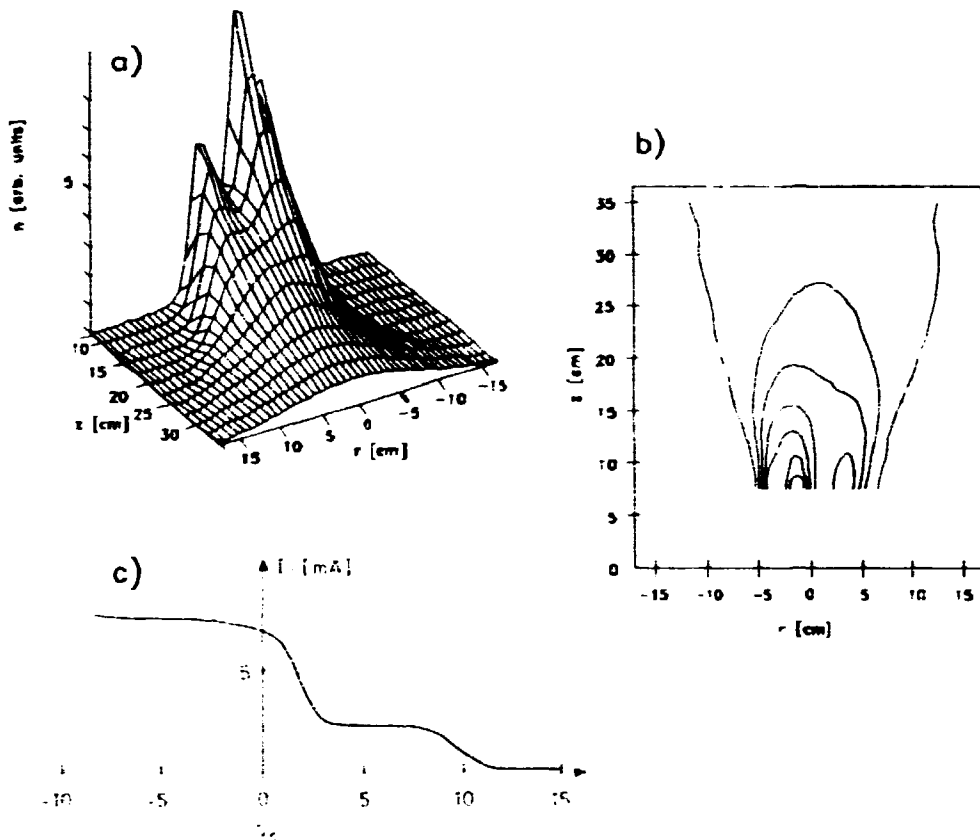


**Figure 45.** a) & b) Propagation of the beam in the target chamber from 0 to 400 mm above the dividing plate.  $E_b = 12eV$ . c) Energy analyser characteristic for this beam, taken at  $r = 0$  and  $z = 70$ mm.



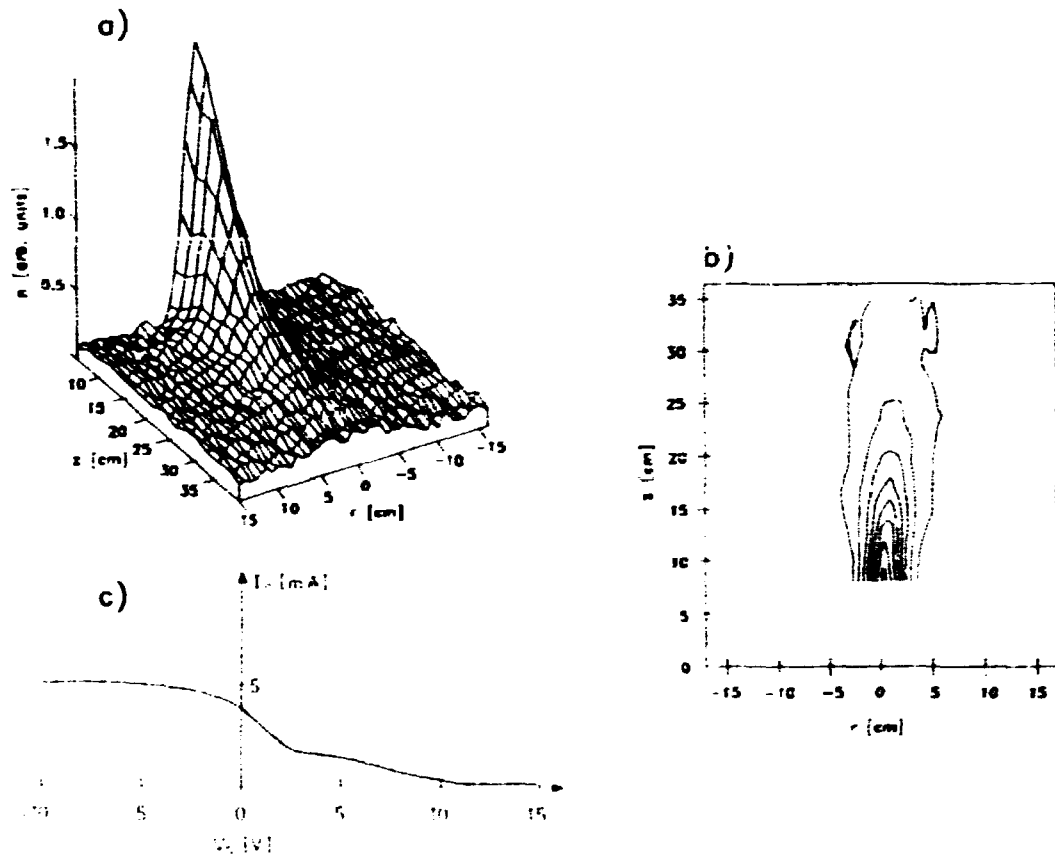


Figure 46. Beam profile as in the previous figure, but for a beam much weaker relative to the background plasma.

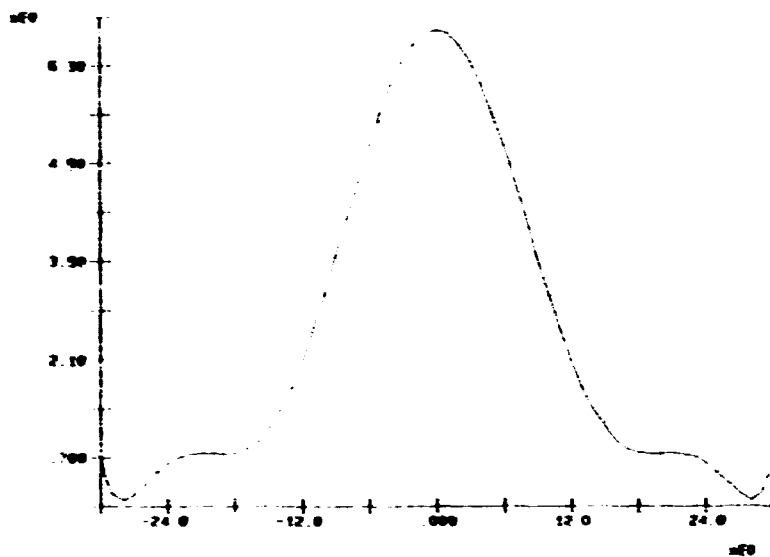


Figure 47. Signal to directional analyser as a function of impinging angle. The cut-off for a completely unidirectional beam is at  $9^\circ$ .  $E_b = 30\text{eV}$ .

therefore depends on the background pressure. Here it should be noted that in this experiment the collision cross section is larger than the standard value as given by e.g. Hegerberg et al. [33]. The reason is that a fairly large part of the background gas is in an excited state and thus the cross section is larger.

When the collimator is used, it is found, somewhat surprisingly, that the beam is strongly attenuated (more than an order of magnitude). The cause is not entirely clear but is thought to be spurious electrical fields between the separating grid and the collimator which deflect the beam ions. The situation is somewhat ameliorated by raising the collimator above the bottom plate (see Fig. 44). The strong attenuation limits the usefulness of the collimator for some purposes which require strong beams. On the other hand it may serve as an efficient attenuator.

Ions passing through the separating grid will be deflected in a random fashion. This will increase the radial beam temperature. An estimate of this can be found by the directional analyser. Placing this in the middle of the beam we measure the beam intensity as a function of the angle of incidence. The result is shown in Fig. 47. It is seen that there is a definite signal beyond the cut-off at  $9^\circ$ , so the ions are not unidirectional. From the curve we find a radial temperature of  $0.8\text{eV}$ .

#### Experiments with a weak modulated beam.

By perturbing a weak beam we may investigate the propagation of this perturbation inside and outside the beam. In our experiments the perturbations were of two kinds:

- A sinusoidal signal applied to an otherwise steady-state beam. This will excite the ion acoustic modes in the beam.
- A short pulse of ions (with no steady-state beam) injected into the target chamber.

The propagation of the perturbation is measured by the Langmuir probe, measuring the AC value of the electron saturation current. This is then multiplied with the original signal and averaged, using a lock-in amplifier. This analog method is fast enough that a two-dimensional picture of the perturbation can be obtained in a reasonable time.

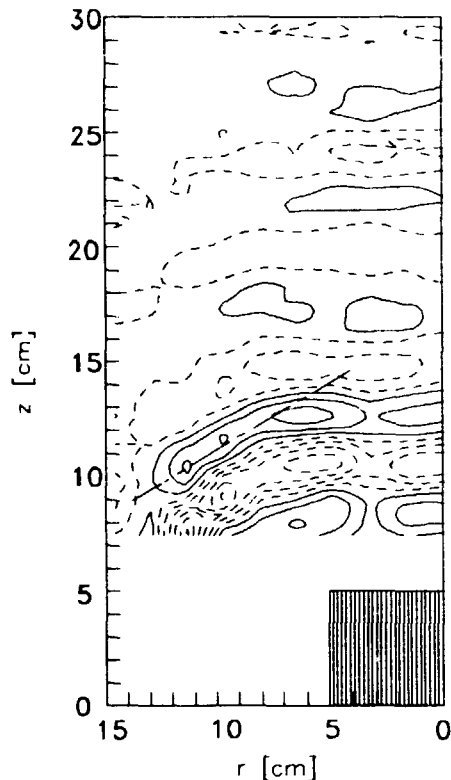


Figure 48. Ion sound wave propagation inside and outside the beam. The collimator is shown in the lower right corner of the figure. Here  $E_b = 5$  eV,  $f = 100$  kHz. Only one half of the experiment is shown in the figure. The dashed line indicates the angle at which the waves propagate outside the beam.

### Wave propagation

In this series of experiments a weak, i.e.  $eV_{p-p} \ll E_b$ , sinusoidal signal was superimposed on the DC-voltage between the driver and target chambers. Thus the two beam acoustic modes (see Fig. 43) were excited. If the frequency is sufficiently low (much lower than the ion plasma frequency at  $\omega_{pi}/2\pi = \sqrt{ne^2/\epsilon_0 M_i}/2\pi \approx 350$  kHz) this should then couple to the ion acoustic mode in the background plasma.

In Fig. 48 is shown one measurement of the propagation of the wave inside and outside the beam, shown as a contour plot of the probe signal and the reference signal multiplied and averaged in time. Wavefronts are clearly seen to be perpendicular to the beam inside the beam and to propagate at an angle to the beam in the background plasma. From plots of this kind the bending angle at the interface can be found as a function of the beam velocity.

This function is plotted in Fig. 49. The solid curve indicates the theoretical values given by  $\cos \theta = C_s/v_b$  (the simple law of diffraction in two media with different propagation speeds).

The experimental results are in qualitative agreement with the expectations but show clear deviations quantitatively. Various explanations for this can be found:

At subsonic speeds the theoretical curve does not apply as the wavefronts will here be semicircular outside the beam (see Fig. 40). But in the experimental results

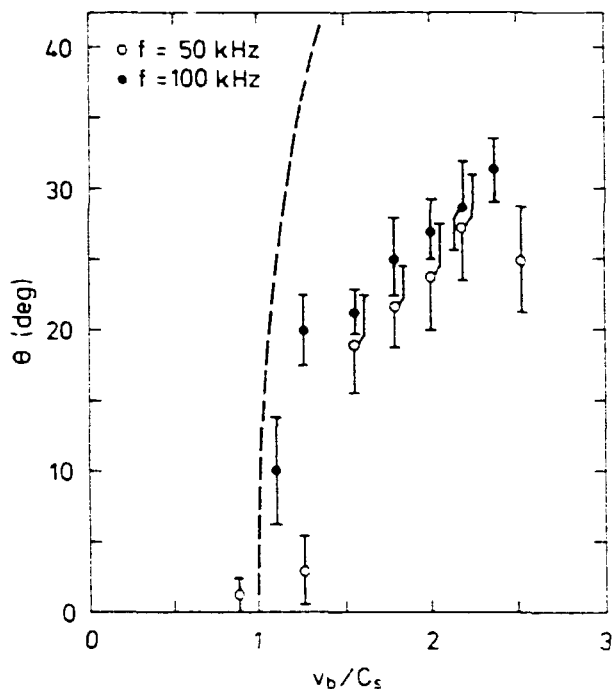


Figure 49. The angle  $\theta$  at which the sound waves propagate outside the beam, as a function of  $\sqrt{E_b} \propto v_b$ .

the wavefronts do not bend at sharp angles at the beam boundary. Thus the semicircular wavefronts at subsonic speeds may have been mistakenly interpreted as a bending angle.

At supersonic speeds the observed angle is consistently smaller than the one predicted by theory. One explanation could be that the beam is not exactly monoenergetic. This would blur the sharp bending of the wavefront. However, the beam temperature is not nearly high enough to explain the discrepancies. A better explanation may be that the plasma electrons have a small component which is much hotter than the bulk of the electrons. This will lead to a higher  $C_s$  in the background plasma and hence to a smaller bending angle.

As was mentioned in section 4.4 the bottom plate of the target plate (and hence the collimator) can be biased independently. In all the experiments described above the bottom plate was at ground potential (as is the target chamber). If the bottom plate is biased at the same potential as the separating grid (i.e.  $\sim -80V$ ) the picture is quite different. In Fig. 50 is shown the wave propagation in this case.

It is seen clearly that the waves do not propagate outside the beam. The reason is thought to be the following: The ions in the background are attracted by the negative potential of the bottom plate and thus obtain a net downwards drift. This will cause the plasma ion acoustic mode in Fig. 43 to be rotated around origin in the negative direction. It will then become more difficult for the beam modes to couple to the plasma mode.

#### Plasma response to a short pulse of fast ions.

In these experiments the DC voltage between the driver and target chamber was set to 0V. By applying a short ( $\sim 10\mu s$ ) voltage pulse between the chambers a bunch of ions was injected into the target chamber. The plasma response to this disturbance can be traced by correlating the signal to the Langmuir probe with

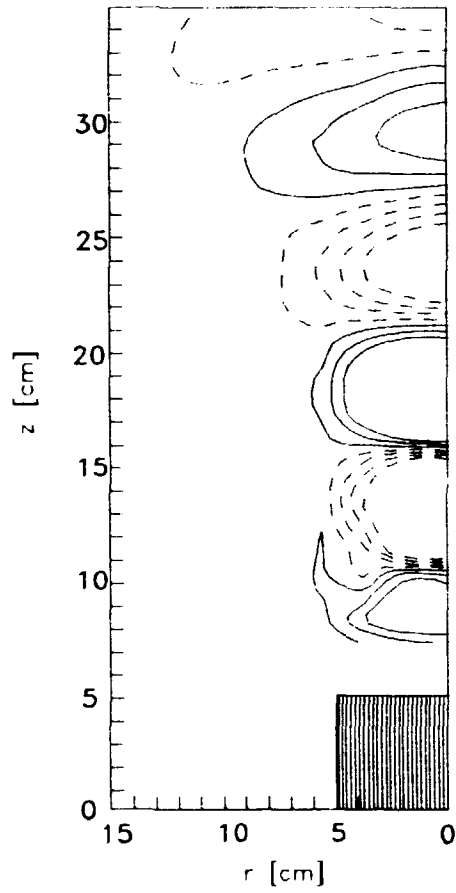


*Figure 50. Ion sound wave propagation in the target chamber when the bottom plate is biased at  $-80\text{ V}$  relative to the target chamber. The waves do not propagate outside the beam.  $E_b = 5\text{ eV}$ ,  $f = 50\text{ kHz}$ . Only one half of the experiment is shown in the figure.*

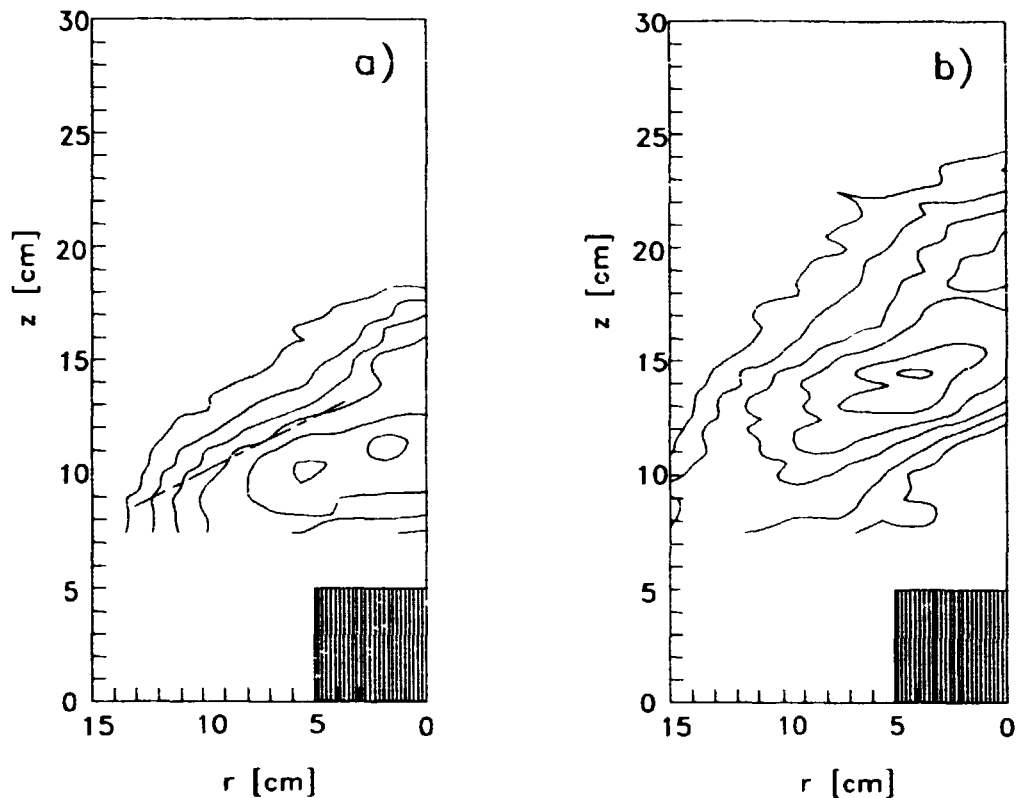


*Figure 51. Plasma response to a pulse of supersonic ions of duration  $10\mu s$  at different times after injection. In a)  $t = 35\mu s$ , in b)  $t = 45\mu s$  after the start of the pulse. The pulse energy  $E_b = 5eV$ . Only one half of the experiment is shown in the figure. Again, the dashed line indicates the angle at which the waves propagate outside the beam.*

the applied voltage pulse  $V(t)$ , i.e.

$$\bar{n}(r, z, \tau) = \int \bar{n}(r, z, t + \tau) V(t) dt. \quad (88)$$

The multiplication and time integration is performed with a boxcar averager. By varying  $\tau$  the time evolution of the plasma response can be obtained. This is shown in Fig. 51 for two different values of  $\tau$ . It is clearly seen that the perturbation propagates along the  $z$ -axis.

These measurements are somewhat distorted by noise but still it is possible to see a resemblance to the numerically calculated results in Figs. 39-42.

It is seen from Fig. 51 that the plasma is perturbed both inside the path of the pulse of ions and outside. Since the ions in the pulse are supersonic the perturbation propagates slower than the pulse and hence at an angle outside the path. This angle depends on the pulse energy as is seen in Fig. 52. As in the wave propagation the measured angles are consistently smaller than predicted values.

#### **Experimental investigations of the ion beam instability. Preliminary results.**

The experimental results to be described here are only a preliminary investigation of the turbulence due to the ion beam instability. Most of this work has also been done by other authors, [29][34][35]. The main new feature of this work is the finite width of the ion beam which gives rise to some special effects.

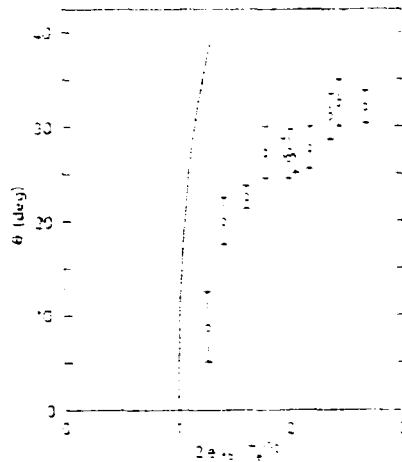


Figure 52. The angle  $\theta$  at which the disturbance due to a pulse of ions propagates outside the beam, as a function of  $\sqrt{E_b} \propto v_b$ .

For this experiment the collimator was not used as it attenuates the beam too strongly. Without the collimator the beam density can become comparable to the background plasma density as is shown in Fig. 45. At this beam density the ion beam instability is excited provided the beam energy is not too high.

By applying a standard spectrum analyzer to the signal from the Langmuir probe the frequency spectrum of the noise generated by the instability can be obtained. This is shown in Fig. 53 at various points in the target chamber.

In Fig. 53a we show the noise spectra in the middle of the beam ( $r = 0$ ) at various distances  $z$  from the orifice. It is seen that the instability grows in the time it takes the ions to reach a position about 7 cm into the target plasma. At a beam voltage of 12V this gives a growth time of  $\sim 10\mu s$ . At higher positions the noise level diminishes again due to the attenuation of the beam, see Figs. 45 and 46. A conspicuous feature of the noise spectra is their double-humped form. Most earlier investigations with ion beams filling the entire experiment [36] showed spectra with a single broad peak (one exception may be the results of Taylor and Coroniti[34]). Since the main difference in our experiment is the finite width of the ion beam, we expect that the second hump is due to radial modes in the beam, which are excited at beam velocities  $v_b > C_s$ , as is the case in this experiment [37]. These modes propagate across the beam and are partially reflected at the edges because of the change in refractive index at the edge. The second (high frequency) hump disappears further into the background plasma as the beam becomes weaker.

In Fig. 53b & c we show spectra at different radial positions at  $z = 8\text{cm}$  and  $z = 17\text{cm}$ , respectively. It is seen that the noise level diminishes when we move from the center of the beam towards the edge. At the same time the spectrum changes qualitatively. This too may be due to the partial reflection at the beam edge. It is also seen that the noise does not disappear entirely at the edge of the beam. This shows that the noise generated inside the beam propagates in the radial direction out of the beam.

A more detailed investigation of the turbulence caused by the instability will be the subject of future studies. This will introduce two-point correlation methods similar to those described in chapter 2 to determine the propagation of structures in the turbulence.

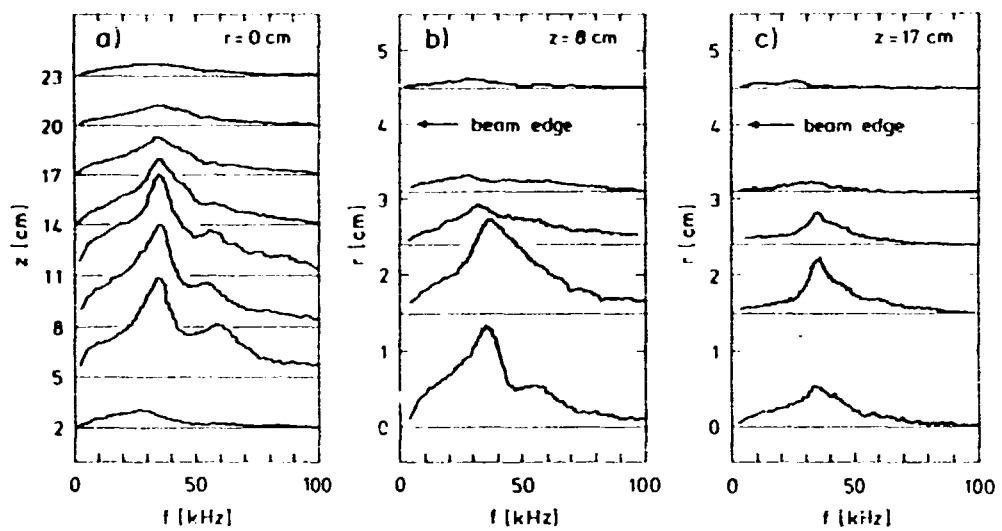


**Figure 53.** Spectra of the noise due to the beam instability. a) Spectra taken in the middle of the beam at various distances from the orifice. b & c) Spectra for different radial positions at positions  $z = 8\text{ cm}$  and  $z = 17\text{ cm}$  above the orifice.



## 5 The AIDA data acquisition and display system.

### 5.1 Introduction

The Advanced Interactive Data Acquisition program is a collection of routines written in ASYST to facilitate the acquisition and plotting of measurements from the Q- and DP-machines of the Plasma Physics Section. Here it has been used extensively and some of the data from the Q-machine and all the data from the DP-machine presented in the previous chapters have been acquired with this program.

The system has been designed to enable the user to perform data acquisition operations without any deep knowledge of the hardware or of programming in ASYST.

AIDA runs on an IBM PC or compatible using the ASYST software tools (version 2.0 or later). It also requires one of the A/D plug-in boards for the PC which is supported by ASYST. Our set-up consists of an Olivetti M380/XP5 PC-compatible computer with a hard disk, expanded memory, and a floating point co-processor, a matrix printer and a Hewlett-Packard 7475 graphics plotter. The A/D-board is an Analog Devices 2818, with 4 A/D channels, two D/A channels and  $2 \times 8$  digital input/output channels. The A/D-board is connected to a couple of custom-built motor control boxes, which can control two stepper motors and two DC motors.

### 5.2 General structure of AIDA

The goal set for the development of AIDA was to make it easy for the user to perform a wide variety of data acquisition sessions without programming (on the user's part) and to display the data thus obtained. It should be possible to use the program with many different experimental set-ups and make the measurements in many different ways. To make the program easy to use it has been made *menu-driven* to a high degree and to make it generally applicable the concept of the *Measurement Type* was introduced. The structure of the source code generally reflects the structure of the program as revealed through the menus, so in the following I will more or less go through the program menu by menu.

When first entering AIDA from the ASYST environment you are presented with a menu as the one in Fig. 54.

This corresponds well to the physical structure of the program as seen in Fig. 55. As you can see, AIDA consists of a main part and three general subparts which correspond to the various options in the main menu. The main part consists of initialisation routines, the main menu, and some general routines that are used by more than one of the subparts. This part of the program has been *SAVED* in a customized version of ASYST called AIDA and thus these routines are always available. The subparts have each been stored in one or more *overlay files* (see [39, p. 1.10 ff.]). These overlay files can be loaded into ASYST by the main program and the Words (subprograms in ASYST are called Words) in them can then be accessed. However, they cannot be active all at the same time. Therefore there are sometimes some overlapping between the routines in the various overlays. We will have a look at each of these parts in turn, but first I will take a look at the concept of the *Measurement Type*.

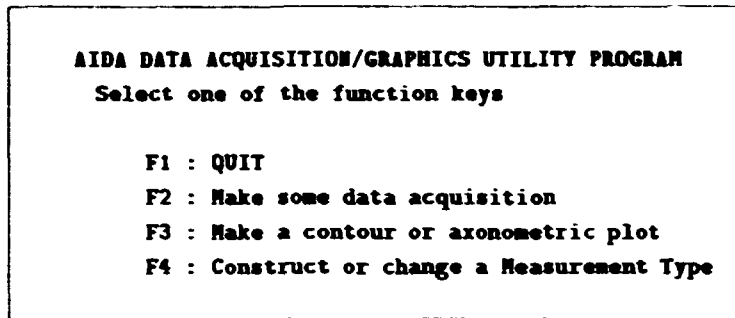


Figure 54. The main menu in AIDA

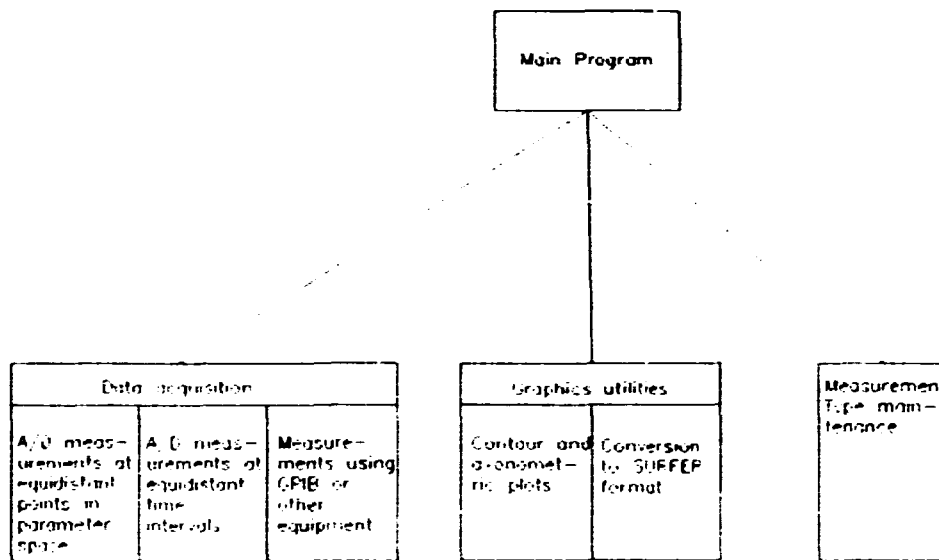


Figure 55. Top level structure of AIDA. Each box in the subprograms corresponds to an overlay file.

### 5.3 Measurement Types

The term *Measurement Type* denotes a set of information which makes it easy to perform a series of identical or nearly identical data acquisition sessions. This information may be about the shape of the acquired data, when to make a measurement, or general parameters for the experiment. The information in the Measurement Type is also used by the graphics part of AIDA to find the relevant data in the data files and determine the parameters for the plot. Each Measurement Type has a specific name of not more than 12 characters and an abbreviation 2 characters long. This name is used by the user to find the relevant information for the data acquisition session. The abbreviation is among other things used for naming the data files where the acquired data are stored. The name of a data file made with AIDA is `NNddmmyy.XXX`, where `NN` is the abbreviation name, followed by the date the acquisition was made. `XXX` is the number of the data file acquired that day using the given Measurement Type.

The information making up a Measurement Type is stored in two files. One is an `ASYST` file called `DEFAULT.NN` and the other an `ASCII` file called `QUESTION.NN` where again `NN` denotes the abbreviation name of the Measurement Type. `DEFAULT.NN`

contains a single array of 50 real numbers (this number can be changed, of course). The numbers in the DEFAULT.HH file contain the following information:

**Nos. 1-20** Default values of parameters for the data acquisition session. These can be parameters that are essential for the proper execution of the session, e.g. the number of measurement points, or they can be general parameters for the experiment that have no influence on the acquisition session. These values are set by the user in the beginning of each session (see sec. 5.4). They are also stored in the comments of the data file created in the session. Some of these parameters must occupy fixed places in the list, whereas others may be placed randomly. Not all 20 places need be used.

**Nos. 21-28** These numbers are conversion factors between the integer values output by the A/D-converter and the real values of the quantities measured by the A/D-channels. Two numbers are required for each channel, a conversion factor and an offset value, and so there is room here for four channels.

**Nos. 29-42** These numbers are specific to the current Measurement Type but are not normally changed between sessions using the same Measurement Type. The information stored here includes items such as the number of A/D-channels used in these sessions, the number of comments in the data files, whether the sets of data are one- or two-dimensional etc..

**Nos. 43-50** are not currently used.

The exact contents of the DEFAULT.HH file for set-up used in the Plasma Physics Section is described in the AIDA Reference Manual ([44, App. B]).

The file QUESTION.HH is closely related to the first 20 numbers in the file DEFAULT.HH. This file contains the text for the questions which the user are given in the beginning of each data acquisition session and the corresponding comments which are put into the comment lines of the data file created during the session. The file is read one line at a time, so the questions and comments must be placed on separate lines with no empty lines between lines of text.

As was mentioned in the beginning of this section, the files resulting from a data acquisition session are named according to the date of the acquisition and the number of previous completed sessions on that day. Therefore we must have a place to store information on the number of times a given Measurement Type has been used today. This information has been stored in the file MEAS.TYP. This is an ASYST file which contains 100 comment lines and two arrays of length 100. The comment lines contain the names of the currently defined Measurement Types and the arrays contain for each entry in the comments the date of last access and the number of sessions made on this last date. This file is read by the data acquisition parts of AIDA and is updated by the subprogram that constructs or changes Measurement Types.

## 5.4 The data acquisition subprograms

### The basic classes of Measurement Types

Essentially, the task of the data acquisition part of AIDA is to control the flow of data from an A/D plug-in board to the computer memory and on to an ASYST data file. There are almost infinitely many ways of doing this and so it is important that the program makes it easy for the user to make exactly the type of measurement she wants. Indeed, a large part of the acquisition routines deal with

selecting the appropriate Measurement Type and finding the right parameters for the measuring session.

At present four basic classes of data acquisition sessions exist. They differ from each other in the organisation of the data and the way the time of measurement is determined. Determining the time of measurement can here be done in two ways:

1. The measurements can be made at equal time intervals.
2. The time of measurement can depend on some other measured quantity.

Here the present version of the program makes some constraints:

- The reference quantity determining the time of measurement must be measured by the first channel of the A/D-converter.
- The points of measurement must be at equidistant values of the reference quantity.
- The reference values must increase monotonically.

The program can of course be modified to remove these constraints.

In order to use the first class of measurements the A/D board must be able to be programmed to different acquisition frequencies. This is the case for the one we are using. The reference quantity for the second class may in principle be any measurable quantity that satisfies the constraints. It may be the position of a measuring probe, the temperature of the experiment etc..

In a sense the two classes are equivalent since the time could be measured by the reference channel and thus turn the second class into the first. However, there is an important difference. In the first class you may acquire data at a rate which is only limited by the type of A/D board you use. These boards normally work at rate from a few kHz to a few hundred kHz. But in the second class of measurements there is a large programming overhead and so the maximum speed here will be less than 100 Hz, even on the fastest PC's.

Each of these two different ways of making measurements can again be divided into two groups according to whether the grid of measuring points in phase space is one- or two-dimensional. In other words: each time you make a series of measurements depending either on time or some other quantity, you make a scan through the parameter space of your experiment. AIDA allows you to make either one scan and save the data in a separate file or to make several scans where some other quantity is changed between scans. The values of this quantity may or may not be equidistant and the value of this second quantity may or may not be monitored by an A/D-channel. Note here, that whether you make a one- or two-dimensional measurement you will get a set of data of this dimension from each of the A/D channels you use.

#### **General structure of the Acquisition routines.**

The routines for the two classes of Measurement Types are placed in separate overlay files (see Fig. 55). Since you may not load one overlay from another the highest level of these routines is part of the main system. This consists of among other things the acquisition menu shown in Fig 56.

Of the three options in the menu, the simplest is the listing of the available Measurement Types. The list of Measurement Types is stored in a text file which can be read with the ASYST editor. The routine called by option 3 simply calls the editor.

The data acquisition programs themselves are activated by the second option. The general lay-out of this part of the program is shown in Fig. 57.

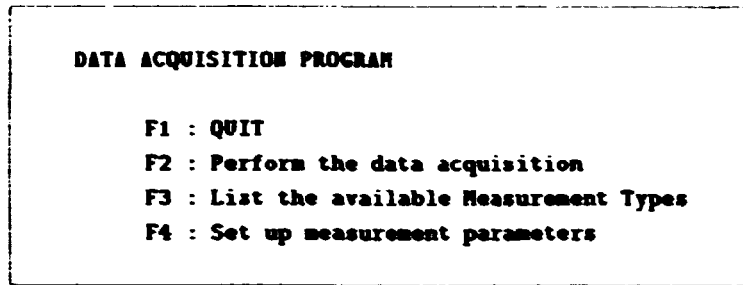


Figure 56. The menu for the data acquisition system.

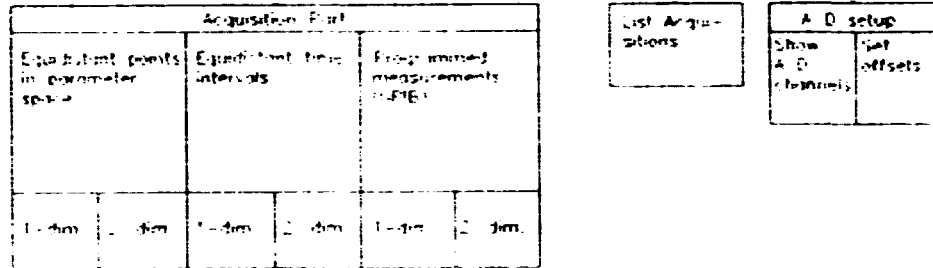
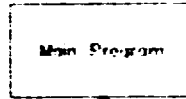


Figure 57. Structure of the data acquisition part of AIDA.

The very first thing this program does is to get the name of the Measurement Type from the user and then examine the DEFAULT.WW file to find which class of Measurement Type it is. This is necessary at the very start as the Words for the various classes are stored in two different overlays.

What happens next varies a little between the classes of Measurement Types. For two-dimensional measurements the user is asked whether the points in the second dimension in phase space are equidistant or not. This has some bearing on which questions the user will be asked next. For the next part is a series of questions about parameters for the session, arranged in a menu, where the user can browse through the menu using the cursor keys. Some of the parameters are essential for the measurement session, such as the number of data points.

When the parameters have been entered the program sets up some temporary arrays for storing the data as they are being acquired. The shape and size of the arrays vary with the Measurement Types and the entered parameters. The file for the data is also created at this time.

Now the program is ready to proceed with the actual data acquisition as soon

```
F1 : QUIT
F2 : Show values of A/D channels
F3 : Set offset and incremental values
```

*Figure 58. The acquisition setup menu.*

as the user is ready. The data acquisition process depends not only on the class of Measurement Type and the number of data points but also to what extent the experiment can be controlled by the program. If the program can control the value of the independent variable that is changing during a scan and the parameter changing between scans, then the entire data acquisition process can run without further help from the user. If the set-up is not automatic the program will stop at convenient points. Moreover, the user can at almost any time stop the acquisition to exit. In the case of two-dimensional measurements it is also possible to stop to see a plot of the last completed scan or to retake a number of scans.

When the acquisition has finished (or has been terminated prematurely) the user is asked whether to save the data. This is then done if wished. The data acquisition is now finished and the user may return to make another acquisition with the same Measurement Type or return to the data acquisition menu.

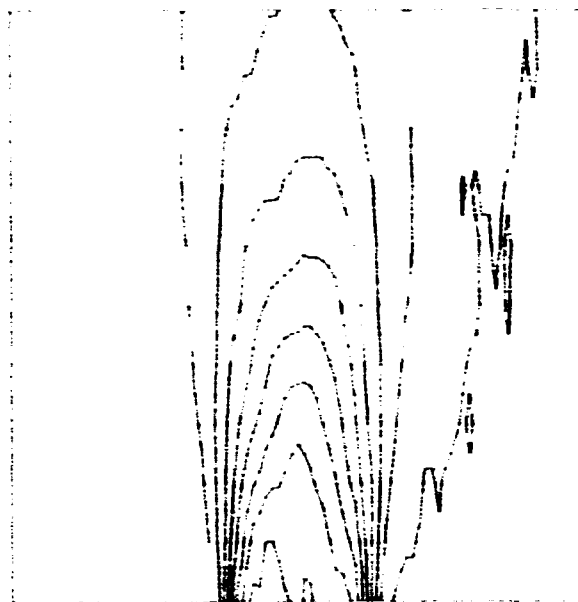
The fourth option in the data acquisition menu is a set of routines which calibrate the Measurement Type so that the values measured by the A/D converter will be converted into the actual physical values when a measurement is done. It will present you with yet another menu shown in fig 58.

The first option measures the voltage input to the A/D channels and shows the values output directly by the A/D channels. Hitting a key will give new values. This is useful for determining the relation between the physical quantities measured and the output from the A/D board. This knowledge is necessary for the second option in the menu. For a chosen A/D channel it asks you for two physical values and the corresponding output from the A/D. Thus the program can calculate the general relation (assuming that it is linear) and output the proper physical values to the data file when making a measurement.

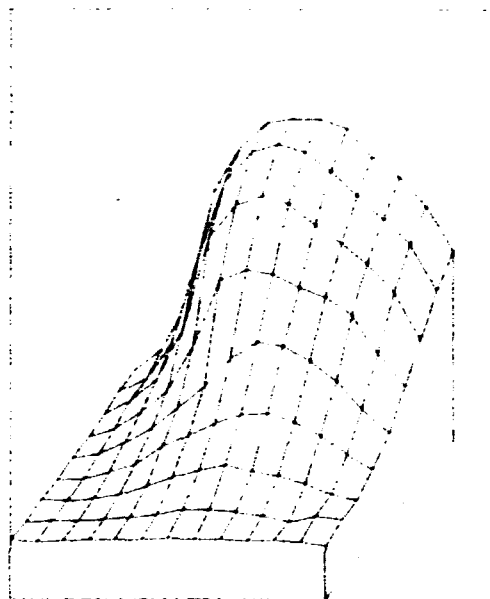
## 5.5 The graphics subprograms

ASYST has powerful built-in graphics facilities. Ordinary two-dimensional plots (e.g. plots of a function vs. an independent variable) can easily be made in many different fashions. For a closer look at these capabilities, see [39, ch. 6]. These Words are so easy to use that they can normally be used directly from the command line interpreter.

In addition to this ASYST also features Words to make three-dimensional plots, such as contour plots and *netsurface* or *azometric* plots [40, ch. 9]. Examples are shown in Fig. 59. These 3-D plotting Words are the ones that form the backbone of the graphics utilities in AIDA. For while the few Words which cover 3-D plotting in ASYST are easy to use, they are not very flexible and so additional programming is called for. In the process it was discovered that the plots are not always of sufficiently good quality, as can be seen in the contour plot in Fig. 59, and therefore some additional programs were made to enable the data to be plotted using the



09 27 '89  
Data from 05130488 2  
First contour : 1700  
Last contour : 9000  
Contour spacing : 1000



09 27 '89  
Data from 05300894 9

*Figure 59. Examples of contour and azimuthal plots made with AIDA.*

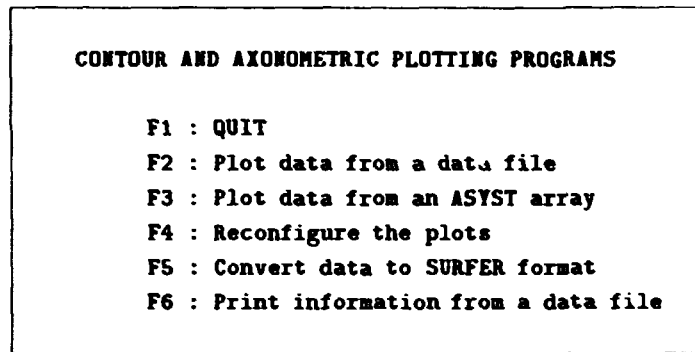


Figure 60. The graphics menu.

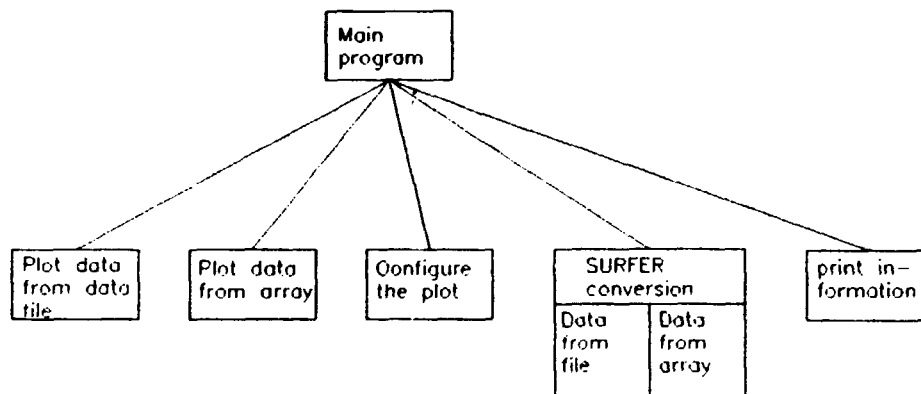


Figure 61. Structure of the graphics part of AIDA. The structure reflects the graphics menu options.

#### SURFER graphics software.

If you choose the graphics option in the main menu you will be presented with a new menu as shown in Fig. 60.

Physically the programs are divided into two overlay files, one containing the words to convert data into a SURFER file and the other containing all the rest. The two parts have similar structure and many words exist in both. For this reason I will in this section only describe the actual graphics in any detail. The structure of the two is shown in Fig. 61.

#### The actual plotting routines

Both the 3-D plotting and the SURFER conversion programs can be further divided into two parts. One takes the data to be plotted or converted from an ASYST data file created with AIDA. The other takes as input an ordinary two-dimensional ASYST array. Again, there is much overlap between the two parts. Generally speaking, the only difference between plotting data from a file or an



Data file plotting program			
Contour Plot		Axonometric Plot	
Manipulate data		Manipulate data	
Plot to screen	Plot to HP plotter	Plot to screen	Plot to HP plotter

Figure 62. Block structure of the Words for plotting data from a data file.

<p>F1 : Plot to screen  F2 : A4 plot to plotter  F3 : A3 plot to plotter</p>
--------------------------------------------------------------------------------------

Figure 63. The plotting menu.

array is how they find the data to be plotted. In both parts there are checks as to whether the file/array exists, whether the data set is two-dimensional etc.. Again, they are so similar that they will not here be described separately. See Fig. 62 for the structure of these parts of the program.

Before specifying the data file/array where the data are stored the user is asked whether to make a contour or an axonometric plot. The treatment of the data varies somewhat for the two types of plot, so the program must know this at an early stage.

Once the data have been input to the program (they are stored in a `TOKEN` array) the user has several possibilities for manipulating the data before plotting. It is possible to take out a part of the data array for closer inspection or to deplete the array by taking only every *n*'th row or column. This is convenient for making contour plots of large arrays since `ASYST` may not otherwise have enough memory to make the plot. The array may also be transposed or turned around so that it can be shown from any side in an axonometric plot.

When the final data set has been obtained the user must specify some information about the plot to be made. For the axonometric plot the user must specify the viewpoint for the plot. For a contour plot the program must know which contour levels to plot. Also the shape of the plot may be fitted to the actual data if the data came from an `AIDA` data file which contained the relevant information. This will be described in more detail in the `AIDA` manual [43].

Finally the destination of the plot must be specified. At the moment there are in our system two possibilities, indicated by the menu which is shown in Fig. 63.

#### Auxilliary functions

Two other options exist in the graphics menu which we have not yet discussed. They are both very simple.

Option 4 in the menu will give you a set of questions like the ones in the dialogue before a data acquisition session (see p. 82). Only here the questions will be about the size of the plots, the colours to use and the type of lines (solid, dashed etc.) for the contour plots. The questions and the default values are saved in a `Measurement`

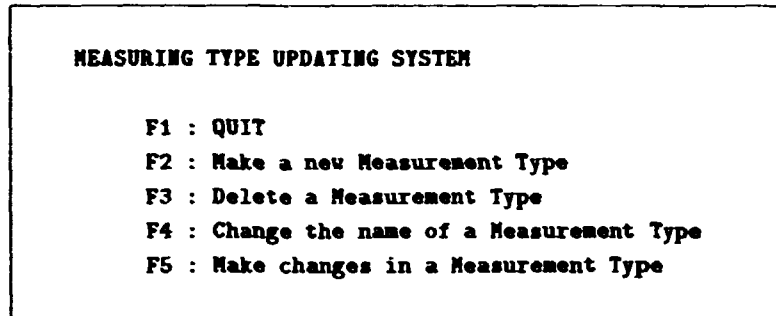


Figure 64. Measurement Type updating menu.

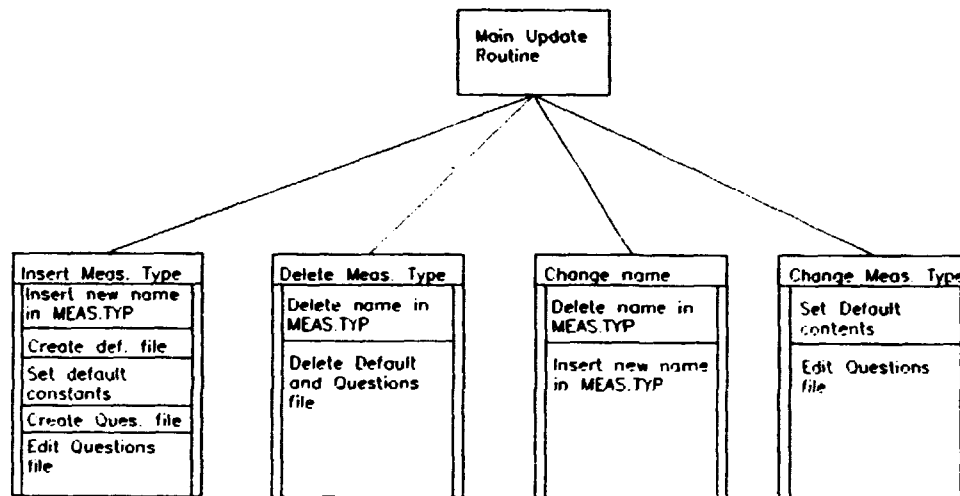


Figure 65. Block structure of the Words for making or updating a Measurement Type.

Type of its own. This Measurement type is not listed in the MEAS.TYP file and to avoid conflict they have a three-letter extension: QUESTION.CON and DEFAULT.CON.

Option 6 will print the information that is stored in the comments of a data file made with AIDA. This should need no further explanation.

## 5.6 Making and updating Measurement Types

In section 5.3 the concept of the Measurement Type was introduced. From the structure of the Measurement Types and the way they are referenced it can be seen that it would be a fairly straightforward process to create new Measurement Types or to modify existing ones. However, there is still considerable scope for error in the process, especially if it is not done often. For this reason a part of AIDA was developed to take care of the maintenance of Measurement Types.

This part of AIDA is stored in a separate overlay file and is invoked with option 4 in the main menu. You will then get a new menu, see Fig. 64.

The block structure of this part of the program is given in Fig. 65. As can be

seen, the various options in the updating menu use the same building blocks. Some of the options will therefore only be described very briefly in the following.

#### **Changes to the MEAS.TYP file**

As mentioned earlier, the file MEAS.TYP contains a list of the currently defined Measurement Types. The object of options 2-4 in the menu will therefore be to manipulate this file. Inserting a new name and abbreviation for a Measurement Type consists simply of getting the name from the user and writing it to an empty slot in the file. However, before entering the new name the program must search the list to see if the name or abbreviation already exists. The list of names may also be full. In any case, the user will be told and must choose another name.

The Words for deleting a Measurement Type are similar. Here too, the program must get the name from the user, and then delete the entry in the list if it exists. The user can also choose whether to keep the QUESTION.MM and DEFAULT.MM files or delete them.

Once these two parts have been made they can easily be combined to change the name of a Measurement Type. All that is needed is a small routine to change the extensions of the QUESTION and DEFAULT files.

#### **Changes to the Measurement Type files**

Since each Measurement Type consists of two files of different types it is obvious that this part of the program is subdivided into two sets of routines, each manipulating one part of the Measurement Type. Here, changes to the DEFAULT file will be considered first.

In option 2 in the menu the new DEFAULT file must first be created and then filled. The second part is identical to option 5 in the menu. The changes that can be made to a DEFAULT file with these Words only affect the last part of the array. The first 20 slots in the array are changed in the dialogue in the data acquisition session and the next 8 (in our set-up) are changed by option 4 in the data acquisition menu (see section 5.4). The values in the rest of the array slots can be set in this part of the program. This session is a questions menu like the one in every data acquisition session (p. 82). The questions are saved in the file QUESTION.SET. They can of course be changed to fit another experimental set-up.

## **5.7 Present and future developments**

In the form described above AIDA has been designed to perform data acquisition via an A/D plug-in board. However, ASYST also has facilities to communicate with instruments via the GPIB data communication bus. This enables ASYST to communicate with many different types of instruments, such as spectrum analysers, digital oscilloscopes etc.. For a programmer who wants to make a general-purpose program which utilises the GPIB bus this raises a number of difficulties. Most important among these is the fact that different instruments have different formats for the orders they need for communicating. Also, the format of the data varies between instruments. This in effect makes it impossible to satisfy all the objectives of AIDA: that the user should be able to run it without detailed knowledge of ASYST or the hardware involved in the data acquisition.

The solution to this is to require the user to make a routine which performs the actual data acquisition. This must be compiled before calling AIDA and will then be called by AIDA at runtime. AIDA can then control the independent variables

between each measurement. This arrangement also allows the user to perform some manipulation of the acquired data immediately after the acquisition. This is handy if the amount of data is too large to store, which can be a problem with for instance long time traces from transient recorders or digital oscilloscopes.

In practice the user may have to produce more than one routine as there may be orders which are only executed at the very beginning or end of the data acquisition session and not every time an acquisition is being made. The names of these programs must be placed on the first lines of the file QUESTION.XX (XX is again the abbreviation of the Measurement Type). They are then called at appropriate times using the ASYST Word "EXEC.

The questions session at the start of the data acquisition can be used to initialise variables for the user-defined routine. This is done with an ASCII file called ?.XX. This contains a list of the names of variables in the routine which are to be initialised. The number of names in the list should correspond to the number of questions and the variables will be given the value of the answer to the specific question. If not all the answers to the questions correspond to a variable in the routine, a name of a dummy variable can be used instead.

Since the data acquired by this method does not have any previously determined form, it is not possible in advance to create the data file for the results. This must therefore be done by the user's routines. Also the filling of the data file must be done by the user. For the same reason the data file thus created cannot be read by the graphics part of AIDA. In the future modifications may be made to the graphics part of AIDA in order to enable it to read non-standard files and extract the relevant data. This will probably work on the same lines as this new data acquisition.

This new data acquisition application has by now (medio June 1989) been implemented and has already been used in acquiring and analysing the data for the conditional statistical analysis in chapter 2 sec. 2.6. Here the data are acquired with a LeCroy digital oscilloscope used as a transient recorder. The amount of data measured in each session is upwards of 10Mbytes. Therefore the analysis is performed immediately at each point across the plasma column. However, this new feature is by no means completed yet. Most importantly, some small bugs still haunt the system. Also, new features may be added, but these will have to be thought up first.

## A Some useful relations between Chebyshev series

A given function  $f(x)$ , defined in the interval  $-1 \leq x \leq 1$  can be expanded as an infinite series of Chebyshev polynomials:

$$f(x) = \sum_{m=0}^{\infty} a_m T_m(x) \quad (89)$$

Given this expansion we can write various expansions of  $\hat{L}f$  where  $\hat{L}$  is some operator:

$$xf(x) = \frac{1}{2}a_1 + (a_1 + \frac{1}{2}a_2)T_1(x) + \frac{1}{2} \sum_{m=2}^{\infty} (a_{m-1} + a_{m+1})T_m(x) \quad (90)$$

$$\begin{aligned} x^2 f(x) &= \frac{1}{4}[(2a_1 + a_2) + (3a_1 + a_2)T_1(x) + (2a_1 + 2a_2 + a_3)T_2(x) \\ &+ \sum_{m=3}^{\infty} (a_{m-2} + 2a_m + a_{m+2})T_m(x)] \end{aligned} \quad (91)$$

$$f'(x) = \sum_{\substack{p=1, \\ p \text{ odd}}}^{\infty} p a_p + 2 \sum_{m=1}^{\infty} \sum_{\substack{p=m+1, \\ p+m \text{ odd}}}^{\infty} p a_p T_m(x) \quad (92)$$

$$x f'(x) = \sum_{\substack{p=2, \\ p \text{ even}}}^{\infty} p a_p + \sum_{m=1}^{\infty} (m a_m + 2 \sum_{\substack{p=m+2, \\ p+m \text{ even}}}^{\infty} p a_p) T_m(x) \quad (93)$$

$$f''(x) = \frac{1}{2} \sum_{\substack{p=2, \\ p \text{ even}}}^{\infty} p^2 a_p + \sum_{m=1}^{\infty} \sum_{\substack{p=m+2, \\ p+m \text{ even}}}^{\infty} p(p^2 - m^2) a_p T_m(x) \quad (94)$$

$$\begin{aligned} x f''(x) &= \frac{1}{2} \sum_{\substack{p=3, \\ p \text{ odd}}}^{\infty} p(p^2 - 1) a_p + \sum_{m=1}^{\infty} (2m(m+1) a_{m+1} \\ &+ \sum_{\substack{p=m+3, \\ p+m \text{ odd}}}^{\infty} p(p^2 - m^2 - 1) a_p) T_m(x) \end{aligned} \quad (95)$$

$$\begin{aligned} x^2 f''(x) &= \frac{1}{2} \sum_{\substack{p=2, \\ p \text{ even}}}^{\infty} p(p^2 - 2) a_p + \sum_{m=1}^{\infty} (m(m-1) a_m \\ &+ \sum_{\substack{p=m+2, \\ p+m \text{ even}}}^{\infty} p(p^2 - m^2 - 2) a_p) T_m(x) \end{aligned} \quad (96)$$

## B Consistency of the discrete Fourier expansion

The proof that Eq. 25 and Eq. 26 are consistent with each other can be seen by inserting one in the other[47]:

$$\begin{aligned} f(x_{j..}) &= \sum_{k=0}^{N-1} \left[ \frac{1}{N} \sum_{j=0}^{N-1} f(x_j) e^{-i \frac{2\pi}{N} j k} \right] e^{i \frac{2\pi}{N} k j} \\ &= \frac{1}{N} \sum_{j=0}^{N-1} f(x_j) \sum_{k=0}^{N-1} e^{i \frac{2\pi}{N} k (j.. - j)} = \frac{1}{N} \sum_{j=0}^{N-1} f(x_j) \sum_{k=0}^{N-1} \left( e^{i \frac{2\pi}{N} (j.. - j)} \right)^k. \end{aligned}$$

The last sum is a geometric series:

$$\sum_{n=0}^{N-1} a^n = \sum_{n=1}^N a^{n-1} = \frac{1 - a^N}{1 - a},$$

and so we get:

$$f(x_{j..}) = \frac{1}{N} \sum_{j=0}^{N-1} f(x_j) \frac{1 - e^{i 2\pi (j.. - j)}}{1 - e^{i \frac{2\pi}{N} (j.. - j)}}.$$

Since both  $j$  and  $j_0$  are integers we have for all  $j$ :

$$1 - e^{i 2\pi (j.. - j)} = 0$$

while the following is valid only for  $j = j_0$ :

$$1 - e^{i \frac{2\pi}{N} (j.. - j)} = 0.$$

This means that all the terms in the sum are zero except for the term where  $j_0 = j$ . For this term we use l'Hospital's rule to get:

$$\left. \frac{1 - e^{i 2\pi (j.. - j)}}{1 - e^{i \frac{2\pi}{N} (j.. - j)}} \right|_{j=j_0} = \left. \frac{\frac{d}{dj} (1 - e^{i 2\pi (j.. - j)})}{\frac{d}{dj} (1 - e^{i \frac{2\pi}{N} (j.. - j)})} \right|_{j=j_0} = \frac{2\pi i}{\frac{2\pi}{N} i} = N.$$

From this we find:

$$f(x_{j..}) = \frac{1}{N} \sum_{j=0}^{N-1} f(x_j) \cdot N \delta(j - j_0) = f(x_{j..}).$$

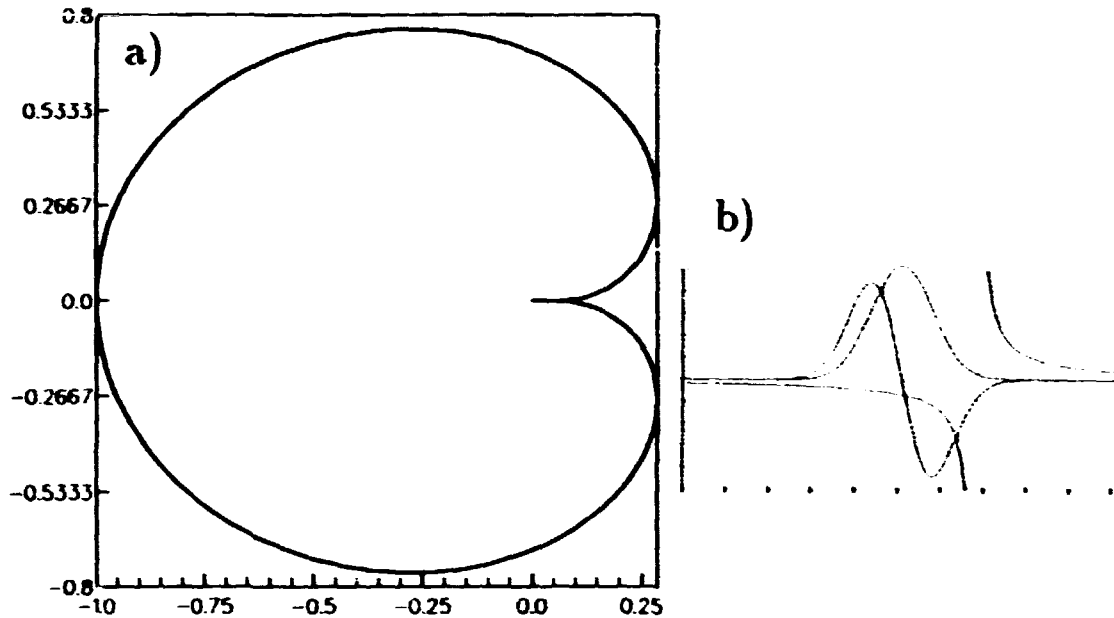


Figure 66. a) Values of  $R(u/k)$  for real values of  $u/k$ . The function  $f$  is here chosen to be a Maxwellian. b) A function  $f$  with only one maximum and its derivative, together with the function  $1/(v-u)$ .

## C Nyquist analysis for the plasma dispersion function

The following analysis has been performed by several authors, e.g. Jackson[46]. The problem is to determine the values of  $u/k$  for which the denominator of the right hand side of Eq. 67 vanishes, that is

$$1 - \frac{T_e}{M_i} \int_{1,2} \frac{f'_n(v)}{v - u/k} dv = 0. \quad (97)$$

where the integration paths run above and below the pole, respectively. We will first look at integration path 2. This is the classical plasma dispersion function.

Since  $T_e/M_i$  can take on many different values the question is whether the value of the integral in the equation can become real and positive. For this purpose we write the integral as

$$R(u) = \rho \int \frac{f'_n(v)}{v - u} dv + i\pi f'_n(u)$$

where  $u = u/k$ . The function  $R$  will map a curve in the  $u$ -plane into a curve in the  $R$ -plane. Specifically, the real  $u$ -axis will have the form given in Fig. 66a. This becomes clear when you look at Fig. 66b which shows the function  $f$ , its derivative, and the function  $1/(v-u)$ . For  $u \ll 0$  the real value is almost zero and the imaginary value is positive. For  $u \gg 0$  the imaginary value is negative. So as you trace out the real axis in the  $u$ -plane you will go around the curve in the  $R$ -plane in the direction indicated by the arrows. As we walk along the  $u$ -axis we will have  $u$ -values with positive imaginary values to the left of the axis. This must also be the case in the  $R$ -plane. Thus the positive imaginary  $u$ -plane maps into the inside of the curve in Fig. 66a. This means that  $R(u)$  can only attain positive real values for  $u$ -values with negative imaginary parts.

Now, values of  $u = u/k$  with negative imaginary parts correspond to negative  $k$ -values since  $\omega$  always has a positive imaginary part. Negative values of  $k$  only

occur in region 1 of fig 37. But  $n_2(k, \omega)$  is only defined in region 2. Therefore the denominator of  $n_2$  cannot become zero in the definition area and there are no poles due to the denominator.

For  $n_1(k, \omega)$  the situation is similar. In this case we integrate above the pole in the  $v$ -plane. So here we get

$$R(u) = \nu \int \frac{f'_u(v)}{v - u} dv - i\pi f'_u(u).$$

The result of this difference is that the curve in Fig. 66a is traced in the opposite direction. But then it will be  $u$ -values with negative imaginary parts that map into the inside of the curve. So only values of  $u$  with positive imaginary parts will satisfy Eq. 97. This corresponds to positive  $k$ -values which are only found in region 2. But  $n_1$  is only defined in region 1. So this too cannot have a pole due to the denominator in the region where it is defined.



## D Briefly on the Cubic Spline Interpolation

The following explanation is very brief. To get more information, see [19]. If we have a function  $y(x)$  given as a table of corresponding values of  $x$  and  $y$ , we can perform an interpolation between values of  $y$ . We choose for each interval between points a cubic polynomial to be the interpolating function. In the interval between  $(x_j, y_j)$  and  $(x_{j+1}, y_{j+1})$  this is written as:

$$y = Ay_j + By_{j+1} + Cy_j'' + Dy_{j+1}''$$

with

$$A \equiv \frac{x_{j+1} - x}{x_{j+1} - x_j},$$

$$B \equiv \frac{x - x_j}{x_{j+1} - x_j},$$

$$C \equiv \frac{1}{6}(A^3 - A)(x_{j+1} - x_j)^2,$$

$$D \equiv \frac{1}{6}(B^3 - B)(x_{j+1} - x_j)^2.$$

Here,  $y_j''$  is the second derivative of the polynomial at the point  $x_j$ .

The above definitions do not prescribe a unique cubic polynomial for the interval, since  $y_j''$  and  $y_{j+1}''$  can take any value. Therefore we prescribe a constraint, namely to require that the derivatives of the cubic polynomials should be continuous at the boundaries of the intervals. This constraint for the  $y_j''$ 's is equivalent to

$$\frac{x_j - x_{j-1}}{6} y_{j-1}'' + \frac{x_{j+1} - x_j}{3} y_j'' + \frac{x_{j+1} - x_j}{6} y_{j+1}'' = \frac{y_{j+1} - y_j}{x_{j+1} - x_j} - \frac{y_j - y_{j-1}}{x_j - x_{j-1}}.$$

For  $N$  points  $x_j$ , we get  $N - 2$  equations of this kind. Together with suitable constraints at the end points[19] we get a tridiagonal system of equations which can be solved to find the  $y_j''$ 's. Then the cubic interpolation polynomial is found for every interval.

When the interpolating polynomials have been found it is a straightforward matter to obtain the derivative of the original function. We find:

$$\frac{dy}{dx} = \frac{y_{j+1} - y_j}{x_{j+1} - x_j} - \frac{3A^2 - 1}{6}(x_{j+1} - x_j)y_j'' + \frac{3B^2 - 1}{6}(x_{j+1} - x_j)y_{j+1}''.$$

Similarly, the integral of the function can easily be found.

## References

- [1] *Plasma Physics and Nuclear Fusion Research*, Gill R. D. editor, Academic Press, London, (1981)
- [2] Roth J. R., Krawczonek W. H., Powers E. J., Hong J. Y. and Kim Y. C. *Phys. Rev. Lett.*, **40** 1450 (1978)
- [3] Ritz C. P., Brower D. L., Rhodes T. L., Bengtson R. D., Levinson, S. J., Luhmann N. C., Peebles W. A. and Powers E. J., *Nucl. Fusion* **27** 1125, (1987)
- [4] Iizuka S., Huld T., Pécseli H. L. and Rasmussen J. J. *Phys. Rev. Lett.* **60**, 1026 (1988)
- [5] Huld T., Iizuka S., Pécseli H. L., Rasmussen J. J. *Plasma Phys. Contr. Fusion* **30**, 1297 (1988)
- [6] Motley R. W. *Q-Machines*, Academic Press, New York, (1975)
- [7] Kent G. I., Jen N. C. and Chen F. F. *Physics of Fluids* **12**, 2140 (1969)
- [8] Weiland J. *Low Frequency Modes Associated with Drift Motions in Inhomogeneous Plasmas 3rd ed.*, Chalmers University of Technology, Gothenburg, Sweden 1985
- [9] P.K., Yu M. Y., Rahman H. U. and Spatschek K. H. *Phys. Rep.* **104**, 227 (1984)
- [10] Chen F. F. *Physics of Fluids* **8**, 912 (1965)
- [11] Pécseli H. L., Rasmussen J. J., Sugai H. and Thomsen K. *Plasma Phys. Contr. Fusion* **26**, 1034 (1984)
- [12] Spitzer L., *Physics of Fully Ionized Gases*, Interscience, New York, (1956)
- [13] Lamb H. *Hydrodynamics* Dover Press, (1932)
- [14] Grove Thomsen, P. *Numeriske metoder for sdvanlige differentiaalligninger*. Numerisk Institut, DTH, 1977
- [15] Ginzburg J. J. *Computational Physics* **20** 196-207 (1976)
- [16] Gottlieb D. and Orszag S. A. *Numerical Analysis of Spectral Methods: Theory and Applications*, SIAM, CBMS-NSF Reg. Conf. Ser. in Appl. Math. **26** 170pp. (1977)
- [17] Myers R. B., Taylor T. D., Murdock J. W. *J. Computational Physics* **43** 180-188 (1981)
- [18] Knorr G., Hansen F. R., Lynov J. P., Pécseli H. L. and Rasmussen J. J. *Physica Scripta* **38**, 892 (1988)
- [19] Press W. H., Flannery B. P., Teukolsky S. A., Vetterling W. T. *Numerical Recipes*, Cambridge University Press (1986)
- [20] Coutinas E. A., Hansen F. R., Huld T. and Lynov J-P. *Physica Scripta* **40**, 270, (1989)
- [21] Pécseli H. L., Rasmussen J. J. and Thomsen K., *Plasma Phys. Contr. Fusion*, **8**, 837 (1985)
- [22] Marcus P. S., *Nature*, **331**, 693 (1988)

- [23] Mason R. J., *Physics of Fluids* 13, 1042 (1970)
- [24] Andersen S. A., Christoffersen G. B., Jensen V. O., Michelsen P. and Nielsen P., *Physics of Fluids* 14, 990 (1971)
- [25] Fried B. and Conte S., *The Plasma Dispersion Function*, Academic Press, New York (1961)
- [26] van Kampen N. G. *Physica* 23, 641 (1957)
- [27] Jensen V. O., *Foerlesningsnoter i Plasmafysik II.*, Ris (1984)
- [28] Doveil F. and Grézillon D. *Phys. of Fluids* 18, 1756
- [29] Johnsen H. *Interaction between low energy ion beam and ion acoustic fluctuations in field free plasma*, University of Tromsø, Norway 1984
- [30] Taylor R. J., MacKenzie K. R. and Ihezi H. *Rev. Sci. Instrum.* 43 1675 (1972)
- [31] Limpacher R and MacKenzie K. R. *Rev. Sci. Instrum.* 44 726, (1973)
- [32] Andersen S. A., Christoffersen G. B., Jensen V. O., Michelsen P. and Nielsen P., *Physics of Fluids* 14, 728 (1971)
- [33] Hegerberg R., Elnford M. T. and Skullerud H. R., *J. Phys.* B15, 797 (1982)
- [34] Taylor R. J. and Coroniti F. V., *Phys. Rev. Lett.* 29, 34 (1972)
- [35] Kiwamoto Y. *J. Phys. Soc. of Japan* 37, 466 (1974)
- [36] Fujita T., Ohnuma T. and Adachi S., *Plasma Physics*, 10, 875 (1977)
- [37] Grézillon D., Doveil F. and Buzzi J. M., *Phys. Rev. Lett.* 34, 197 (1975)
- [38] Lynov, J. P. and Michelsen, P., *GANDALF, A Generally Applicable Numerical Data Acquisition Laboratory Facility*, Risø-M-2393 (1983)
- [39] *ASYST 2.0 Module 1, system, graphics, statistics tutorial*, Macmillan Software Company, 1987.
- [40] *ASYST 2.0 Module 2, Analysis*, Macmillan Software Company, 1987.
- [41] *ASYST 2.0 Module 3, Acquisition*, Macmillan Software Company, 1987.
- [42] *ASYST 2.0 Module 4, GPIB/IEEE-488*, Macmillan Software Company, 1987.
- [43] Huld, T., *Users guide for AIDA*, Plasma Physics Section, Risø-I-470 (in preparation)
- [44] Huld, T., *Reference Manual for AIDA*, Plasma Physics Section, Risø-I-471 (in preparation)
- [45] *Surfer Reference Manual*, Golden Software Inc., Golden CO, USA
- [46] Jackson J. D., *J. Nucl. Energy C1* 171 (1960)
- [47] J-P Lynov, private communication.

---

 Title and author(s)

**Experimental and Numerical Investigations of Plasma Turbulence**
**Thomas Huld**


---

 ISBN

**87-550-1624-3**

ISSN

**0418-6435**


---

 Dept. or group

**Department of Optics and Fluid Dynamics**

Date

**July 1990**


---

 Groups own reg. number(s)

Project/contract no.

---

 Pages

**105**

Tables

**0**

Illustrations

**66**

References

**47**


---

 Abstract (Max. 2000 char.)

Turbulence in plasmas has been investigated experimentally and numerically. The work described here is divided into four parts:

- Experiments on edge turbulence in a single-ended Q-machine. Convective cells are investigated in detail together with the anomalous transport caused by them.
- Numerical simulation of the edge turbulence in the Q-machine. This simulation uses spectral methods to solve Euler's equation in a cylindrical geometry.
- Measurements on wave propagation and the ion beam instability in an unmagnetized plasma with an ion beam with a finite diameter.
- Development of software for the automated acquisition of data. This program can control an experiment as well as make measurements. It also includes a graphics part.

---

 Descriptors INIS/EDB

**A CODES; COMPUTERIZED SIMULATION; CONTINUITY EQUATIONS; DATA ACQUISITION; HELMHOLTZ INSTABILITY; PLASMA; PLASMA MICROINSTABILITIES; PLASMA SIMULATION; TURBULENCE**

---

 Available on request from:

Eise Library, Riso National Laboratory (Riso Bibliotek, Forskningscenter Riso)

P.O. Box 49, DK 4000 Roskilde, Denmark

Phone +45 42 37 12 12, ext. 2268/2269 · Telex 43 116 · Telefax +45 46 75 56 27

**Available on exchange from:  
Risø Library,  
Risø National Laboratory, P.O. Box 49,  
DK-4000 Roskilde, Denmark  
Phone +45 42 37 12 12, ext. 2268/2269  
Telex 43 116, Telefax +45 46 75 56 27**

**ISBN 87-550-1624-3  
ISSN 0418-6435**